공학박사학위논문

고분자 전해질막 연료전지 시스템 고장 반응 및 심각도 기반 고장진단 방법

Fault response and severity-based fault diagnostic method for polymer electrolyte membrane fuel cell system

2021 년 8 월

서울대학교 대학원

기계항공공학부

박 진 영

고분자 전해질막 연료전지 시스템 고장 반응 및 심각도 기반 고장진단 방법

Fault response and severity-based fault diagnostic method for polymer electrolyte membrane fuel cell system

지도교수 김 민 수

이 논문을 공학박사 학위논문으로 제출함

2021 년 4 월

서울대학교 대학원

기계항공공학부

박 진 영

박진영의 공학박사 학위논문을 인준함

2021 년 6 월

위 원 장 : _____

부위원장 : _____

위 원 : _____

위 원 : _____

위 원 : _____

Abstract

Fault response and severity-based fault diagnostic method for polymer electrolyte membrane fuel cell system

Jin Young Park
Department of Mechanical Engineering
The Graduate School
Seoul National University

In recent years, interest in hydrogen society has grown from the viewpoint of a sustainable clean energy society. Hydrogen is the most abundant element in the universe and can be easily produced. When hydrogen becomes a commonly used fuel, an energy conversion device is needed. A polymer electrolyte membrane fuel cell (PEMFC) system is the most widely distributed device so far, with many advantages among many devices. However, there still are some barriers to overcome for the commercialization of the PEMFC system;

reliability and durability. In order to improve the reliability and durability of the fuel cell system, fault diagnosis technology is essentially required. Since the performance and durability of the PFMFC highly depend on operating conditions, faults in the system should be correctly detected in the early stage for its protection.

Firstly, fault responses of a PEMFC stack and PEMFC system are investigated in this study. A response of 1 kW PEMFC stack under insufficient reactant supply or failure thermal management is investigated. Next, probable fault scenarios in a 1 kW class PEMFC system are established. The fault scenarios in air providing system, fuel providing system and thermal management system are classified depending on their fault severity to the stack or the entire system. Responses of control and sensing signals are investigated and analyzed under each fault scenario.

Secondly, a fault diagnostic method for the PEMFC system is suggested in this study. Considering that response time and magnitude differ depending on fault severity, three neural networks that diagnose the critical fault, significant fault and minor fault, respectively, are developed. The neural networks together work as a ‘severity-based fault diagnosis algorithm.’ The algorithm can achieve both sensitivity and robustness by adjusting the moving average time and standard deviation multiplication value that divides the

residual data. The residual data is acquired from the control and sensing signals during the system operation. The severity-based fault diagnosis algorithm can be developed using a tabularized expected fault response without experimental data. As a result, the developed algorithm successfully diagnosed all the considered fault scenarios.

Thirdly, a local current distribution prediction method is suggested in this study. Local current distribution studies have been conducted experimentally or numerically. Both approaches had limitations. In order to overcome the limitations, a neural network-based local current distribution prediction model is developed. Current distribution data is collected under various pressure, temperature, reactant stoichiometric ratio and relative humidity conditions. The model is developed with the data and successfully predicted local current distribution. Using the model, the effect of the operating parameters is investigated.

Lastly, a local current distribution prediction model under degradation and fault is suggested in this study. The performance of the fuel cell inevitably decreases over time. With the degradation, local current distribution also changes. Therefore, understanding and predicting the current distribution changes are important. An accelerated stress test (AST) is applied to the fuel cell for fast degradation. With the AST, current distribution data is collected.

Also, fault data under elevated temperature, reduced humidity and varying cathode stoichiometric ratio condition are collected. With the collected data, local current distribution model based on a neural network is developed. As a result, the model predicted the current distribution under degradation and fault with high accuracy.

In summary, a fault response of PEMFC is investigated from the viewpoint of the system and local current distribution. A severity-based fault diagnosis algorithm is suggested and validated with the PEMFC system fault experimental data. Also, local current distribution prediction algorithm is suggested and successively predicted the current distribution under PEMFC degradation and faults.

Keyword: Polymer electrolyte membrane fuel cell system, Fault diagnosis, Fault severity, Local current distribution, Degradation, Neural network

***Identification Number*: 2016-20653**

Contents

List of Figures

List of Tables

Nomenclature

PEMFC	polymer electrolyte membrane fuel cell
BOP	balance of plant
FDD	fault detection and diagnosis
ANN	artificial neural network
NN	neural network
ReLU	rectified linear unit
i	current density (A/cm^2)
I	current (A)
SR	stoichiometric ratio
sr	normalized stoichiometric ratio
std	standard deviation
RH	relative humidity (%)
rh	normalized relative humidity
P	pressure (bar)
p	normalized pressure
P1	water pump outlet pressure
P2	stack inlet pressure (bar)
P3	stack outlet pressure (bar)
P4	radiator outlet pressure (bar)
P5	water pump inlet pressure (bar)
T	temperature (ºC)

t	normalized temperature
T1	water pump outlet temperature (ºC)
T2	stack inlet temperature (ºC)
T3	stack outlet temperature (ºC)
T4	radiator outlet temperature (ºC)
T5	stack inlet temperature (ºC)

Subcripts

an	anode
ca	cathode
load	applied load

Chapter 1. Introduction

1.1 Background of the study

World energy demand has been covered by the usage of fossil fuels since the 19th century, which caused global warming. This global warming is the most important issue we are facing now in the 21st century. Scientists have come up with a concept of hydrogen society as a solution to this problem. Hydrogen is the most abundant element in the universe and can be easily produced. When hydrogen is liquefied or compressed, hydrogen can be used as a high-density energy carrier. Most importantly, hydrogen as fuel leaves only pure water as a by-product. To explore the potential for the hydrogen society, the United States department of energy has suggested 'H2@Scale' concept as shown in Fig. 1.1 [1]. In this concept, hydrogen replaces fossil fuels and works both as the main energy storage and energy source for electricity. In the case when electricity is on-demand, hydrogen is consumed to produce electricity. In this process, an energy conversion device is necessarily required. Among many devices, polymer electrolyte membrane fuel cell (PEMFC) is the most widely distributed device so far.

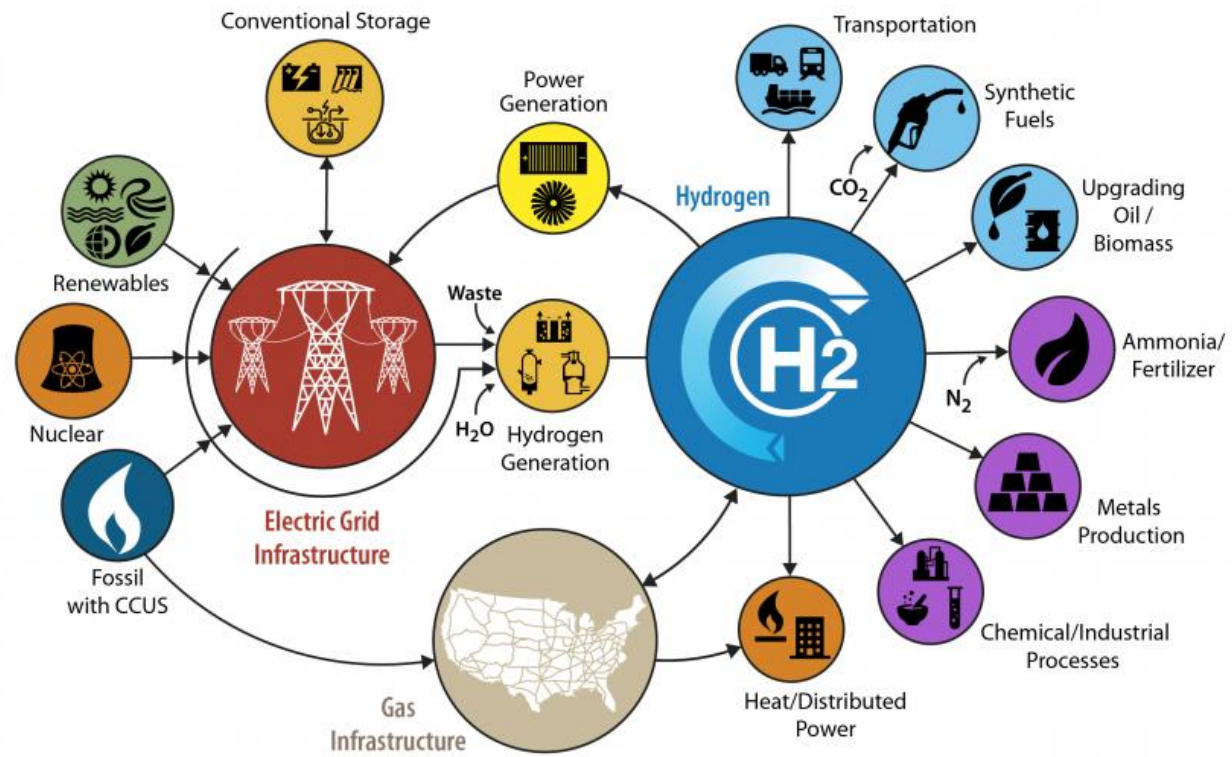

Figure 1.1 Schematic diagram of H2@Scale concept [1]

PEMFC is basically a device that converts the chemical energy of hydrogen into electricity. There are other types of fuel cells, but PEMFC is the most widely applied and commercially used fuel cell for many reasons; high efficiency, high power density, low operating temperature and fast response [2-4]. Compared to conventional internal combustion engines, however, PEMFCs still lack reliability and durability. According to the 2019 US national renewable energy laboratory (NREL) document [5], on-boarded PEMFC systems in fuel cell electric buses (FCEB) reported the average mean between road call (MBRC) less than 20,000 miles. As shown in Fig.1.2, the MBRCs of the fuel cell system are mostly higher than the 2016 department of energy (DOE) target since July 2016. However, the MBRC has not yet reached DOE's ultimate target. On the contrary, compressed natural gas (CNG) engines in CNG buses reported MBRCs more than 30,000 miles [6]. As the document says [5], PEMFC system road calls are caused by balance of plant (BOP) components, not the PEMFC stack.

A schematic diagram of a typical PEMFC system is shown in Fig. 1.3. The PEMFC system includes fuel cell stack and BOP subsystems; hydrogen supply system, air supply system, water management system, and thermal management system. These BOP subsystems are controlled to maintain the stable operating condition for the fuel cell stack. Unfortunately, however, faults occur in the

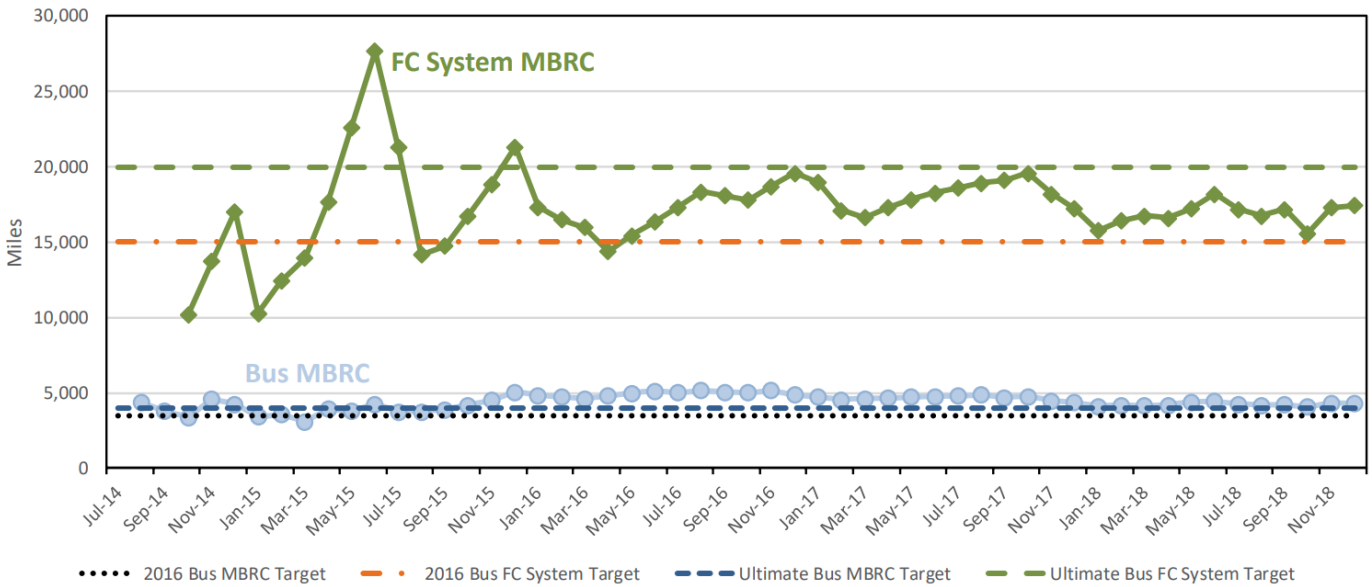

Figure 1.2 Miles between roadcall (MBRC) of fuel cell buses in-service in Unites States [2]

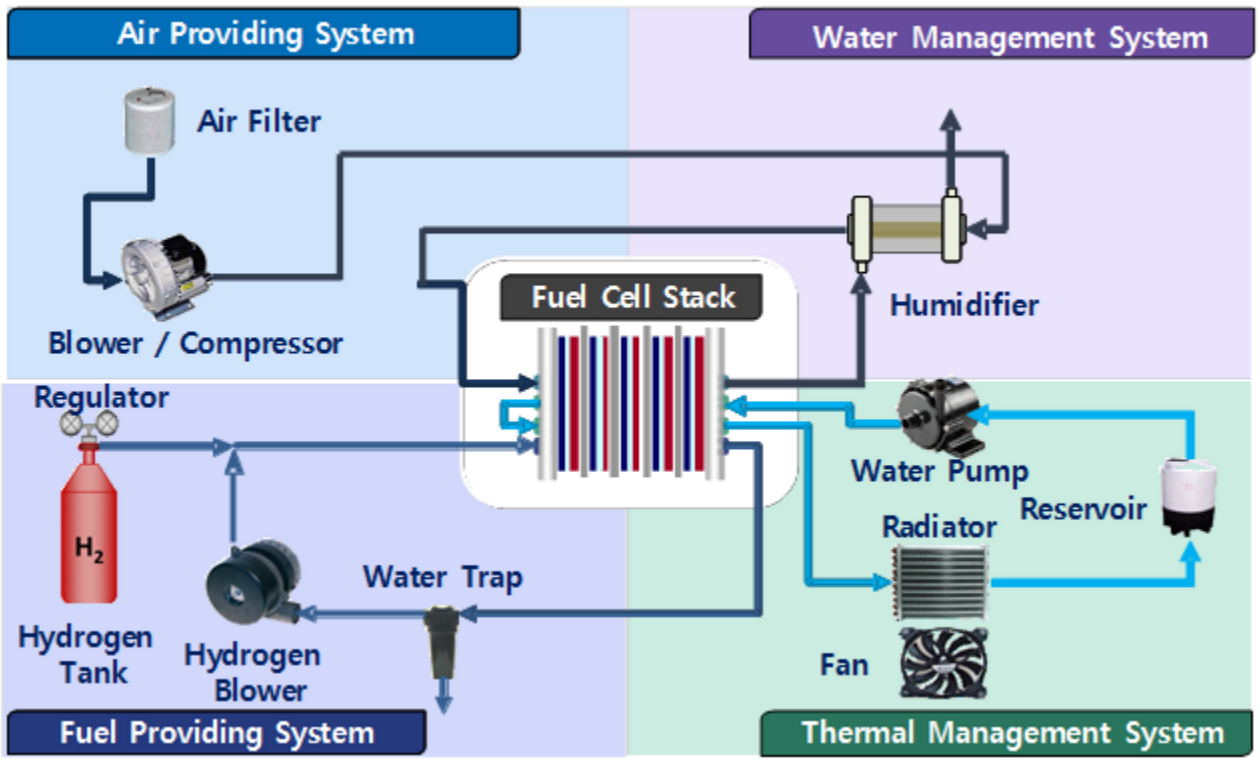

Figure 1.3 Schematic diagram of PEMFC system

subsystems from time to time. Since the PEMFC stack itself is a passive device, its performance and durability are highly affected by the operating condition, fault diagnosis technology for the PEMFC system is essentially needed [7,8]. With the fault diagnosis technology, faults can be properly detected fast and maintenance procedures can be executed to extend both the reliability and durability of the PEMFC system.

1.2 Literature survey

1.2.1 PEMFC fault diagnosis

According to Zheng and Petron [9,10], fault diagnosis methodologies can be divided into two groups; model-based methods and non-model-based methods. Firstly, model-based fault diagnosis methods simulate fuel cell system behavior with an analytical model. Depending on the simulation approach, models are classified into white-box models, grey-box models and black-box models [10]. The white-box model approach includes multi-dimensional mathematical and physical equations. While this seems to be an ideal approach, it is not easy to apply in a real-time system. Due to the sophisticated two-phase electrochemical reactions in PEMFC, it is not easy to develop a high-quality model. Moreover, high computational power and time are other barriers to the real-time system application. On the opposite, the black-box model approach relies on the use of empirical data. It is a simple, fast and practical approach. However, data dependency limits the genericity of the model. The grey-box model implements empirical data or expert knowledge in the form of simplified mathematical/physical equations or relations. By doing so, the grey-box model approach takes advantage of both genericity and simplicity. For its advantages,

many researchers choose to use this approach.

Non-model-based fault diagnosis methods are classified into signal-based, statistical-based and artificial intelligence (AI)-based methods based on their operating principles [9]. The signal-based method usually analyzes the target data on frequency and time domain. Applying mathematical techniques such as Fourier transform or wavelet transform [11], the system's state is diagnosed. The statistical-based method focuses on the correlation between the obtained data. Principal component analysis (PCA), kernel principal component analysis (KPCA) and fisher discriminant analysis (FDA) are widely used techniques [9]. The artificial intelligence (AI)-based method utilizes its pattern recognition performance. The AI model classifies the unseen normal or fault data without explicit design orders in the training process. Fuzzy logic (FL) [12,13], support vector machine (SVM) [14-16] and neural network (NN) [17] are typically favored AI techniques used in non model-based PEMFC fault diagnosis.

As well as PEMFC diagnosis methodology, PEMFC fault diagnostic target and level vary. According to Lee et al. [7], PEMFC system fault diagnosis target can be hierarchically divided into multiple stages (or levels), as shown in Fig. 1.4. In the first stage, PEMFC stack and balance of plant (BOP) subsystems are listed. Subsystems are fuel supply system (FPS), air supply system (APS), water management system (WMS), thermal management system (TMS).

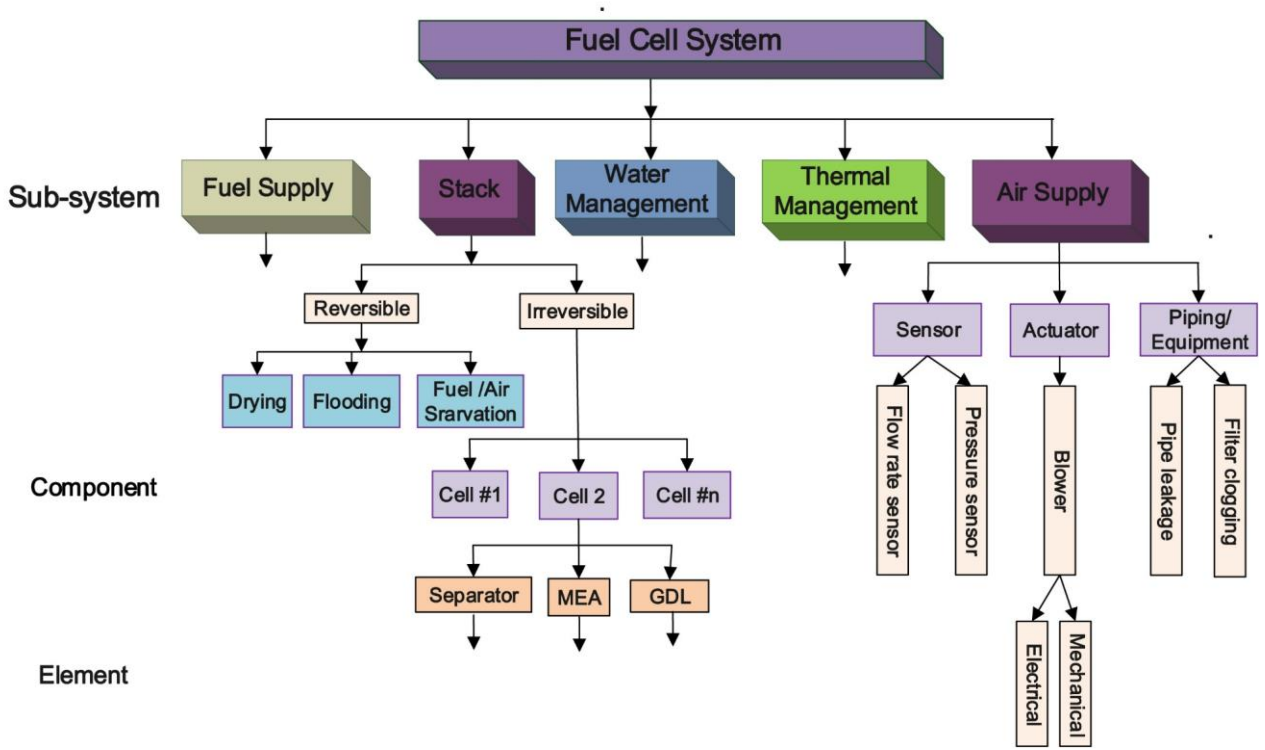

Figure 1.4 An example of multi-stage hierarchical fault detection and diagnosis (FDD) structure for a polymer electrolyte fuel cell (PEFC) system [7]

In the second stage, components that cause a fault in the subsystem are listed; sensors, actuators and piping/equipment. In the third stage, the cause of the fault is suggested at the elemental level.

Many of the previous studies so far have diagnosed the fault at the subsystem level [4]. Frequently addressed water management faults in the stack are flooding [18,19] and drying [20,21]. Shao et al. [22] diagnosed the faults of fuel supply system (FPS), air supply system (APS) and thermal management system (TMS). At the component level, Li et al. [16] diagnosed the low air supply fault and pressure-related faults. Pahon et al. [23] classified oversupplied air fault. Kamal et al. [24] detected the faults of air leakage, compressor, and three sensors with simulation results. Lee [7] and Oh [8] diagnosed more than ten component-level faults over the fuel cell system. At the element level, Lira et al. [25] detected air compressor friction increase with leakage of fuel and air. Escobet et al. [13] diagnosed increased compressor friction and compressor overheating faults with several component level faults; manifold air leakage, increased fluid resistance and control signal below the operating range.

PEMFC system fault diagnosis technology has improved over the decades. To the best of the author's knowledge, however, only the works of Lee [7] and Oh [8] suggest a diagnostic method for the entire PEMFC system with more

than ten different fault scenarios. As with the commercialization of the PEMFC system, fault diagnostic algorithms should be able to deal with more possible fault scenarios. Moreover, the fault diagnostic algorithm should be able to detect the severity of the fault for fast system protection.

1.2.2 PEMFC local current distribution

Despite the PEMFC development history for decades [26], the non-uniform current distribution issue has not yet been solved [27]. Non-uniform current distribution over the fuel cell is a sign of poor reactant and catalyst utilization. It reduces the performance of fuel cell. Also, the non-uniformity may cause local gas starvation, local flooding or local hot spot that leads to catalyst corrosion [28] or bipolar plate corrosion [29]. These corrosions accelerate the degradation of the membrane electrode assembly (MEA) [30], resulting in decreased durability. Local electrochemical reaction in PEMFC is affected by local temperature, pressure, relative humidity, water concentration and reactant concentration [31]. If these parameters are uniform over the fuel cell, the current distribution should also be uniform. However, these parameters vary. For instance, local temperature increases along with the coolant channel flow direction and local reactant concentration decreases along with the gas

flow channel. These inevitable local parameter variations cause uneven current distribution over the fuel cell. To minimize the non-uniformity, an understanding of PEMFC current distribution and its prediction are required.

For the understanding of local current distribution characteristics inside PEMFC, many experimental research has proceeded. In the 2000s, studies with the application of segmented fuel cell are reported focusing on the operating parameter effects. Liu et al. [32] investigated the relationship between water balance and fuel cell performance with segmented fuel cell data under low pressure, low temperature and low humidity conditions. Yoon et al. [33]studied the effects of reactant stoichiometry ratio (SR) and water management issues (flooding and drying). They concluded that the drying spreads from reactant inlet to outlet, whereas flooding proceeds from reactant the outlet region to the inlet region. Ghosh et al. [34] introduced a 240 cm^2 large area segmented fuel cell to scrutinize the effects of cathode SR and cathode inlet pressure on the PEMFC performance. While the cathode SR critically affected local current distribution, its effect on the performance was relatively low. With the pressure elevation, the current distribution was more uniformed. Sun et al. [35] investigated the influences of temperature, pressure, relative humidity (RH) and reactants' SR with a specially designed measurement gasket. Their experimental result shows that cathode SR and RH affect the current

distribution compared to anode SR and RH. Weng et al. [36] compared two types of membranes (Nafion 112 and Nafion 117) under low reactants' humidified conditions. As a result, Nafion 112 showed a more uniform current distribution compared to Nafion 117. Also, they concluded that the use of counter-flow channel design has an advantage over co-flow channel design in the aspect of current distribution.

In the 2010s, more detailed experimental studies were reported focusing on the effect of operating parameters. Jeon et al. [37] focused on the cathode humidification effect. They checked that high cathode humidification alleviates the non-uniformity of current distribution and increases fuel cell performance. One step further, Lin et al. [38] attempted to stabilize the local current density by optimizing the cathode relative humidity (RH). They showed that the RH optimization reduces current oscillation and contributes to better PEMFC performance. Lilavivat et al. [39] and Feng et al. [40] also investigated the RH effects on both anode and cathode. Both studies emphasize the impact of reactant humidification on the membrane water content, which is closely related to fuel cell performance. More specifically, cathode RH had a greater impact on both local current distribution and performance than anode RH. Peng et al. [41] and Gerteisen et al. [42] experimentally studied the effects of RH and SR on two different flow

channels (counter-flow channel and co-flow channel). The reactant RH was important regardless of the channel type. Also, the current distribution was relatively sensitive to the air SR than hydrogen SR [41]. Behaviors of currents distribution under starvations of fuel (hydrogen) and oxidant (oxygen) are investigated in the work of Liang et al. [43] and Dou et al. [44], respectively. One step further, Shao et al. [45] measured local temperature and local RHs in PEMFC with locally inserted microsensors. Reshetenko et al. [46] studied the local current distribution of PEMFC with the serpentine flow field type. Kim et al. [47] studied the effect of clamping torques on the local current distribution with a large active area (360 cm^2) segmented fuel cell. They found out that the curved end-plate is more effective in uniform current distribution than the plain end-plate.

One step further, some researchers focused on the evolution of current distribution with degradation. Weng et al. [48] investigated the aging effect with current cycling using a segmented fuel cell. Spernjak et al. [49] applied 1.3 V overpotential to the fuel cell and observed the change with a segmented fuel cell. Lin et al. [50] applied 2.0 V voltage reversal to the segmented fuel cell. Babu et al. [51] and Dillet et al. [52] repeated startup and shutdown cycles to degrade the fuel cell. The current distribution change is observed with parallel channel type segmented fuel cell. Lin et al. [53] observed changing current

distribution by applying a dynamic driving cycle. Lao and Fly [54] applied a mixed accelerated stress test cycle. Lin et al. [55] investigated the effect of the startup and shutdown cycle with segmented fuel cell. Shan et al. [56] investigated the durability of the fuel cell by applying a dynamic driving cycle.

Numerical works were also proceeded to predict PEMFC local current distribution under various operating conditions. Chevalier et al. [57] developed a pseudo-2D analytic model for predicting current density distribution. Wang et al. [58] developed a temperature distribution prediction model along the fuel cell channel and compared it with the experimental result. Askaripour et al. [59] investigated the effect of pressure, temperature, SR and RH on current distribution with a numerical simulation model. Yin et al. [60] studied the effect of SR with a two-phase CFD model. They added a non-isothermal model for a detailed investigation of the SR effect on RH, temperature distribution and current distribution.

Overall, many experimental studies were carried out to understand the characteristics of current local distribution since the 2000s, using a segmented fuel cell. Numerical studies were also carried out to simulate the current local distribution. While tendencies of most numerical simulation models match the experimental results [57-61], there still are errors between the model predictions and experiment results. Reminding that PEMFC electrochemical

reaction includes sophisticated interactions between mass transfer, two-phase flow and heat transfer mechanisms, numerical prediction error seems inevitable. The error may be reduced with a delicate simulation model. However, its complexity will increase computational time. In the viewpoint of commercial PEMFC development, therefore, a numerical approach has limitations for predicting local current distribution. An experimental approach also has limitations since the number of test operating condition cases is limited. The application of an artificial neural network (ANN) can be a solution in this case. The ANN has proven its powerful modeling performance in many research fields including PEMFC. The ANN model also shows a good performance with limited model training data. Therefore, with the neural network approach, limitations of both experimental approach and numerical approach seem to be surmountable.

In this sense, numerous research papers have applied neural network predicting the performance of PEMFC. Lee et al. [62] developed an empirical neural network-based model to predict PEMFC performance. They used temperature, pressure, SRs and RHs as input variables and achieved affordable accuracy results. In some studies, the cathode outlet temperature is predicted as well as its performance [63,64]. Jemei et al. [65] implemented a neural network-based fuel cell performance prediction model into the system on-board. Seyhan

et al. [66] predicted the performance of wavy serpentine flow channel fuel cell with a neural network model. Qu et al. [67] developed both radial basis function (RBF) network model and neural network model for PEMFC performance prediction. Both models showed good prediction accuracy. A similar conclusion was stated in another research predicting a 1.2 kW commercial PEMFC system [68]. Han and Chung [69] compared the prediction result with a neural network-based model and support vector machine (SVM). SVM, as a classic machine learning technique, showed great performance. However, better result was obtained with the neural network model. There were attempts to apply another type of neural network techniques in the field of PEMFC. Vural et al. [70] developed an adaptive neuro-fuzzy interference system (ANFIS) model for performance prediction. Puranik et al. [71] developed a recurrent neural network model for performance prediction. Both attempts showed that various neural network techniques could work on the fuel cell model. Neural network can be applied for different targets such as impedance model development [72] and hydration state analysis [73]. As introduced, neural network has been actively applied in the field of PEMFC for various targets with various techniques. However, to the best of author's knowledge, no current distribution prediction research with application of neural network-based model has been reported, except for the author's published work. With the application of neural

network, accumulated local current distribution data over decades could be effectively used for understanding PEMFC and its local current distribution prediction.

1.3 Objectives and scopes

Reliability and durability are two big barriers to overcome for the successful commercialization of polymer electrolyte membrane fuel cell (PEMFC) systems. A fault is one of the main reasons that reduce the reliability and durability of the system. Therefore, fault diagnosis technology is essentially required to protect the system.

The first purpose of this paper is to suggest a new fault diagnostic method for PEMFC. When developing a fault diagnostic algorithm, the algorithm's robustness and sensitivity are in the trade-off position. The suggested method achieves both robustness and sensitivity by applying multiple diagnostic neural networks based on fault severity. Moreover, the method requires no experimental fault data for the model development, which could help saving development time for the commercial PEMFC system. The second purpose of this paper is to suggest a modeling method for local current distribution. For many years, experimental and numerical studies were conducted. However, both approaches had limitations.

The suggested method in the paper overcomes this limitation by introducing a neural network model with limited experimental data. This way, acquired experimental data in the process of commercial PEMFC development can be effectively utilized with little effort. The method also considers the

change of local current distribution under faults and PEMFC degradation. The detailed explanations for this research outline are suggested below.

In chapter 2, the fault response of the 1 kW PEMFC stack and 1 kW PEMFC system are experimentally investigated. When a fault occurs, related signals change. The faults are diagnosed based on these signal changes. Therefore in this chapter, understandings of the fault response proceed before the diagnostic algorithm development. In the first part of this chapter, fault responses to the fuel supply failure, air supply failure, and thermal management failure are investigated. In the second part, the PEMFC system designed for fault experiments is introduced. Then, responses of 17 different BOP faults are experimentally investigated.

In chapter 3, a severity-based fault diagnostic method for a PEMFC system is suggested. The core idea of the algorithm is to separately diagnose the faults depending on their severity. Three neural network classifiers diagnose the critical faults, significant faults and minor faults, respectively. By separating the fault diagnosis classifiers, fault diagnosis accuracy and robustness are achievable at the same time. The development process of the severity-based fault diagnosis algorithm is suggested in detail as well as its diagnosis results.

In chapter 4, local current distribution prediction model is suggested. Local current distribution data is collected using segmented fuel cell under

various operating conditions. Using the data, a neural network based current distribution prediction model is developed. On step further, by switching the inputs and outputs of the training data, a new model is developed. The model suggests operating conditions for the uniform current distribution. The given operating condition is verified with the current distribution prediction model. In this chapter, pre-treatment and after-treatment of the data are described step by step.

In chapter 5, local current distribution prediction under fuel cell degradation and fault mode has proceeded. First, local current distribution evolution data under the degradation is collected with the accelerated stress test. Second, a fault experiment is performed between the accelerated stress test cycle to collect current distribution changes under faulty conditions. Modifying the method suggested in chapter 4, local current distribution model for degradation and fault is developed and validated.

Chapter 2. Fault response of PEMFC system

2.1 Introduction

Since a PEMFC system includes components with mechanical moving parts, faults occur from time to time. When a fault occurs, the performance of the system decreases. With a severe fault, the performance, as well as durability of the system, decreases. So in order the detect faults, a diagnosis algorithm should be developed. Before the development, however, fault characteristics should be understood in advance.

Understanding the fault response and its effects on the stack should be firstly considered. A fault experiment is performed with a 1 kW PEMFC stack in this chapter. Reactant starvation and failure of thermal control are simulated and physics between the faults and responses are briefly explained. Then, fault response to the system and its effects on the system are investigated with a 2.4 kW stack included 1 kW PEMFC system. The fault responses are measured with the sensors implemented in the system. The physics between the fault scenarios and corresponding responses are discussed.

2.2 Fault response of 1 kW stack

2.2.1 Experimental setup description

A single PEMFC consists of several components such as membrane electrolyte membrane assembly (MEA), a couple of gas diffusion layers (GDL), pair of gaskets and bipolar plates that include flow fields for fuel, oxidant and coolant. In this sub-chapter 10-cell-stacked 1 kW PEMFC (Powercell, S1-1000) is used for fault experiment. Experimental setup for the stack and its schematics are shown in Fig. 2.1(a) and Fig. 2.1(b), respectively. In the center of the system, the co-flow type stack is placed. Pure hydrogen gas with 99.999% purity is supplied to the stack anode channel by a mass flow controller (MFC). Air is supplied to the stack cathode channel with MFC. Both reactant gases are humidified through the bubbler-type humidifiers. A closed-loop thermal management system (TMS) is prepared for thermal control. The TMS consists of a reservoir, water pump (Iwaki, RD-30), Coriolis type mass flow meter (Oval, ULTRA mass MKII), and radiator (Heat exchanger: Wonsim, B-type, Fan: Sanyo Denki, San Ace 172). Pressure transmitters (PA-21SR, Keller) and thermocouples (T-type, Omega) are implemented between each TMS component and stack and labeled as P1, P2, P3, P4, P5, T1, T2, T3, T4, T5.

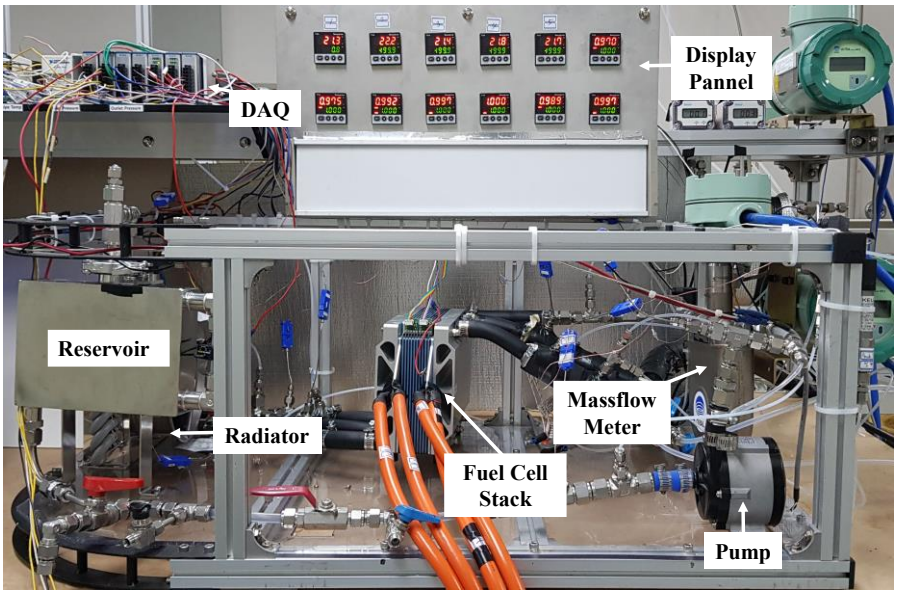

(a)

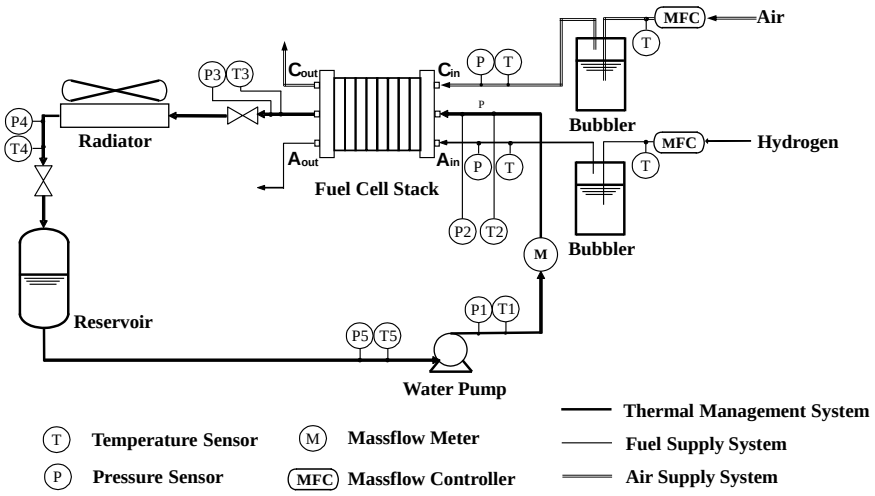

(b)

Figure 2.1 PEMFC stack experimental setup

(a) System picture (b) schematic diagram [17]

De-ionized water is used as a coolant for TMS. The current and voltage were measured with an electric loader (PLZ-1205WZ&, Kikusui). Information of mentioned components and sensors are organized in Table 2.1.

Table 2.2. shows the operating conditions for the normal state PEMFC stack. The stack is operated under a non-pressurized condition with an entering reactants' temperature of 60^{o}C. Both anode and cathode are fully humidified through the bubbler-type humidifiers. Stoichiometric ratios (SR) for anode and cathode are 1.5 and 2.0, respectively. The normal state stack coolant flow rate is 3.3 liters per minute, which corresponds to the maximum performance of the water pump. The stack outlet temperature is maintained at 65^{o}C with the PID-controlled radiator fan. Response of temperature control can slow when the control target is stack outlet temperature. Since the reactants' flow direction is the same as the coolant, however, maintaining the outlet region temperature contributes to preventing excessive flooding when a fault experiment in the TMS is performed.

Under these conditions, a maximum designed current load of 200A is applied to the stack. All the experimental conditions are controlled with the LabVIEW program, as shown in Fig. 2.3. Fig. 2.3(a) shows a panel for the thermal management control. Fig. 2.3(b) shows a panel for the load and reactants supply.

Table 2.1 Components and sensors for stack experimental setup

Component / Sensor	Model	Manufacturer	Specification / Measurement accuracy
Thermocouple	T-type	Omega	±0.5℃
Pressure transmitter	PA-21SR	Keller	±0.5% of full scale
Mass flow controller (Air)	F-202AV	Bronkhorst	±0.5% of reading ±0.1% of full scale
Mass flow controller (H_2)	F-201AC	Bronkhorst	±0.5% of reading ±0.1% of full scale
Mass flow meter (Water)	ULTRAmass MKII	Oval	±0.2% of reading
Humidity transmitter	HMT-330	Vaisala	±0.015% of reading ±1.0% of full scale
Water Pump	RD-30	Iwaki	BLDC motor
Radiator Heat exchanger	B-type	Wonsim	Fin-tube type
Radiator Fan	San Ace 172 9EH1724P5C01	Sanyo Denki	PWM controlled
Stack	S1-1000	Power Cell	200 cm^2 active area 10 cells stacked
Data acquisition board	cDAQ-9172	National Instruments	
Electric loader	PLZ-1205WZ	Kikusui	

Table 2.2 Stack operating conditions

Parameter	**Values**
Operating pressure (bar)	1
Cathode(Air) stoichiometric ratio	2.0
Anode(H_2) stoichiometric ratio	1.5
Cathode inlet temperature (℃)	60
Anode inlet temperature (℃)	60
Cathode Bubbler temperature (℃)	60
Anode Bubbler temperature (℃)	60
Normal state coolant flow rate (L min^{-1})	3.3
Stack coolant outlet temperature (℃)	65
Current (A)	200
Stack cell number	10
Normal state stack power (W)	1050

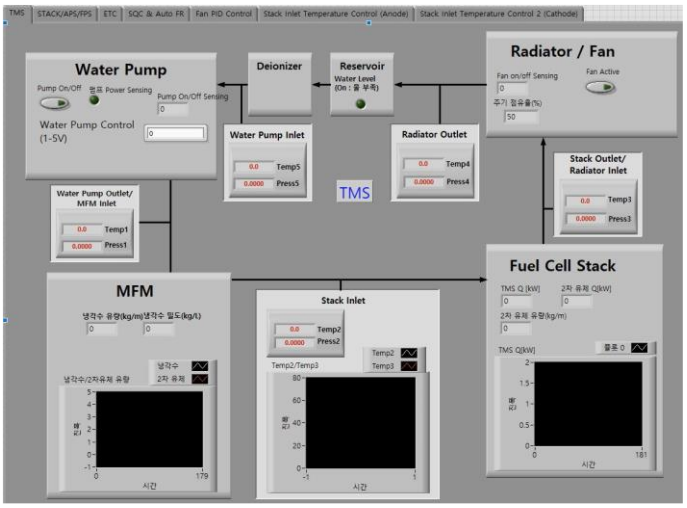

(a) Thermal management

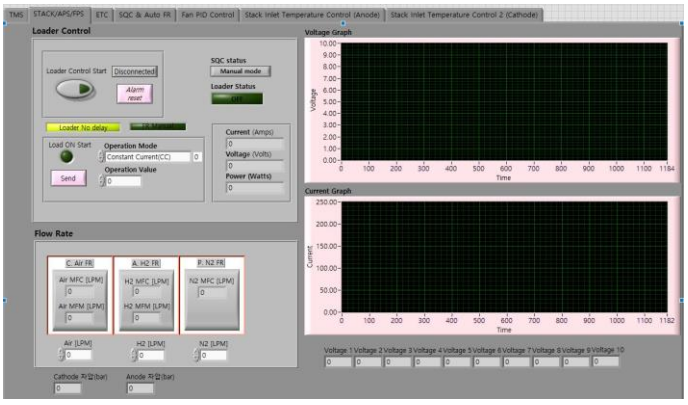

(b) Load and reactants

Figure 2.2 PEMFC stack experimental setup control panel

(a) Thermal management control (b) Load and reactants

2.2.2 Fault response of stack

A PEMFC stack performance is only secured when sufficient hydrogen and air are supplied with proper thermal management. In Fig. 2.4, responses of three fault scenarios are suggested; insufficient hydrogen supply at the anode, insufficient air supply at the cathode, insufficient coolant supply. Fig. 2.4(a) represents the case when hydrogen SR is reduced 20% from 1.5 to 1.2. In the normal state, the fuel cell stack maintains its voltage around 4.95 V. However, when hydrogen flow decreases, the stack voltage declines for a couple of minutes and fluctuates. As well as voltage decline, pressure difference over the anode channel also reduces with the decreased flow rate. A similar trend is shown with the fault case of reduced air SR 20% from 2.0 to 1.6 (Fig. 2.4(b)). Stack voltage decreased as well as pressure difference over the cathode with reduced air supply. Comparing the result of Fig. 2.4(a) and Fig. 2.4(b), the cathode fault response is bigger and faster than the anode. In other words, the cathode SR effect is more dominant and instantaneous than the anode SR effect. This trend is reported in many previous studies [61]. In Fig. 2.4(c) [14], stack inlet temperature (T2) and outlet temperature (T3) are shown instead of stack voltage. Also, PWM (pulse with modulation) signal is shown instead of pressure difference. This is because PEMFC operating temperature is not always optimized for its performance. Durability and water management issue

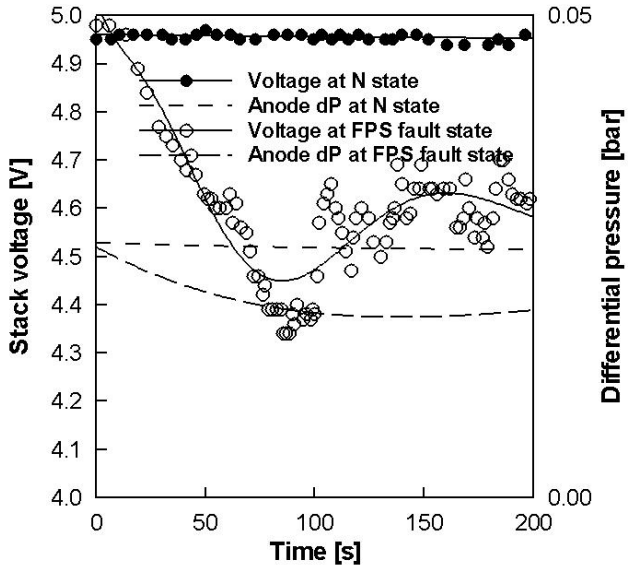

(a) Reduced fuel supply

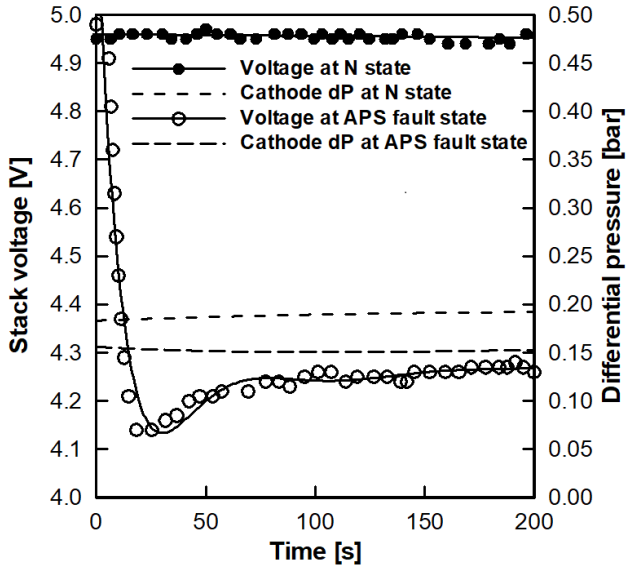

(b) Reduced air supply

Figure 2.3 Fault response of PEMFC stack (a) Reduced Fuel supply

(b) Reduced air supply (c) Reduced coolant supply [14]

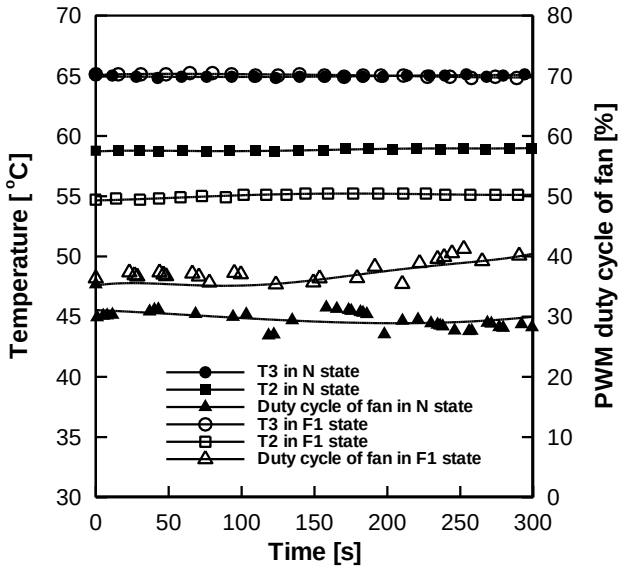

(c) Reduced coolant supply

Figure 2.3 Fault response of PEMFC stack (a) Reduced Fuel supply (b) Reduced air supply (c) Reduced coolant supply [17] (Continued)

in the reactant channel is also affected by operating temperature. In the normal state, the temperature difference between stack inlet and outlet temperature is around 6^{o}C. Under the reduced coolant state, the temperature difference spreads to around 10^{o}C. At both states, the radiator fan is PID controlled to maintain stack outlet temperature (T3) at 65^{o}C. Therefore, the PWM duty cycle signal of the fan also changes with the reduced coolant. With lesser coolant flow in the radiator heat exchanger part, air flow should be increased. This way, a similar amount of heat generated from the stack under the fault can be removed.

The fault case of heat removal failure is shown in Fig. 2.4(a) [14]. The case is simulated by disconnecting the fan power supply. Under the fault, the stack inlet and outlet temperatures (T2&T3) increase within a minute. The PWM duty cycle signal sent from the controller also increases but fails to remove heat due to the disconnected power line. When the power line of the water pump is disconnected, the coolant flow stops. Surprisingly, when the coolant flow stops, stack inlet and outlet temperatures slowly decrease, as shown in Fig. 2.4(b) [14]. The locations of thermocouples cause this distorted phenomenon. Stack's core temperature rises with the fault. However, the temperature of the coolant contacting the thermocouple decreases due to the dissipation to the ambient. In this case, therefore, the pressure transmitter placed in the stack inlet (P1) reacts to the fault and drops immediately.

As checked in Fig. 2.3 and Fig. 2.4., when a fault occurs, there are changes. The sensors implemented around the stack show these changes. It gives us incites that fault can be detectable by carefully observing the characteristics of these fault changes.

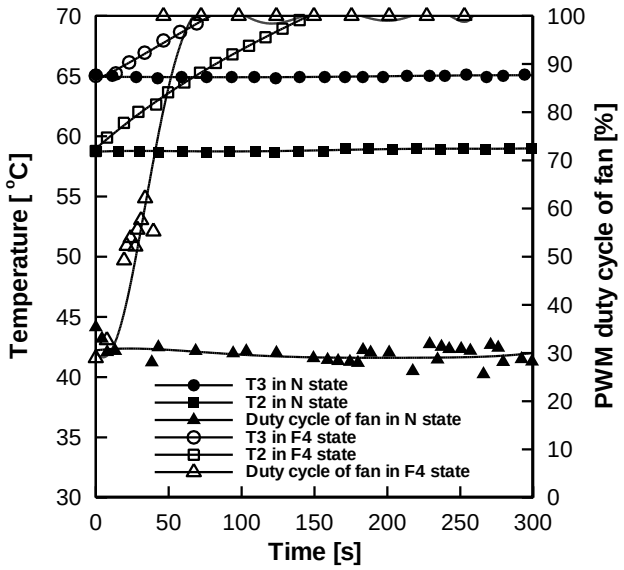

(a) Fan failure

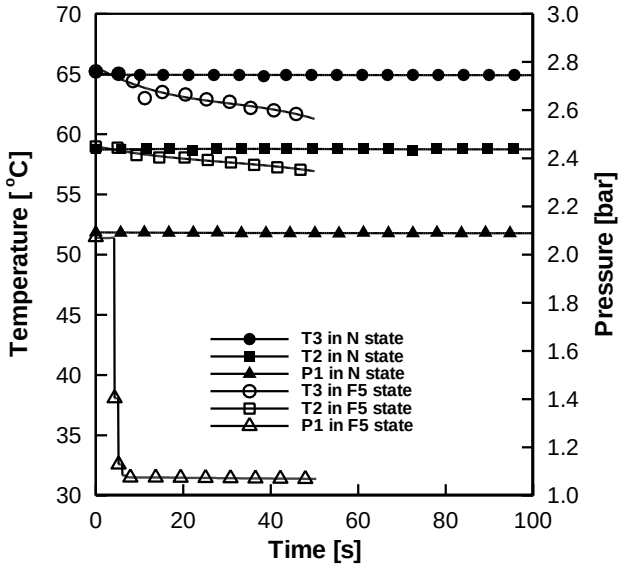

(b) Water Pump failure

Figure 2.4 Fault response of PEMFC stack thermal management

(a) Fan failure (b) Water pump failure [14]

2.3 Fault response of 1 kW PEMFC system

2.3.1 Description of 1kW PEMFC system

The PEMFC system configuration picture is shown in Fig. 2.5. On the top of the metal frame, a PEMFC stack (S2, Powercell) is located. The power load is applied to the stack with an electric loader (PLZ1205WZ & PLZ2405WZ, Kikusui). The balance of plant (BOP) system is placed below the stack. The BOP system includes fuel providing system (FPS), air providing system (APS) and thermal management system (TMS). A schematic diagram for the system is suggested in Fig. 2.6. Details of each BOP subsystem are described below.

The FPS is designed to recirculate the fuel for high fuel efficiency. Five-nine quality hydrogen is supplied from the hydrogen tank line. This hydrogen is then pumped to the stack with the hydrogen blower (recirculation pump, 118Z20, Thomas). Unused fuel comes out from the stack with water included. The liquid phase water is separated by the water trap. Then, fresh hydrogen gas merges with the rest of the unused fuel again to enter the hydrogen blower. While this circulation, purge is made through a purge valve to exhaust accumulated nitrogen gas from the cathode.

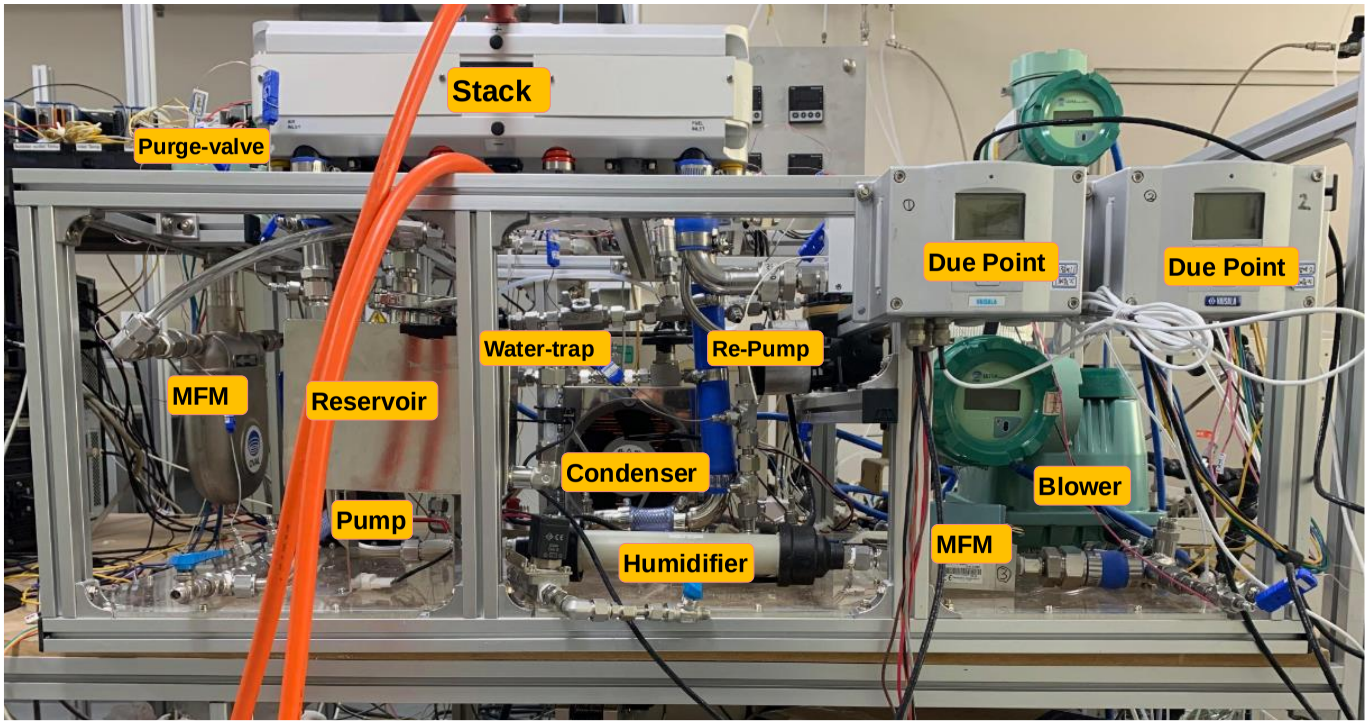

Figure 2.5 PEMFC system configuration

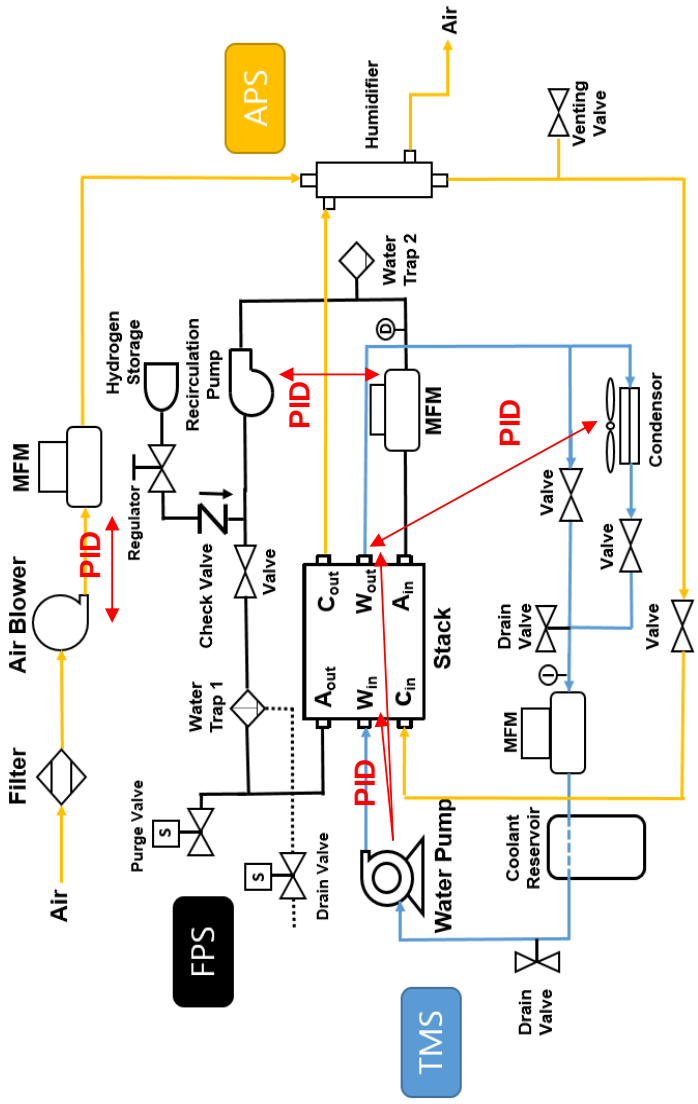

Figure 2.6 PEMFC system schematic diagram

The APS uses an air blower (HP200, Hiblow) to pump air into the stack. While the process, the airflow rate is check with a mass flow meter (MFM) (CMS0200, Yamatake). The air is then humidified through the membrane-type humidifier (FC125-240, PermaPure) and enters the stack. After the reaction insider the fuel cell, high water concentrated exhaust air goes into the humidifier for the elevation of the stack inlet air' temperature and humidity.

The TMS consists of three main components; water pump (RD-30, Iwaki), Radiator (Heat exchanger: B-type, Wonsim / Fan: Model, SanAce), mass flow meter (Ultramass, Oval) and reservoir. De-ionized water is filled into the system as a coolant. The coolant is supplied to the stack with a water pump from the reservoir. The stack outlet coolant is then cooled with a radiator. Here, a bypass line exists for the fast-startup process. After the cooling, the coolant flow rate is measured and circulated back to the reservoir. The specification of the components and sensors used in the system are listed in Table 2.3.

The system is controlled with the LabVIEW program. Each BOP subsystem control panel and fault control panel are shown in Fig.2.7. Figure 2.7(a), Fig. 2.7(b) and Fig. 2.7(c) represents FPS, APS and TMS respectively. Besides the mentioned components and sensors above, the location of implemented pressure and temperature sensors are shown. Fault conditions are simulated with the panel shown in Fig. 2.7(d).

Table 2.3 Components and sensors for system experimental setup

Component / Sensor	Model	Manufacturer	Specification / Measurement accuracy
Air blower	HP-200	HIBLOW	200 LPM at 20 kPa
Hydrogen blower	118ZC20	Thomas	22 LPM at 50 kPa
Air mass flow meter	CMS0200	Yamatake	±3% of reading ±1% of full scale
Hydrogen mass flow meter	TSM-D220	MKP	±2% of full scale
Mass flow meter (Water)	ULTRAmass MKII	Oval	±0.2% of reading
Humidifier	FC125-240	Perma pure	Membrane type
Water Pump	RD-30	Iwaki	Centrifugal BLDC motor
Radiator Heat exchanger	B-type	Wonsim	Fin-tube type
Radiator Fan	San Ace 172 9EH1724P5C01	Sanyo Denki	PWM controlled
Stack	S2-2400	Power Cell	200 cm^2 active area 24 cells stacked
Electric loader	PLZ-1205WZ PLZ-2405WZ	Kikusui	Max load 3.6 kW

The operating conditions of the PEMFC system are shown in Table 2.4. The cathode is operated under the non-pressurized condition with an SR of 2.0. The airflow rate is measured with the mass flow meter (MFM) in Fig. 2.7(b) and PID controlled with the air blower. In Fig. 2.7(a), FPS is provided with 0.1 bar (gauge) pressurized hydrogen gas from the regulator. This condition is set to reduce nitrogen gas crossover from the cathode. However, nitrogen gas is accumulated to the anode and stack voltage decreases with the operation. Therefore, the purge valve is opened to release anode gas every ten minutes and fills high-quality hydrogen gas. Like the APS, the hydrogen blower (recirculation pump) is PID controlled to provide fuel SR at 1.5, and its flow rate is checked with MFM. In TMS (Fig. 2.7(c)), the water pump is controlled to maintain a temperature difference of 5°C between the stack inlet and outlet. For example, when the temperature gap is less than 5°C, LabVIEW sends a higher control signal to the pump to increase the gap. When the temperature gap is more than 5°C, a lower control signal is sent to the pump. The radiator fan speed is controlled to keep the stack inlet temperature at 60°C. The LabVIEW sends pulse with modulation (PWM) signal from 0~100% to the fan. When the stack inlet temperature is higher than 60°C, a higher PWM signal is sent to the fan.

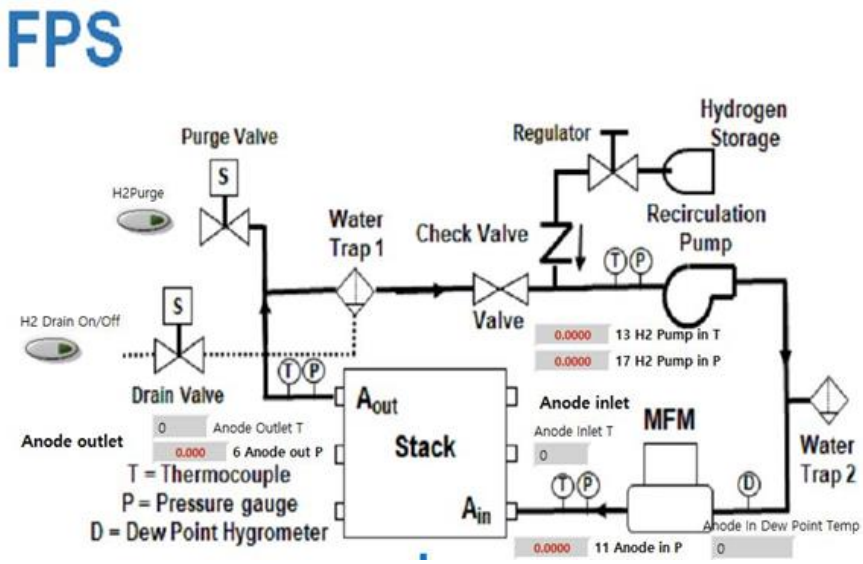

(a) Fuel providing system

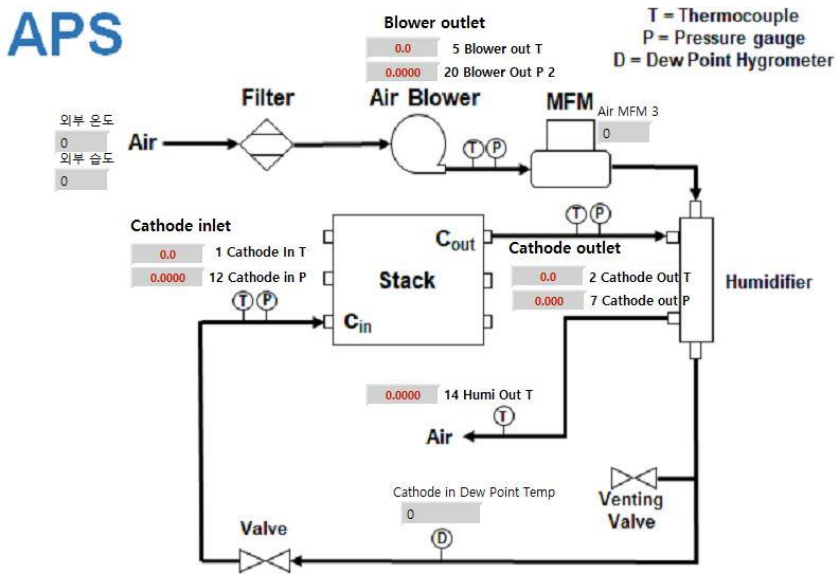

(b) Air providing system

Figure 2.7 PEMFC system control panel (a) Fuel providing system (b) Air providing system (c) Thermal management system (d) Fault control

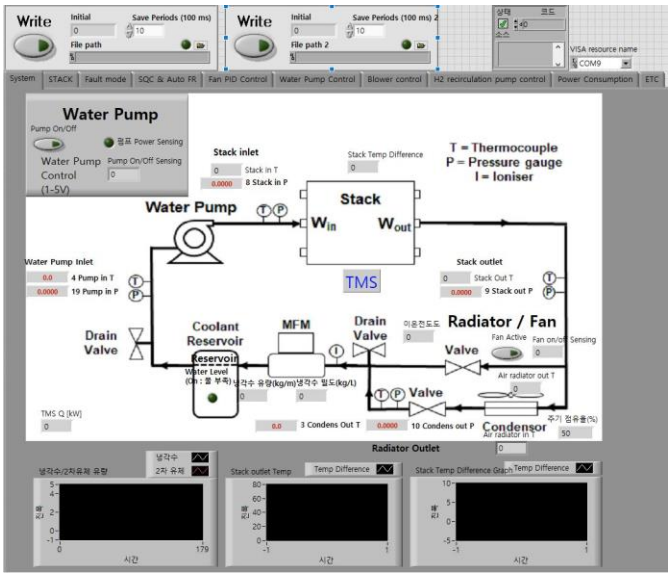

(c) Thermal management system

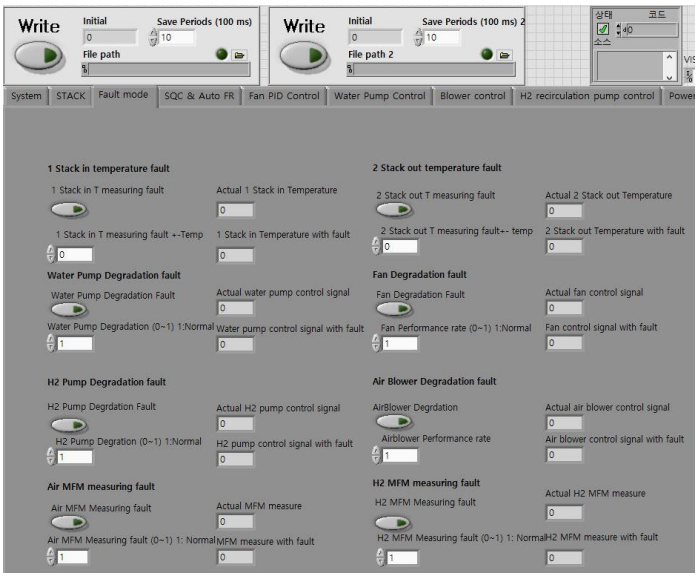

(d) Fault control

Figure 2.7 PEMFC system control panel (a) Fuel providing system (b) Air providing system (c) Thermal management system (d) Fault control (Continued)

Table 2.4 PEMFC system operating conditions

Parameter	Values
Cathode operating pressure (bar)	1
Anode operating pressure (bar)	1.1
PID controlled cathode (Air) stoichiometric ratio	2.0
PID controlled anode (H_2) stoichiometric ratio	1.5
Stack coolant inlet temperature (℃)	60
Stack coolant outlet temperature (℃)	65
Ambient temperature (℃)	15~25
Ambient relative humidity (%)	30~70
Purge period (minutes)	10
Stack active area (cm^2)	200
Stack cell number	24
Stack current (A)	60, 80
Maximum stack power (W)	2400

The stack's maximum power (2,400W) is rated under the current load at 200 A. However, the stack is operated at two different current loads; 60 A and 80 A. As widely known, PEMFC's fuel efficiency decreases with the power increment. Also, with the power increment, heat dissipation load increases. It leads to a higher TMS parasite power. Therefore, in the point of the system, optimal load conditions with high fuel efficiency exist under low current region density. Moreover, PEMFC is recommended to operate voltage higher than 0.6 V to prevent fast degradation. In this context, commercial residential fuel cell system product (S-Fuel cell, Korea) operates between 0.2~0.4 A/cm^2, which corresponds to the expected voltage around 0.7 V. Targeting the 1 kW class mobile distributed power generation system, the PEMFC system in this paper operates under the current densities at 0.3 A/cm^2 and 0.4 A/cm^2. The expected stack voltage is between 16.6 ~17.2 V in normal operating conditions.

2.3.2 Fault scenarios

PEMFC system consists of a stack and multiple BOP subsystems. Each subsystem has probable faulty components that might bring failure to the system. Possible fault scenarios in each subsystem are organized in Fig. 2.8. The FPS and APS each have blower and mass flow meter (MFM) as faulty components. Pipe clogging and leakage or reactant are considered. For the TMS, faults on the water pump and fan are considered as well as the fault of thermocouples in the stack inlet and outlet. Also, pipe clogging and leakage are considered. Fouling of radiator and humidifier are considered as possible fault scenarios.

Faults on the PEMFC system can be categorized depending on its damage risk. In this paper, considered faults shown in Fig. 2.8 are categorized into three groups; minor faults, severe faults and critical faults. Categorized fault scenarios with fault severity are shown in Fig. 2.9. Since the purpose of the BOP system is to provide target condition for the stack, component's natural degradation or minor failures rarely affects the stack's performance or the durability. For example, natural degradation of the air blower does not affect the stack's operating condition, because fixed air flowrate is always checked. In this case, a higher control signal is sent to the air blower to compensate for its degradation. Likewise, minor faults are often fixable. A list of minor fault

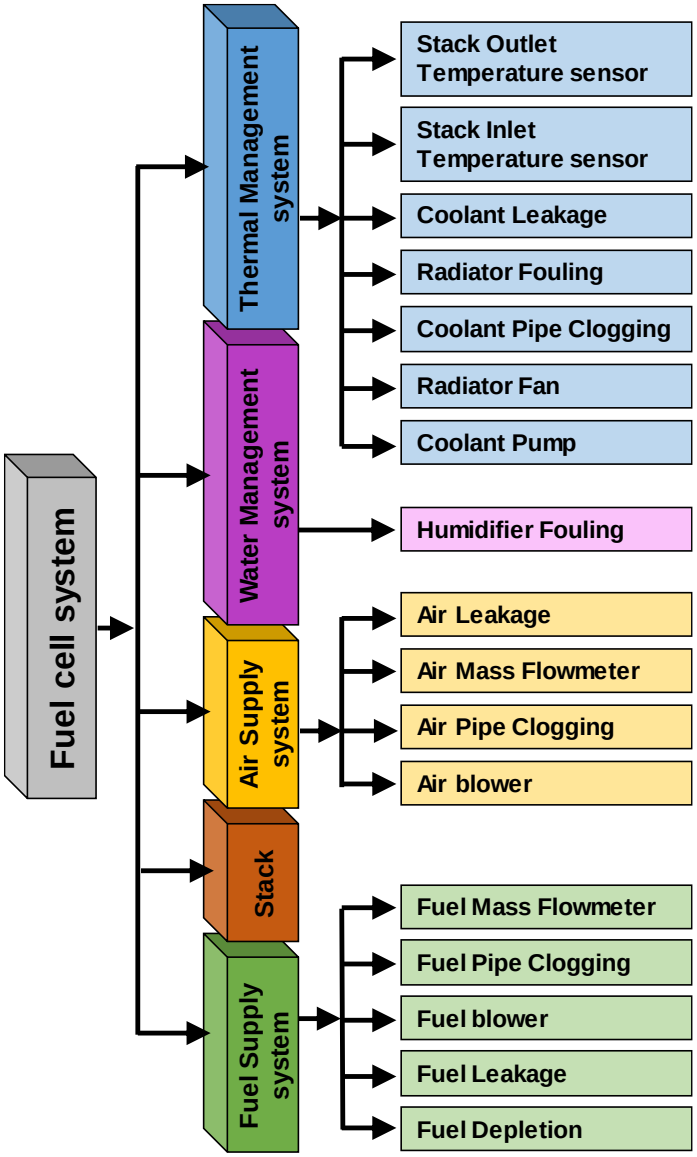

Figure 2.8 Probable fault scenarios in PEMFC subsystems

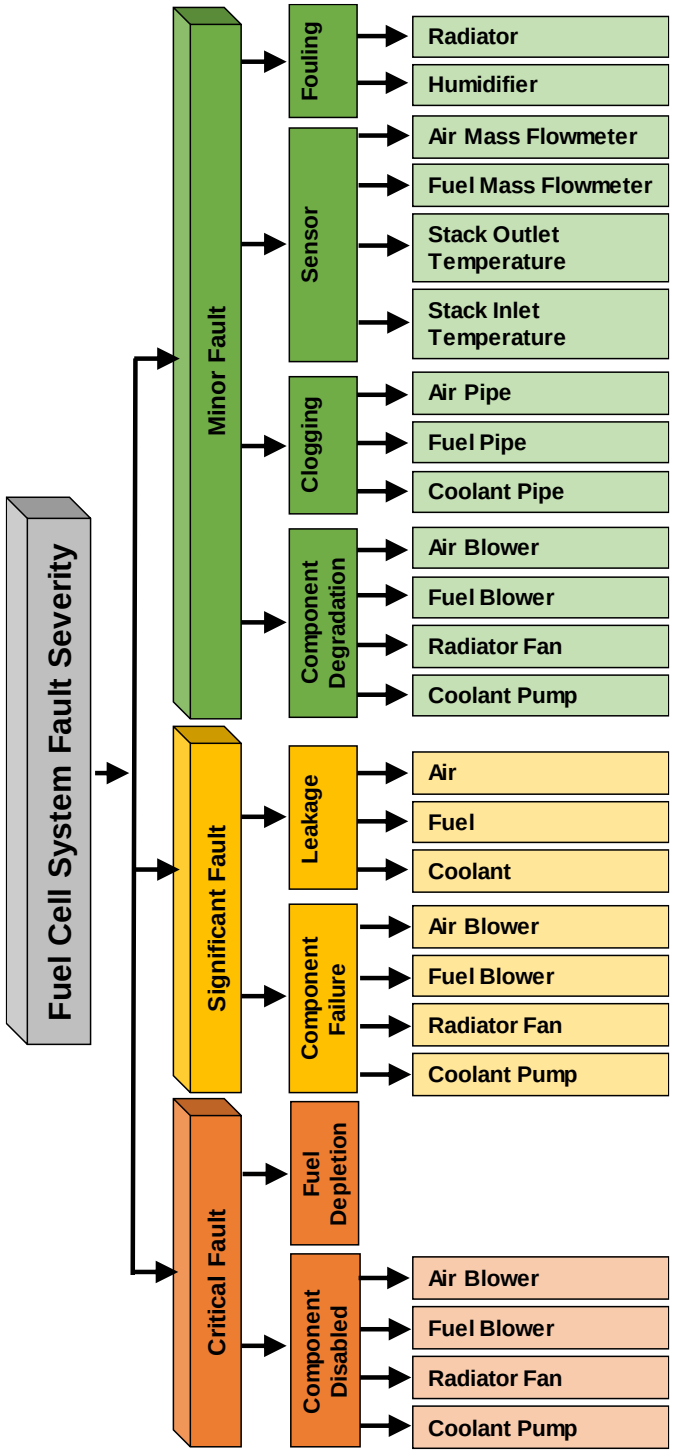

Figure 2.9 Severity-based fault scenarios in PEMFC subsystems

Table 2.5 Minor fault scenarios and corresponding simulation

Fault scenario	Fault label	Simulation method
Fuel pipe clogging	*MF1*	Increasing flow resistance using valve
Fuel flowmeter failure	*MF2*	Decreasing sensing signal 10~20%
Fuel blower degradation	*MF3*	Decreasing control signal 10~20%
Air pipe clogging	*MF4*	Increasing flow resistance using valve
Air flowmeter failure	*MF5*	Decreasing sensing signal 10~20%
Air blower degradation	*MF6*	Decreasing control signal 10~20%
Humidifier fouling	*MF7*	Increasing flow resistance using valve
Coolant pipe clogging	*MF8*	Increasing flow resistance using valve
Coolant inlet temperature sensor failure	*MF9*	Decreasing sensing temperature 0.5~1°C
Coolant outlet temperature sensor failure	*MF10*	Decreasing sensing temperature 1°C
Coolant pump degradation	*MF11*	Decreasing control signal 10~20%
Radiator fan degradation	*MF12*	Decreasing control signal 10~20%
Radiator fouling	*MF13*	Blocking heat transfer area 50%, Increasing flow resistance using valve

scenarios and their simulation methods are suggested in Table 2.5. The minor faults in FPS (*MF1~MF3*), APS (*MF4~MF7*) and TMS (*MF8~MF13*) are introduced.

Humidifier fault is grouped with APS faults because the humidifier is included in the APS of this PEMFC system. Clogging faults in each subsystem are simulated by increasing flow resistance with valves located in each subsystem loop. Flowmeter faults in APS and FPS are simulated by reading 90% of the signal sent from the flowmeter. Faults in TMS temperature sensors are simulated by reading lower values (0.5~1^{o}C) than the actual values. Degradations of main mechanical moving components in each subsystem are simulated by sending lower control signals to the components. Fouling of humidifier is simulated by blocking the half area of the membrane path with tape. Fouling of heat exchanger is simulated by blocking the heat exchange and increasing the flow resistance with valves located at the inlet and outlet of the radiator.

While the minor faults do not affect the stack or fixable by adjusting control logic, the other faults might bring significant problems to the stack. Faults that induce the unstable operating condition are categorized as significant faults and are listed in Table 2.6. Severe degradation of the main components in each subsystem threatens sufficient reactant supply (*SF2*&*SF4*) or stable thermal

Table 2.6 Significant fault scenarios and corresponding simulation

Fault scenario	Fault label	Simulation method
Fuel leakage	*SF1*	Opening venting valve in FPS
Fuel blower failure	*SF2*	Decreasing control signal 65~75% (Unable to satisfy anode SR 1.5)
Air leakage	*SF3*	Opening venting valve in APS
Air blower failure	*SF 4*	Decreasing control signal 25~55% (Unable to satisfy cathode SR 2.0)
Coolant leakage	*SF5*	Opening drain valve in TMS
Coolant pump failure	*SF6*	Decreasing control signal 30~50% (Unable to maintain 5^{o}C temperature difference)
Radiator fan failure	*SF7*	Decreasing control signal 65% (Unable to maintain stack inlet temperature at 60^{o}C)

control (*SF6*&*SF7*). Failures of the components (*SF2, SF4, SF6, SF7*) are simulated by sending the reduced control signal to the components. Hydrogen leakage (*SF1*) is related to safety issues and performance decrement of the stack. Since the cathode SR is very crucial to the stack performance, air leakage (*SF3*) reduces the performance and durability of the stack. When the coolant is insufficient (*SF5*), MEA is expected to dry out due to the temperature rise. Leakage faults are simulated by opening the valves in each subsystem.

Faults that bring complete failures to the stack are categorized as critical faults in this system. Five different critical fault scenarios are list in Table 2.7. When a critical fault occurs, the entire PEMFC system should be shut down immediately. For example, when the fuel blower or air blower is disabled (*CF1*&C*F3*), the stack cannot operate due to reactant starvation. Also, when the fuel tank is empty (*CF2*), the reaction of the stack stops. In these cases, other normal functioning subsystems should be stopped to prevent membrane drying or reduce parasitic power consumption. Failure of the thermal control is also critical to the stack. When the coolant pump or the radiator is disabled (*CF4*&C*F5*), the temperature rapidly increases. Complete disability of the components (*CF1, CF3, CF4, CF5*) is simulated by disconnecting the power line using a relay. Depletion of the fuel is simulated by closing the fuel tank valve.

Table 2.7 Critical fault scenarios and corresponding simulation

Fault scenario	Fault label	Simulation method
Fuel blower disabled	*CF1*	Disconnecting power supply to the fuel blower with relay
Fuel depletion	*CF2*	Closing the fuel tank valve
Air blower disabled	*CF3*	Disconnecting power supply to the air blower with relay
Coolant pump disabled	*CF4*	Disconnecting power supply to the pump with relay
Radiator fan disabled	*CF5*	Disconnecting power supply to the fan with relay

2.3.3 Fault response of PEMFC system

The priority of the PEMFC BOP system is to secure the operating conditions for the stack. Only when the operating condition is secured, performance and durability of the stack are also secured. In this context, the BOP system is controlled to satisfy the requirements for the stack operation. Reminding the fact, the fault scenarios in Table 2.5, Table 2.6 and Table 2.7 simulated with the PEMFC system shown in Fig. 2.5. The fault responses are investigated with the control/sensing signal changes in the form of standardized residuals. The collected signals are transformed to the standardized residuals (*std residuals*) with Eq. 2.1.

$$std\ \ residuals = \frac{Signal_{observed} - Signal_{normal\_state}}{Standard\ \ devitaion_{normal\_state\_signal}} \quad (2.1)$$

The fault responses in the FPS at 80 A are presented in Fig. 2.10. Fig. 2.10(a) represents the standardized residuals of the fuel blower control signal fuel flow rate signal. Fig. 2.10(b) represents that of the regulator pressure, stack inlet pressure and stack outlet temperature in FPS. The state of the FPS system is repeatedly changed from a normal state to a fault state and a fault state to a normal state. The state of the system is suggested below the graph.

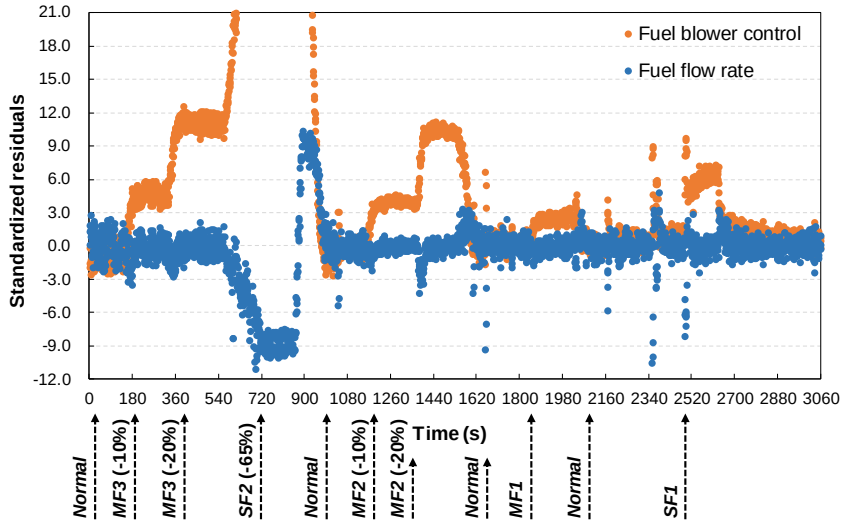

(a)

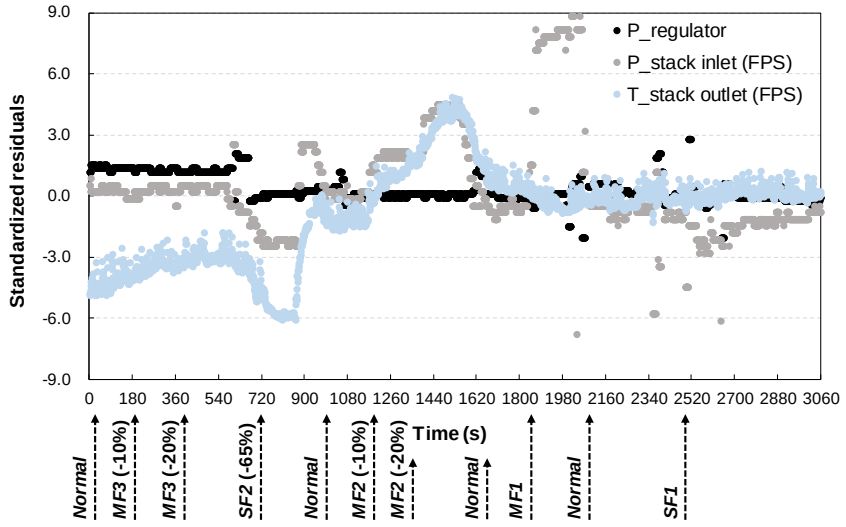

(b)

Figure 2.10 Fault response in fuel providing system at 80A

(a) Blower and MFM (b) Pressure and temperature

With the fuel blower degradation (*MF3*), the blower control signal increased. The standardized residual of the signal increased step by step with the increase of degradation rate from 10% to 20% and 65%. The performance decrement of the blower is compensated with the overload. When the degradation rate exceeded the control range (*SF2*), the fuel flow rate signal (MFM signal) decreased with the stack inlet pressure and stack outlet temperature. Lessen fuel flow rate induced the FPS pressure difference drop and temperature drop. Under the failure of the fuel flowmeter (*MF2*), on the other hand, the actual fuel flow rate increases and the signals move toward the opposite. Under the FPS clogging (*MF1*), pressure difference increases due to the increased flow resistance, and overload is applied to the FPS blower. Lastly under the situation of fuel leakage (*SF1*) between the FPS blower and FPS fuel flow meter (MFM), overall FPS pressure decreases. Due to the decrement, actual pressure at the FPS inlet decreases, and the pressure difference with the regulator reduces. The control signal of the FPS blower increases to pump additional fuel to the ambient. The fault response in the FPS system at 60 A follows a similar trend to that of the 80 A.

The fault responses in the APS at 80 A are presented in Fig. 2.11. Responses of the air blower outlet pressure, stack inlet temperature, airflow rate signal and blower control signal are mainly investigated. Same for the case of APS, the fault experiments are performed by switching normal state and fault states.

Under the normal state, standardized residuals of the signals are mostly between -2.0 and 2.0. Under the degradation of air blower (*MF6*), only the air blower control signal rises to compensate for its degraded performance. When the degradation proceeds out of the control range (*SF4*), the APS MFM signal decreases due to insufficient airflow. Reduced airflow is also reflected in the air blower outlet pressure. In the case of air flowmeter failure (*MF5*), the APS MFM signal under senses the flow rate. Therefore, the actual airflow rate should be increased to satisfy the required airflow measure in the MFM. With an elevated airflow rate level, the blower is overloaded and reflected in the pressure sensor. Stack inlet air temperature increases due to the increased heat and mass transfer in the humidifier.

Clogging in APS (*MF4*) shows a similar response to the clogging in FPS. Pressure and blower control signal rises with the elevated flow resistance. Air leak between the humidifier and stack (*SF3*) reduces the air supply to the stack. Due to the leak, control signal and pressure decreases as well as temperature

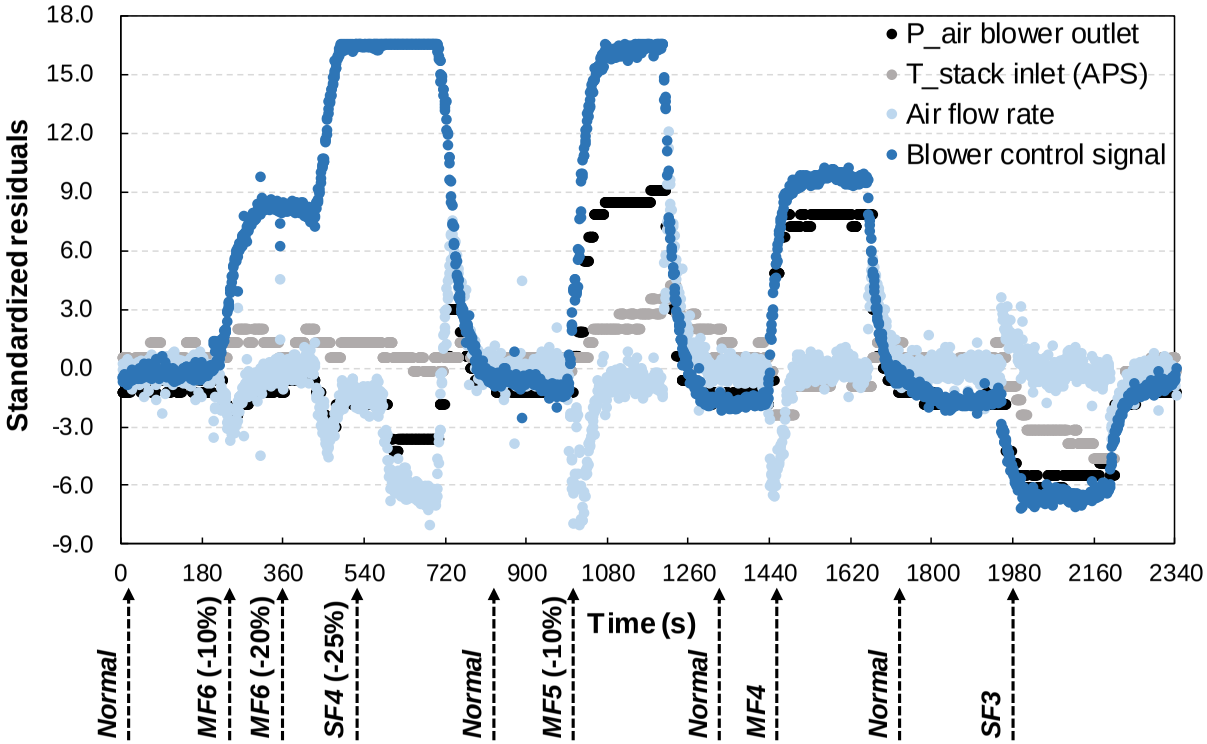

Figure 2.11 Fault response in air providing system at 80 A

The fault responses in the TMS system at 80 A are presented in Fig. 2.12. Responses of stack inlet pressure, stack inlet and outlet temperatures, pump and fan control signals are mainly observed. The first-hour fault responses and the second-hour fault responses are shown in Fig. 2.12(a) and Fig. 2.12(b).

Under the normal state, standardized residuals of the signals stay near zero. With the degradation of the radiator fan (*MF12*), the control signal slowly increases, but no significant changes are shown. It is my opinion that the standard deviation of the fan control signal is relatively larger than that of the other signals. So the change of the fan control signal residual is not clearly shown. When the fan suffers from severe degradation (SF7), generated heat from the stack is not sufficiently removed. Therefore, the fan control signal rapidly increases, but the stack inlet and outlet temperatures rise (small fluctuations are shown).

In the case of gradual pump degradation (*MF11*), the pump control signal gradually increases to maintain the temperature gap over the fuel cell. When the pump confronts its limitation due to the severe degradation (*SF6*), pressure drops with the coolant flowrate decrement. Also, the stack outlet temperature slowly increases. Under the TMS clogging (*MF8*), pressure and pump control signal increase like the clogging faults in the FPS and APS. Under the radiator fouling (*MF13*), both responses of fan degradation (*MF12*) and clogging (*MF8*)

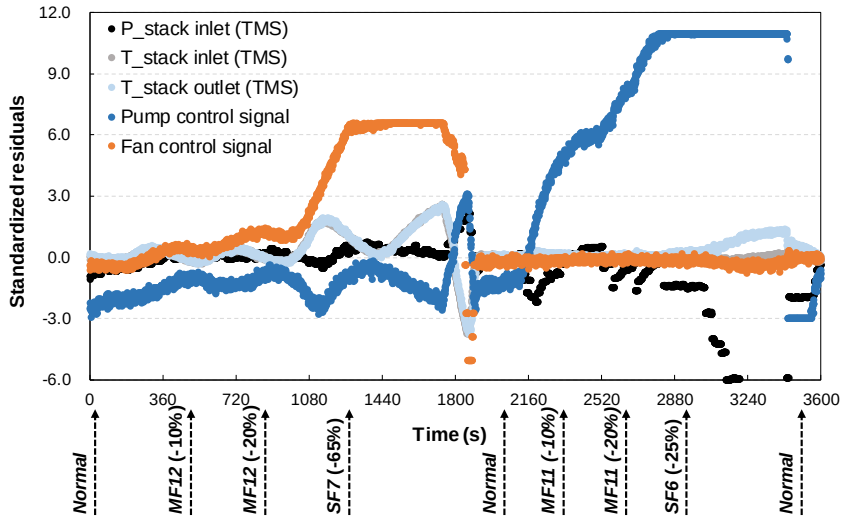

(a)

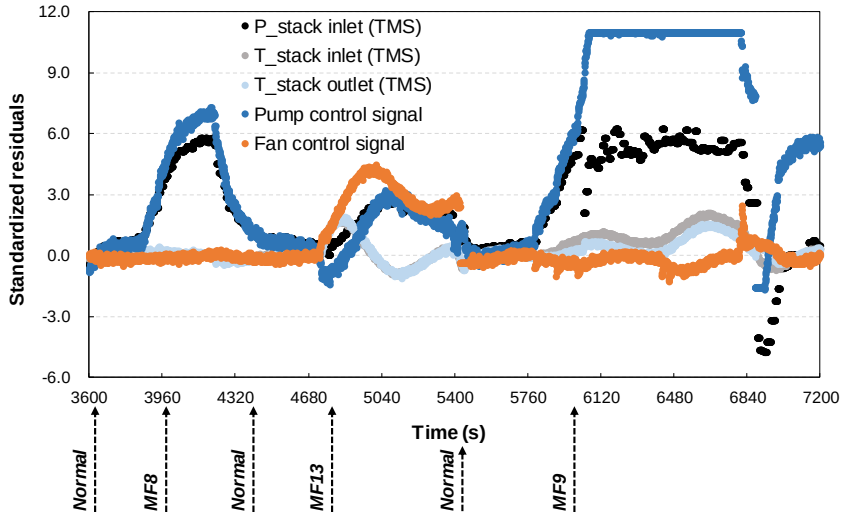

(b)

Figure 2.12 Fault response in thermal management system at 80A

(a) First-hour (b) Second-hour

are observed. Failure of the stack inlet temperature sensor (*MF9*) underestimates the temperature. Under the situation, the actual temperature gap is decreased, which means that the coolant flow rate should be increased. TMS pressure is then increased. Also, the fuel's outlet temperature increases since the FPS outlet is on the same side as the coolant inlet.

The fault responses in the FPS, APS and TMS show a similar response the degradation, clogging, sensor failure. Also, when a fault degree is elevated, the magnitude of responding signal residuals also elevates. Fault responses in the TMS are relatively slower than fault responses in the FPS and APS.

The overall responses to the fault scenarios suggested in this chapter are shown in Table 2.8, Table 2.9 and Table 2.10. The increase and decrease of the signal changes in response to the faults are represented with plus and minus symbols. Minor faults response, significant faults response and critical faults response are shown in Table 2.8, Table 2.9 and Table 2.10, respectively.

Table 2.8 Minor fault residual response

Fault Scenario	Sensor & Control Signals														
	Thermal management system						Air providing system				Fuel providing system				
	P_stack inlet (TMS)	T_stack inlet (TMS)	T_stack outlet (TMS)	Pump control signal	Fan control signal	Reservoir level sensor	P_air blower outlet	T_ stack inlet (APS)	Air flow rate	Blower control Signal	P_regulator	P_stack inlet (FPS)	T_stack outlet (FPS)	Fuel flow rate	Fuel blower control signal
Normal	0	0	0	0	0	0	0	0	0	0	0	0	0	0	0
MF1	0	0	0	0	0	0	0	0	0	0	0	+	0	0	+
MF2	0	0	0	0	0	0	0	0	0	0	0	+	+	0	+
MF3	0	0	0	0	0	0	0	0	0	0	0	0	0	0	+
MF4	0	0	0	0	0	0	+	0	0	+	0	0	0	0	0
MF5	0	0	0	0	0	0	+	+	0	+	0	0	0	0	0
MF6	0	0	0	0	0	0	0	0	0	+	0	0	0	0	0
MF7	0	0	0	0	0	0	+	-	0	+	0	0	0	0	0
MF8	+	0	0	+	0	0	0	0	0	0	0	0	0	0	0
MF9	+	0	0	+	0	0	0	0	0	0	0	0	+	0	0
MF10	-	0	0	-	0	0	0	0	0	0	0	0	0	0	0
MF11	0	0	0	+	0	0	0	0	0	0	0	0	0	0	0
MF12	0	0	0	0	+	0	0	0	0	0	0	0	0	0	0
MF13	+	0	0	+	+	0	0	0	0	0	0	0	0	0	0

Table 2.9 Significant fault residual response

Fault Scenario	Sensor & Control Signals														
	Thermal management system						Air providing system				Fuel providing system				
	P_stack inlet (TMS)	T_stack inlet (TMS)	T_stack outlet (TMS)	Pump control signal	Fan control signal	Reservoir level sensor	P_air blower outlet	T_ stack inlet (APS)	Air flow rate	Blower control Signal	P_regulator	P_stack inlet (FPS)	T_stack outlet (FPS)	Fuel flow rate	Fuel blower control signal
Normal	0	0	0	0	0	0	0	0	0	0	0	0	0	0	0
SF1	0	0	0	0	0	0	0	0	0	0	0	-	0	0	+
SF2	0	0	0	0	0	0	0	0	0	0	0	-	-	-	+
SF3	0	0	0	0	0	0	-	-	0	-	0	0	0	0	0
SF4	0	0	0	0	0	0	-	0	-	+	0	0	0	0	0
SF5	0	0	0	0	0	+	0	0	0	0	0	0	0	0	0
SF6	-	0	0	+	0	0	0	+	0	0	0	0	0	0	0
SF7	0	+	+	0	+	0	0	+	0	0	0	0	+	0	0

Table 2.10 Critical fault residual response

Fault Scenario	Sensor & Control Signals														
	Thermal management system						Air providing system				Fuel providing system				
	P_stack inlet (TMS)	T_stack inlet (TMS)	T_stack outlet (TMS)	Pump control signal	Fan control signal	Reservoir level sensor	P_air blower outlet	T_ stack inlet (APS)	Air flow rate	Blower control Signal	P_regulator	P_stack inlet (FPS)	T_stack outlet (FPS)	Fuel flow rate	Fuel blower control signal
Normal	0	0	0	0	0	0	0	0	0	0	0	0	0	0	0
CF1	0	0	0	0	0	0	0	0	0	0	0	-	0	-	+
CF2	0	0	0	0	0	0	0	0	0	0	-	0	0	-	+
CF3	0	0	0	0	0	0	-	0	-	-	0	0	0	0	0
CF4	-	0	0	+	0	0	0	0	0	0	0	0	0	0	0
CF5	0	+	+	0	+	0	0	+	0	0	0	0	+	0	0

2.4 Summary

In this chapter, fault responses of 1 kW PEMFC stack and 1 kW PEMFC system are investigated. To observe the effect of the fault clearly, the 1 kW stack is operated at its maximum performance. With the reduced hydrogen and air supply, the performance of the stack decreased fast. Other than the voltage, pressure sensors reacted to the faults. For the failure of the thermal management case, pressure and temperature sensors reacted to the faults. With the stack fault experiment, an insight that fault brings changes to the sensors in the system is gained.

Fault experiments are also performed with the 1 kW PEMFC system. Seventeen different fault scenarios are set and grouped depending on their fault severity to the system. Fault response and reacting control and sensing signals to the corresponding faults are analyzed. Overall, responses of thermal management system faults are slower than those of the fuel providing system and air providing system. Also, when a fault degree is more severe, the corresponding response is faster and its magnitude is larger. The increments and decrements of the control and sensing signals to the faults are tabularized.

Chapter 3. Severity-based fault diagnosis of 1 kW PEMFC system

3.1 Introduction

In general, maintenance actions are followed after the fault diagnosis. Typical fault diagnosis procedures and following maintenance actions are depicted in the flow chart Fig. 3.1. During a PEMFC system operation, the system maintains its normal state. The sensing data or control signal data are collected and transformed to put into the diagnosis algorithm. The diagnosis algorithm then monitors the state of the PEMFC system. When a fault occurs, the algorithm detects the abnormal state and classifies the fault. After the fault type is known, a fault assessment is made. Depending on its severity, maintenance decision also varies. If the fault is critical to the system, a decision is made to stop the whole system immediately. If the fault has significant effects on the system (or the stack), a decision can be made to change the operating strategy or stop the system with proper procedure. If the system suffers from minor faults, a maintenance decision can be made to overcome the problem using a control strategy or maintain the state. While many research papers focus on fault detection, fault classification and fault assessment, we have to remind

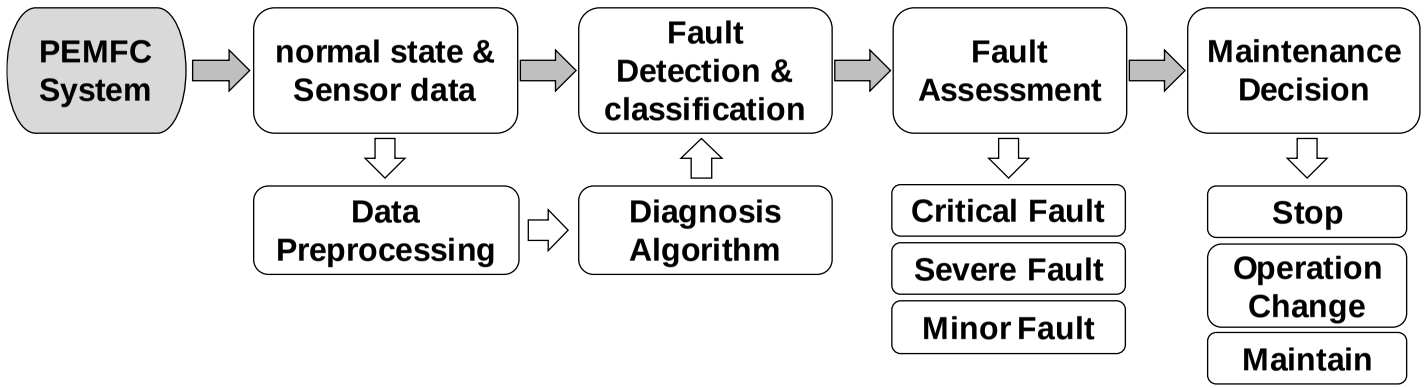

Figure 3.1 Fault diagnosis and maintenance decision flow chart

that taking action to prevent further damage to the stack or the system is important. Only when proper maintenance decisions and action proceed, the system can be protected.

In this sense, therefore, the concept of designing the fault diagnosis algorithm from the perspective of maintenance decisions is suggested and validated in this chapter. The conceptual schematics of hierarchical fault diagnosis and severity-based fault diagnosis are depicted in Fig. 3.2. The hierarchical fault diagnostic method locates fault in the subsystem level firstly [7]. Then, a faulty component is found. The severity-based fault diagnostic method detects the critical fault, significant faults and minor faults in series. This approach has several advantages. First, the fault assessment process can be omitted. Diagnosis results can be directly led to the maintenance actions. Second, the diagnosis algorithm can be designed considering the fault severity characteristics. For example, critical faults are easily detected, but the diagnosis results should be very accurate. Therefore, in this case, the algorithm can be developed focusing on its robustness.

The detailed development process of the severity-based fault diagnosis algorithm is explained in the chapter. Also, the diagnosis result with the algorithm is validated with fault experiment data from chapter 2.

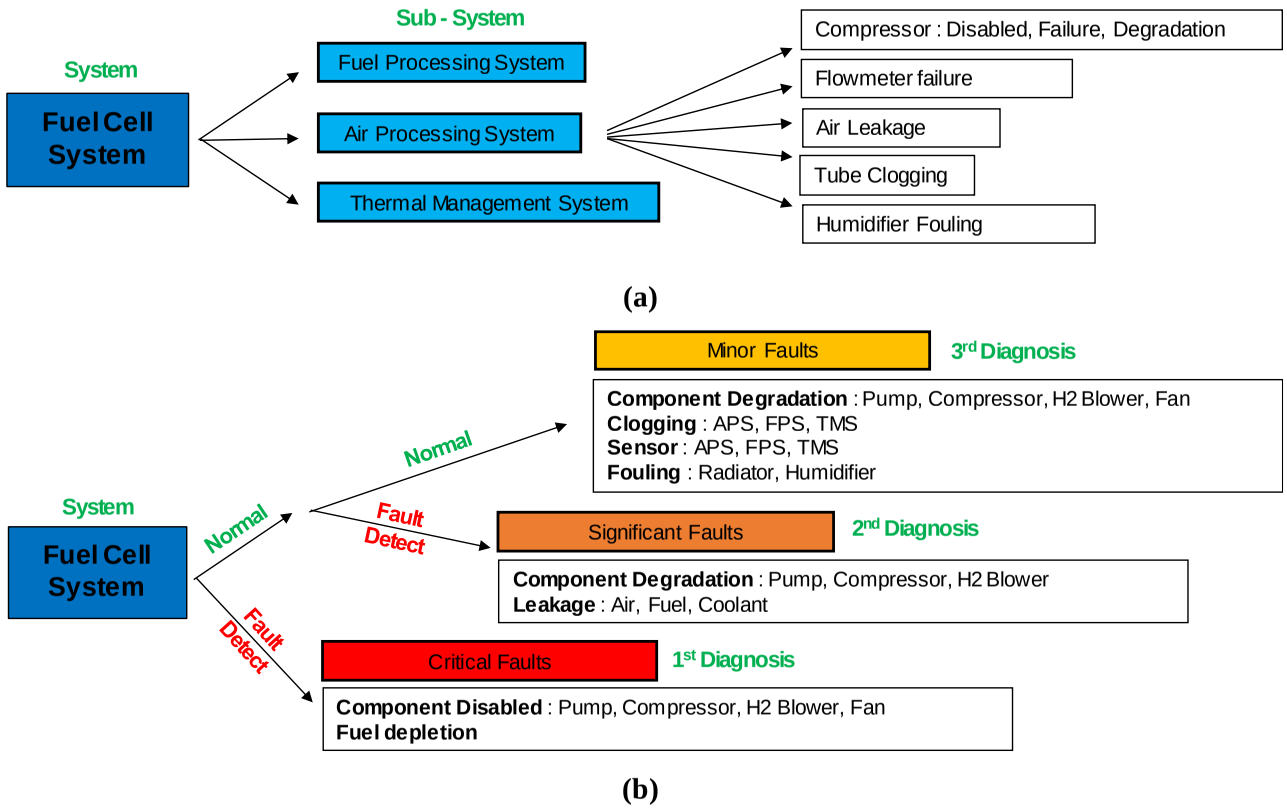

Figure 3.2 PEMFC system fault diagnostic method (a) Hierarchical diagnosis (b) Severity-based diagnosis

3.2 Fault residual patterns

3.2.1 Input variables

Reminding chapter 2, when a fault occurs, its response is reflected in the system's control signals or sensors. So, if we implement enough sensors at the right point, any faults are detectable. Unfortunately, however, the number of implemented sensors and their types are very limited in a commercial fuel cell system. Increased sensors elevate the cost of the system. In this sense, sensors used as input for the diagnosis algorithms in this paper are selected on a minimum scale.

In FPS, pressure transmitters located at the regulator outlet (which is also the position of the fuel blower inlet) and stack inlet are used. For the temperature, stack outlet fuel temperature is sensed. Fuel flow rate from the flow meter (target value) and fuel blower signal (control value) are also used as inputs. In APS, the pressure transmitter located between the air blower and flow meter is used. The thermocouple located between the humidifier and stack inlet is used as input to diagnose APS. Airflow rate from the flow meter (target value) and air blower signal (control value) are also used. In TMS, coolant pump outlet pressure is monitored with a pressure transmitter and used as input. A signal from the reservoir level sensor is also monitored in binary values. Temperatures

at both stack inlet and outlet (target values) and control signals of the coolant pump and radiator fan (control values) are used as inputs.

3.2.2 Normal state

As repeatedly mentioned, there are always changes to the sensing signals or control signals with faults. Before the changes, there has to be a reference state, which is the normal state of the PEMFC system. There are two methods to acquire normal state data, as shown in Table 3.1.

The first method is using an empirical model. If the target current load is set, corresponding target SRs are also fixed on both anode and cathode. So the required reactant flow rates are obtained with simple equations. Then, pressure drops due to the flows are acquired with the P-Q curves of anode and cathode. The anode outlet temperature is affected by current load, fuel flow rate, stack inlet operating temperature and ambient temperature. Since the PEMFC system mostly operates under fixed conditions, the relation between the anode outlet and those parameters can be expressed in simple equations. Using a neural network model can also be another simple solution. Same for the APS, the normal state cathode inlet temperature can be acquired with current load, airflow rate, ambient temperature as inputs. For TMS, the coolant flow rate

Table 3.1 Normal state prediction

Subsystem	Input	Output	Sensor
Stack	Current	Voltage	Voltage sensor
Fuel providing system (FPS)	Current	Fuel flow rate	Fuel flow rate MFM
	Fuel flow rate	Anode pressure difference	P_stack inlet (FPS)
	Fuel flow rate, Anode pressure	Fuel blower control signal	Fuel blower control signal
	Current, Anode pressure, Fuel flow rate, Ambient temperature	Fuel stack outlet temperature	T_stack outlet (FPS)
	-	Anode pressure	P_regulator
Air providing system (APS)	Current	Air flow rate	Air flow rate MFM
	Air flow rate	Cathode pressure difference	P_blower outlet (APS)
	Air flow rate, Cathode pressure	Air blower control signal	Air blower control signal
	Current, Cathode pressure, Air flow rate, Ambient temperature	Air stack inlet temperature	T_stack inlet (APS)
Thermal management system (TMS)	-	Coolant inlet temperature	T_stack inlet (TMS)
	-	Coolant outlet temperature	T_stack outlet (TMS)
	Current, Ambient temperature	Heat geration rate, Coolant flow rate	
	Coolant flow rate	TMS pressure	P_stack inlet (TMS)
	Coolant flow rate, TMS pressure	Pump control signal	Pump control signal
	Coolant flow rate, Ambient temperature, Heat geration rate	Fan control signal	Fan control signal
	-	Coolant level	Reservoir level sensor

should be acquired. For that, the heat generation rate from that stack should be calculated with current load, stack voltage and ambient temperature. The stack voltage can be simply acquired from the stack polarization curve (I-V curve). When the heat generation rate is calculated, the required normal state coolant flow rate is also fixed. Then pressure drop of the TMS is acquired from the TMS P-Q curve. The control signal of a water pump is a function of coolant flow rate and pressure difference. The fan control signal is a function of the heat generation rate, the coolant flow rate and the stack outlet temperature.

The second method is to acquire normal state data is using experimental data. The reason for developing a fault diagnosis algorithm is to implement it in the system. Therefore, the test data should exist in the process of system development. The easiest method to obtain the normal state data is using the test data. Either way, standard deviations of sensing/control values are also required to develop the severity-based fault diagnosis algorithm. Therefore in this study, this second method is used to set the normal state.

3.2.3 Fault residual pattern table

Considering that the fault makes changes to the sensors, expected residual patterns should be made into tables. Table 3.2 shows the expected fault response to the minor fault scenarios in Table 2.5. Table 3.3 and Table 3.4 represents expected fault responses to the significant faults and critical faults list in Table 2.6 and Table 2.7, respectively. When the signals are expected to increase with the fault, the value one is put into the corresponding spot. When the signals are expected to decrease, the value minus one is put into the corresponding spot. The value zero means non-expected changes with the fault.

In Table 3.2, signals at the normal state are not expected to change. When the flow resistance of FPS increases (*MF1*), the pressure difference over the fuel cell increases as well as the fuel blower control signal. In the case of fuel flowmeter failure, the flow is measured less than its real value. Therefore, the fuel blower signal has to rise for more fuel flow. Then, differential pressure over the FPS rises. Also, stack outlet fuel temperature increases due to the increment of fuel recirculated hydrogen portion and thermal inertia. Similar trends are shown in the fault scenarios in APS (*MF4*, *MF5*, *MF6*). With the humidifier fouling fault (*MF7*), air blower control signal and pressure difference increase due to the increased flow resistance and stack inlet temperature of the air decreases due to the reduced humidifying capability.

Table 3.2 Minor fault residual patterns

Fault Scenario	Sensor & Control Signals														
	Thermal management system						Air providing system				Fuel providing system				
	P_stack inlet (TMS)	T_stack inlet (TMS)	T_stack outlet (TMS)	Pump control signal	Fan control signal	Reservoir level sensor	P_air blower outlet	T_ stack inlet (APS)	Air flow rate	Blower control Signal	P_regulator	P_stack inlet (FPS)	T_stack outlet (FPS)	Fuel flow rate	Fuel blower control signal
Normal	0	0	0	0	0	0	0	0	0	0	0	0	0	0	0
MF1	0	0	0	0	0	0	0	0	0	0	0	**1**	0	0	**1**
MF2	0	0	0	0	0	0	0	0	0	0	0	**1**	**1**	0	**1**
MF3	0	0	0	0	0	0	0	0	0	0	0	0	0	0	**1**
MF4	0	0	0	0	0	0	**1**	0	0	**1**	0	0	0	0	0
MF5	0	0	0	0	0	0	**1**	**1**	0	**1**	0	0	0	0	0
MF6	0	0	0	0	0	0	0	0	0	**1**	0	0	0	0	0
MF7	0	0	0	0	0	0	**1**	**-1**	0	**1**	0	0	0	0	0
MF8	**1**	0	0	**1**	0	0	0	0	0	0	0	0	0	0	0
MF9	**1**	0	0	**1**	0	0	0	0	0	0	0	0	**1**	0	0
MF10	**-1**	0	0	**-1**	0	0	0	**0/1**	0	0	0	0	0	0	0
MF11	0	0	**0/1**	**1**	0	0	0	0	0	0	0	0	0	0	0
MF12	0	0	0	0	**1**	0	0	0	0	0	0	0	0	0	0
MF13	**1**	0	0	**1**	**1**	0	0	0	0	0	0	0	0	0	0

Table 3.3 Significant fault residual patterns

Fault Scenario	Sensor & Control Signals														
	Thermal management system						Air providing system				Fuel providing system				
	P_stack inlet (TMS)	T_stack inlet (TMS)	T_stack outlet (TMS)	Pump control signal	Fan control signal	Reservoir level sensor	P_air blower outlet	T_ stack inlet (APS)	Air flow rate	Blower control Signal	P_regulator	P_stack inlet (FPS)	T_stack outlet (FPS)	Fuel flow rate	Fuel blower control signal
Normal	0	0	0	0	0	0	0	0	0	0	0	0	0	0	0
SF1	0	0	0	0	0	0	0	0	0	0	0	**-1**	0	0	**1**
SF2	0	0	0	0	0	0	0	0	0	0	0	**-1**	0	**-1**	**1**
SF3	0	0	0	0	0	0	**-1**	**0/-1**	0	**-1**	0	0	0	0	0
SF4	0	0	0	0	0	0	**-1**	**0/-1**	**-1**	**1**	0	0	0	0	0
SF5	0	0	0	0	0	**1**	0	0	0	0	0	0	0	0	0
SF6	**-1**	0	**1**	**1**	0	0	0	**1**	0	0	0	0	0	0	0
SF7	0	**1**	**1**	0	**1**	0	0	**1**	0	0	0	0	**1**	0	0

Table 3.4 Critical fault residual patterns

Fault Scenario	Sensor & Control Signals														
	Thermal management system						Air providing system				Fuel providing system				
	P_stack inlet (TMS)	T_stack inlet (TMS)	T_stack outlet (TMS)	Pump control signal	Fan control signal	Reservoir level sensor	P_air blower outlet	T_ stack inlet (APS)	Air flow rate	Blower control Signal	P_regulator	P_stack inlet (FPS)	T_stack outlet (FPS)	Fuel flow rate	Fuel blower control signal
Normal	0	0	0	0	0	0	0	0	0	0	0	0	0	0	0
CF1	0	0	0	0	0	0	0	0	0	0	0	**-1**	0	**-1**	**1**
CF2	0	0	0	0	0	0	0	0	0	0	**-1**	0	0	**-1**	**1**
CF3	0	0	0	0	0	0	**-1**	0	**-1**	**-1**	0	0	0	0	0
CF4	**-1**	0	0	**1**	0	0	0	0	0	0	0	0	0	0	0
CF5	0	**1**	**1**	0	**1**	0	0	**1**	0	0	0	0	**1**	0	0

Under TMS clogging (*MF8*), pressure drop over the TMS increases and the coolant pump signal rises to maintain its coolant flow rate. In case when the coolant stack inlet thermocouple's sensing value is lower than its true value (*MF9*), the actual temperature gap over the stack decreases. Then, the coolant flow rate should increase to remove the same amount of heat before the fault. The pump signal and TMS pressure are expected to elevate. Also, since the actual temperature is raised in the coolant inlet side, the outlet temperature of hydrogen is expected to increase. On the contrary, when the coolant outlet temperature sensor has a problem (*MF10*), the temperature gap over the stack is increased. Then, the coolant pump control signal and the TMS pressure are expected to decrease with a lower coolant flow rate. Also, if the actual stack outlet temperature increases, cathode air outlet temperature increases. This leads to the increased stack air inlet temperature due to the heat transfer in the humidifier. In the case of coolant pump degradation (*MF11*) and radiator fan degradation (*MF12*), the corresponding control signal is expected to rise to compensate for the degraded performance. With the radiator fouling (*MF13*), the responses of both radiator fan degradation (*MF12*) and TMS clogging (*MF8*) are expected at the same time.

There are seven significant fault scenarios considered in Table 3.3. When the fuel is leaked (*SF1*), fuel blower control signal increases due compensate

for the fuel loss to the ambient. Since the FPS is maintained at 0.1 bar gauge pressure, the FPS pressure difference decreases with the fault. When the fuel blower cannot sufficiently supply the required fuel (*SF2*), fuel flow rate and pressure difference decreases. A similar trend is expected with the air blower failure (*SF4*). Under SF4, stack inlet temperature can be decreased due to the reduced heat transfer with reduced air flow. Shen the air is leaked after the MFM (*SF3*), over all flow resistance decreases. Therefore, load on blower decreases as well as APS pressure. With decreased air flow, heat transfer rate can decrease and stack inlet temperature of the air can decrease. Leakage of coolant in TMS (*SF5*) is sensed with level sensor. Severe degradation of the coolant pump reduces the coolant flow rate. Pressure difference surely decreases and stack outlet temperature increases due to the insufficient coolant. Then, air outlet temperature increases and it elevates the inlet temperature of the air with heat transfer at the humidifier. In case of fan failure (SF7), temperatures at the TMS, FPS and APS all rise due to the heat removal failure.

There are five critical fault scenarios considered in Table 3.4. When the fuel blower is completely disabled (*CF1*), fuel flow rate rapidly decreases. With the decrement, pressure transmitter also senses the decreased pressure difference. Fuel blower control signal rises up with the decreased target flow rate but does not work. When the fuel is completely depleted (*CF2*), anode

outlet pressure decreases. In case of disabled air blower (*CF3*), disabled coolant pump (*CF4*) and disabled radiator fan (*CF5*), similar responses are shown with that of failure cases (*SF4, SF6, SF7*). But the responses are expected to be faster and have bigger residuals.

3.3 Fault diagnosis algorithm development

3.3.1 Severity-based fault diagnosis concept

A comparison example of fault responses under normal, minor fault, significant fault and critical fault are shown in Fig.3.3. Fig. 3.3(a) represents normal and coolant pump fault responses of stack inlet temperature. Fig. 3.3(b) represents normal and coolant pump fault responses of TMS pressure. (In the case of Fig. 3.3, abrupt faults are simulated rather than gradual faults. For instance, degradation of the fault is simulated by gradually decreasing the control signal sent to the coolant pump in chapter 2. In the case of Fig. 3.3, 20% of the control signal is reduced at once. The radiator fan is operated to maintain stack outlet temperature rather than stack inlet temperature in this case. Overall TMS line was shorter than the TMS loop in chapter 2.)

As shown, the residuals are faster and bigger as the fault gets severe. In other words, responses will be fast and big when critical faults occur. On the other hand, the system will response slow and relatively small to the minor faults. Focusing on the characteristics of the fault response, over all concept of the severity-based fault diagnosis algorithm is shown in Fig. 3.4. There are three neural networks in the algorithm. The first neural network (NN1) detects critical faults. The second neural network (NN2) detects the significant faults.

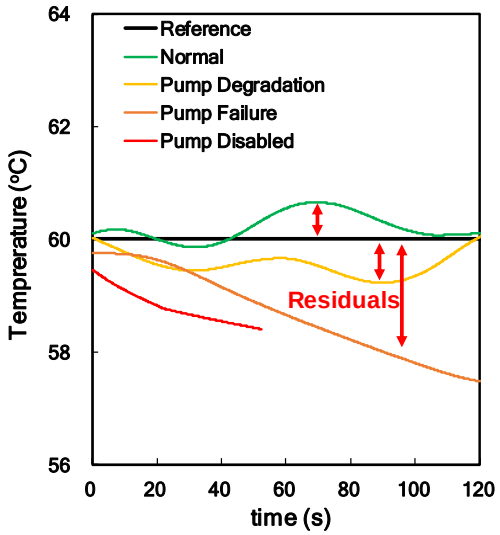

(a)

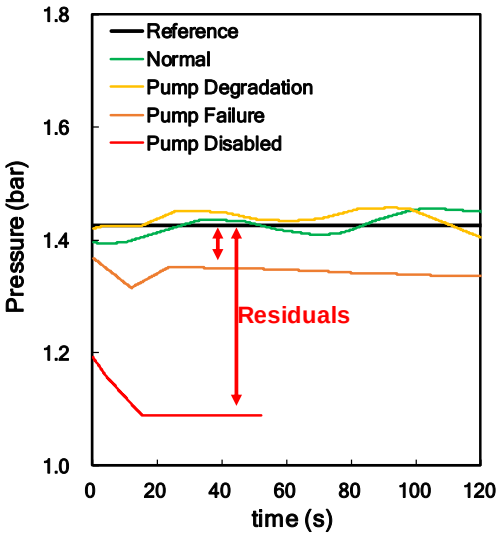

(b)

Figure 3.3 Response of TMS with different coolant pump fault severity (a) Stack inlet temperature (b) Stack inlet pressure

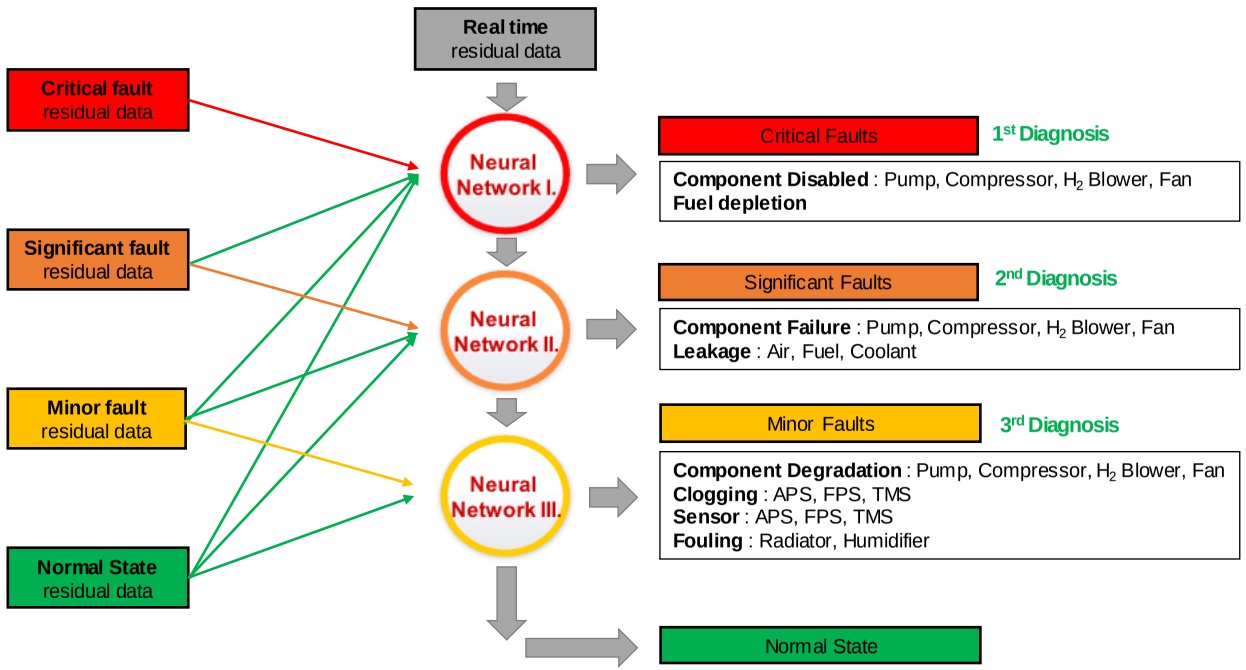

Figure 3.4 Severity-based fault diagnosis algorithm concept

The last neural network (NN3) detects minor faults and normal state. The real-time residual data from the system firstly enters the NN1. If the NN1 detects no the critical faults, the decision is passed on to the NN2. If the NN2 detects no the significant faults, the decision is passed on to the NN3. Lastly, NN3 detects minor faults or normal state. Diagnosis of each neural network is independently processed. Therefore, there are three decisions at each neural network. However, there are priorities to the higher severity class decision. For example, if NN2 detects leakage of air and NN3 detects clogging in the APS, the decision of NN2 is the final decision.

3.3.2 Algorithm development

Bringing sensational results in numerous research fields, artificial neural network (ANN) has proven to be a powerful pattern recognition tool and became mainstream in machine learning [17] . ANN, shortly neural network (NN), consists of multiple basic units; perceptron. A perceptron acts alone as a regressor or a binary classifier. When multiple perceptrons are connected, they become a strong classifier or regressor with high accuracy [17]. As introduced in the first chapter, there are many type of neural network. In the field of PEMFC fault diagnosis, neural network is actively applied. In this study, fully-connected multi-layer perceptron neural network (MLPNN), typical NN, is applied to diagnose the state of PEMFC system.

The fault scenarios and corresponding residual patterns are shown in previous chapters. The overall residual patterns are based on triple values; 0, +1 and -1. These fault residual patterns and corresponding fault classes are used to train neural network. For example, schematic structure of a neural network II (NN2) in Fig. 3.4 is shown in Fig. 3.5. the neural network consists of input layer, hidden layers and output layer. Input layer has 15 nodes (percenptrons), which corresponds to the number of input values. Input values are the control/sensor signal information in the PEMFC system. Output layer has eight nodes, which corresponds to the number of significant faults including the normal state. Hidden layer consists of three layers that each has 14, 12 and 10 nodes.

When the signal information is given to the NN2, each signal is transformed in to an appropriate form. Then the NN2 makes output in a form of 1 by 8 matrix. Each value in the matrix represents probability of normal and significant faults. The final state is determined by applying soft-max function to this matrix. In other words, the biggest value in the matrix represents the state of the PEMFC system. The NN1's hidden layer includes three layers (12-10-8) and output layer with six nodes. The NN3's hidden layer includes three layers (14-12-10) and output layer with 14 nodes.

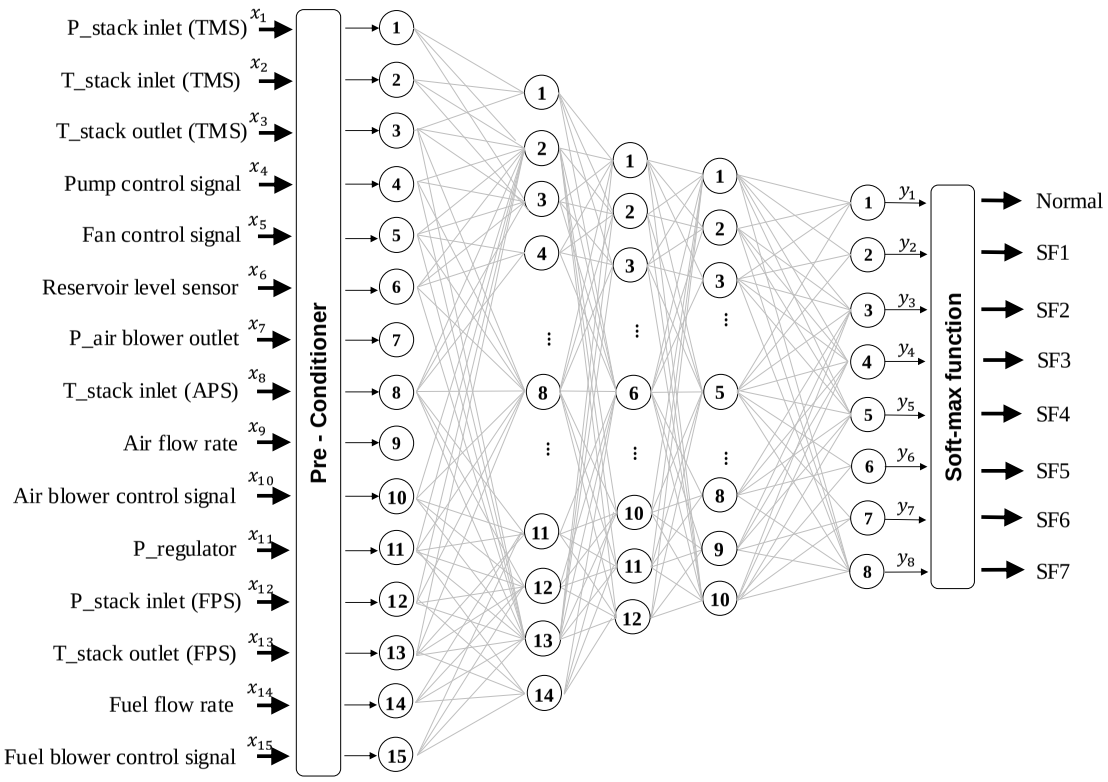

Figure 3.5 Structure of the neural network II (NN2, for significant faults)

The training and validation process for the severity-based fault diagnosis algorithm is shown in the flow chart Fig. 3.6. For the algorithm training, residual patterns are used as inputs and corresponding fault classes are used as outputs. For the NN3, which diagnoses minor faults, only minor fault residual data is used. For the NN2, significant data and minor data are used for the training. In this point, minor fault residual data is trained as normal state. For the NN3, all the fault residual data are used, but significant data and minor data are both treated as normal state. Since the sensing data has up and down during the real PEMFC system operation, the value '0' in the pattern is randomly transformed to the value between -0.5 to +0.5. With the randomness, the patterns are repeated trained to set appropriate weights for the neural networks. Also, since the NN3 should be very robust in detecting critical faults, significant data and minor data are divided into the proportional value with their divided standard deviations of input value to that of critical data. For instance, NN1 receives the data divided into 30 times of the data's standard deviation. NN2 and NN3 receive the 30 times of the data's standard deviations. Therefore, when in training, +1s and -1s in the residual patterns of significant and minor faults are trained with the value of +0.1 and -0.1.

To validate the diagnosis algorithm, system operation data is used. As described in the previous subchapters, the sensing/control signals should be

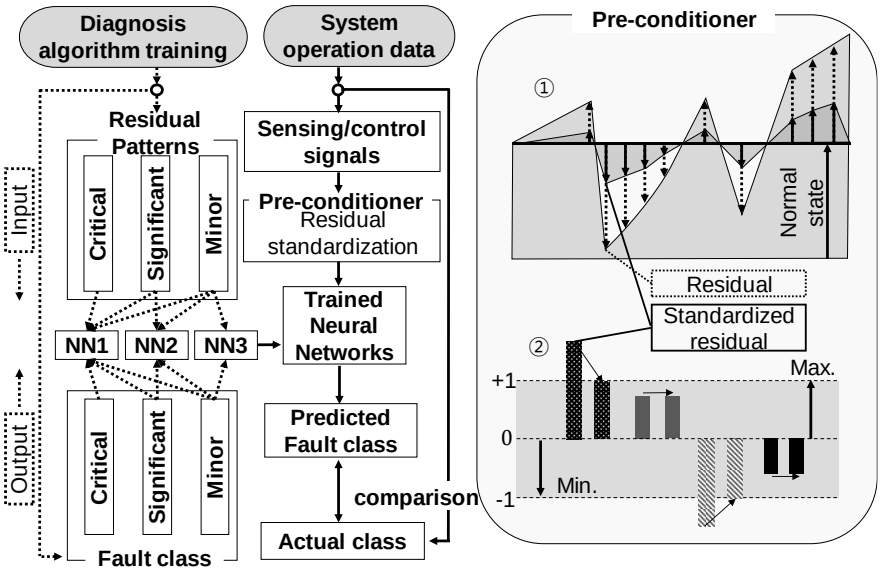

Figure 3.6 Training and validation process for the severity-based fault diagnosis algorithm

transformed into appropriate forms. The process is proceeded with pre-conditioner. First, the data is transformed to the residuals. The residuals are put into the all three neural networks (NN1, NN2 and NN3). Depending on the neural network, residuals are sometimes averaged and divided into the multiple value of standard deviation. For NN1, real-time data is used after dividing the residual with 30 times of its standard deviation. For NN2, 60 seconds averaged data is used after dividing the residual with 3 times of its standard deviation. For NN3, 180 seconds averaged data is used after dividing the residual with 3 times of its standard deviation. After the deviation, standardized residual is lastly adjusted. The neural network is only trained in the boundary of value -1 to +1. Therefore, the standardized residuals are cut into value +1 if it is bigger than the +1. If the value is smaller than the -1, the value is cut into -1.

Finally, the pre-conditioned data is put into the trained neural networks and predicted fault class is acquired. The results are compared with the actual state (actual class).

3.4 Fault diagnosis results

The fault experiments are performed under current load of 60 A and 80 A as explained in the chapter 2. The experiments are performed simultaneously repeating normal state and fault states. Diagnosis results of FPS at 60 A are presented in Fig. 3.7. Fig. 3.7(a) shows the diagnosis results of minor faults in FPS. X-axis represents operation time and Y-axis represents state of the PEMFC system. Actual state of the system firstly starts with normal state. The diagnosis algorithm detects the normal state after 180 seconds, due to the averaged data as input. Then, the actual state is changed to degradation of hydrogen blower (*MF3*). The algorithm also detects the MF3 after about three minutes. When the system goes back to the normal state, diagnosis algorithm also follows the normal state. After then, flow meter sensor offset of 10% (*MF2*) is correctly diagnosed as well as FPS clogging (*MF1*). Overall, minor faults in FPS at current load of 60 A are perfectly diagnosed. In Fig. 3.7(b), failure of the hydrogen blower (*SF2*) and hydrogen flow meter offset of 20% (*MF2*) are simulated. In the simulation of *SF2*, its sending signal is reduced from 0% to 50% and then to 75%. Due to the delay between the hydrogen blower and fault application, fault is miss-diagnosed in the transition from 0% to 50%. However, the algorithm diagnosed the *MF3* and *SF2* in turn. When the state is gradually recovered, *MF3* and normal state are correctly diagnosed. While the transition

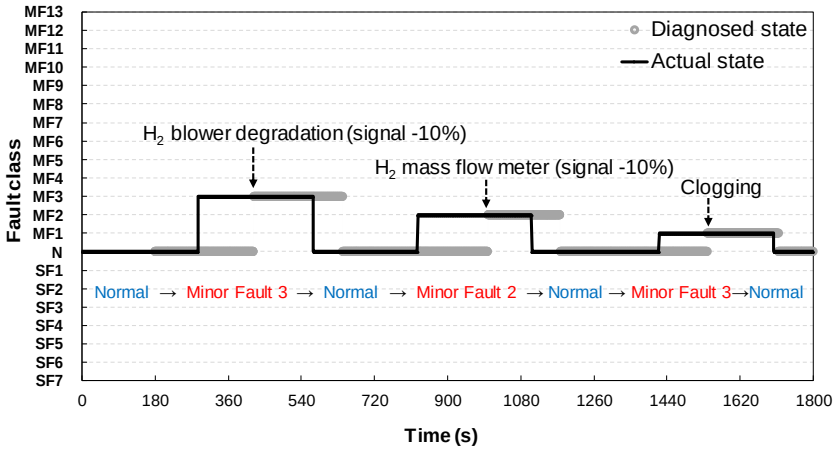

(a)

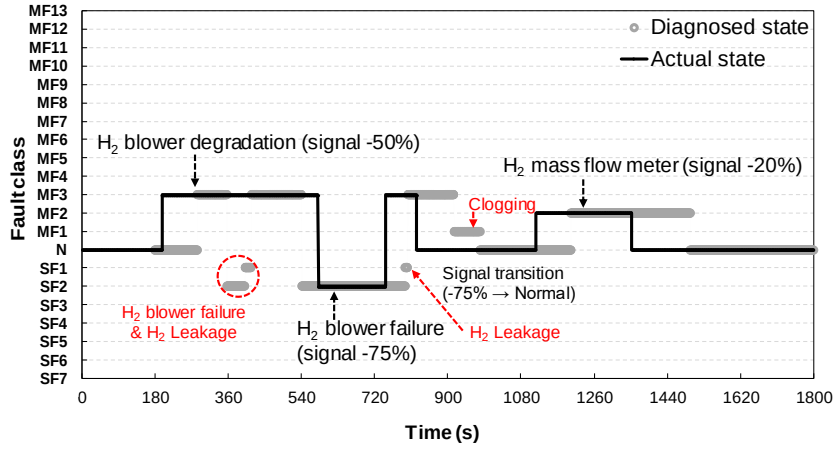

(b)

Figure 3.7 Fault diagnosis result in FPS at 60 A

(a) Minor faults (b) Significant faults

there is misdiagnosed state (*SF1* and *MF1*). Miss-diagnosis results can be interpreted with standardized residuals for significant fault neural network (Fig. 3.8(a)) and minor fault neural network (Fig. 3.8(b)). Looking at the significant fault residual pattern (Table 3.3), difference between *SF1* and *SF2* is residual of fuel flow rate. At about 800 seconds in Fig. 3.8(a), MFM signal rapidly rises faster than the other signals. At this point, NN2 shortly diagnoses the state as *SF1*. If the recovery from the *SF2* to *MF3* is proceeded slowly, this miss-diagnosis would not happen. Also for the miss-diagnosed case in the transition from *MF3* to normal state at about 950 seconds, pressure and MFM signal fluctuates upward. At the point, the residual pattern matches the FPS clogging shortly. After then, the normal state is correctly diagnosed. But, these miss-diagnosed results are no problem since our intention is to diagnose a fault state from the normal state, not the opposite. When in transition from the normal state to *MF2*, however, there is miss-diagnosis in the early stage. This is also due to the fast performed fault experiment. When the *MF2* is applied to the system, FPS stack outlet temperature changes slower than the hydrogen blower signal or FPS pressure. The gap between the response time makes the misdiagnosis of the algorithm. This is also not a problem, because real fault of hydrogen mass flow meter occurs with a long time period. Therefore, the response will be slow enough.

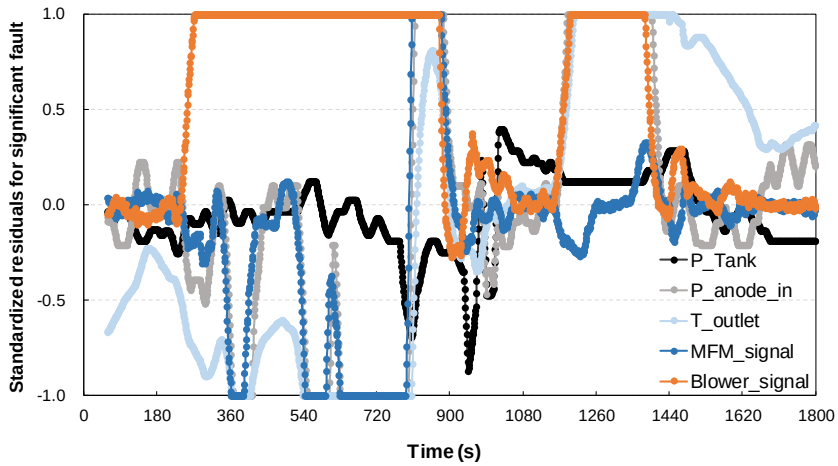

(a)

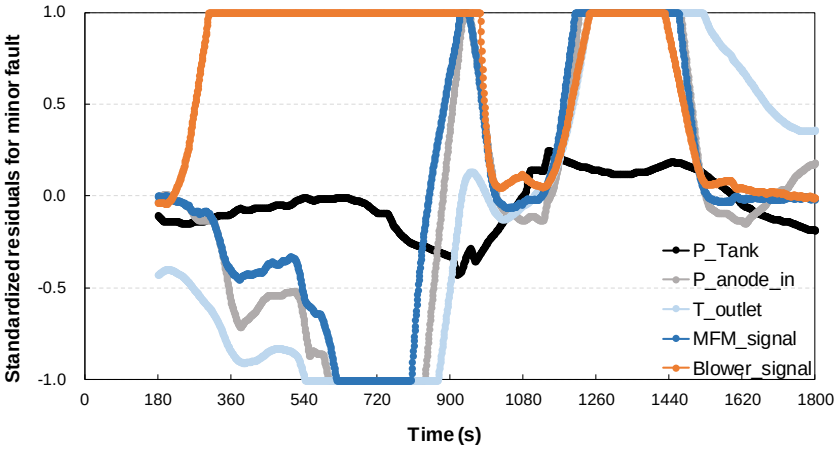

(b)

Figure 3.8 Standardized residuals for algorithm

(a) Residuals for NN2 (b) Residuals for NN3

The FPS fault diagnosis results at current load 80 A are presented in Fig. 3.9. This time, reduced control signal is sent to the hydrogen blower in gradual from 0% to 10%, to 20% and 65%. Then the reduced proportion is recovered back to the normal state. While the process, the algorithm correctly follows the actual state. When in transition from normal state to *MF2* at 1,260 seconds, miss-diagnosed states of *MF3* and *MF1* are shown before the *MF2*. This is due to the different response time of control signal, pressure and temperature. When the control signal rises first, *MF3* is diagnosed. Then, when the pressure follows the up, *MF1* is diagnosed. Finally, when the temperature follows up, *MF2* is diagnosed. In the case of normal state to *SF1* at about 2,400 seconds, control signal rapidly increases due to the sudden pressure drop over the FPS. Until the fluctuation of the control signal stabilized and pressure responses, *MF3* is diagnosed before the *SF1*.

The fault diagnosis results APS at 60 A are presented in Fig. 3.10. In Fig. 3.10(a), degradation of air blower (*MF6*) and clogging (*MF4*) are clearly diagnosed. In the early stage of the transition from normal to 10% air mass flow meter signal offset failure (*MF5*), the degradation (*MF6*) and the clogging (*MF4*) are diagnosed in turn. This trend is similar to the fault case of *MF2* in FPS. Leakages at APS (*SF3*) are performed in two different spots; Between air

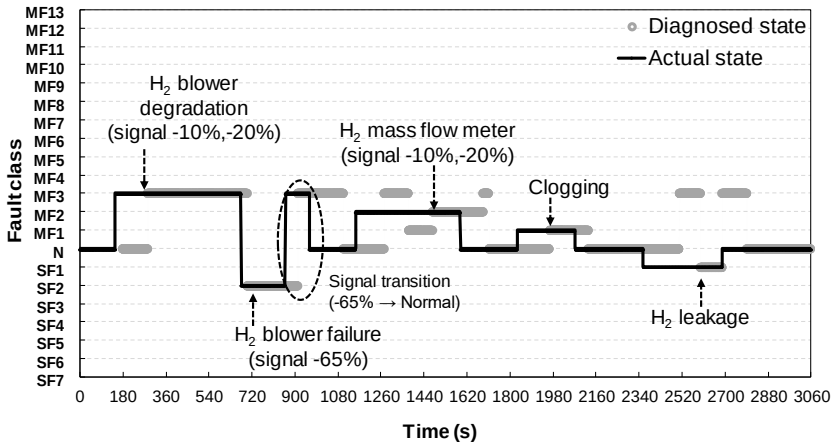

Figure 3.9 Fault diagnosis result in FPS at 80 A

blower and MFM, and between stack and humidifier. The latter case is clearly diagnosed, but the former case is diagnosed as air blower degradation. When the air leak occurs before the MFM, there are no other effects to the stack except for the case when required air flow rate is not sufficiently provided. In the situation, only air blower operates harder to compensate for the loss in the loop. Therefore, it is reasonable for the algorithm to diagnose the state as *MF6*.

In Fig. 3.10(b), severity of the MF5 is elevated to signal offset 20%. A similar trend is observed in the case of signal offset 10%. This phenomenon will be explained with the following 80 A case. After the MF5, control signal sent to the air blower is reduced from 0% to 55% gradually. In the process, *MF6* is firstly diagnosed. When the air blower could not supply the air flow that corresponds to the SR at 2.0, the algorithm diagnosed the state as *SF4*.

Fault diagnosis results in APS at current load 80 A are presented in Fig. 3.11. The diagnosis results are interpreted with the standardized residuals for significant fault neural network (Fig. 3.12(a)) and minor fault neural network (Fig. 3.12(b)). Miss-diagnosis at 240 seconds is due to the abrupt fault experiment from normal to blower degradation. Due to the abrupt incident, control signal and pressure fluctuated and miss-diagnosed for a short time. The miss-diagnosis at about 600 seconds in also due to the fluctuation. The phenomenon of miss-diagnosis at the early stage of *MF5* is due to the different

response time of control signal, pressure and temperature. With the *MF5*, the control signal firstly responses. Then, the pressure and the temperature is followed. With the responses, degradation and clogging are diagnosed in turn. Only after the temperature response is followed, the state is correctly diagnosed as flow meter fault. Response time different is also the reason for the miss-diagnosis at the early clogging (*MF4*). Over all, faults in APS are correctly diagnosed except for the leakage before the MFM.

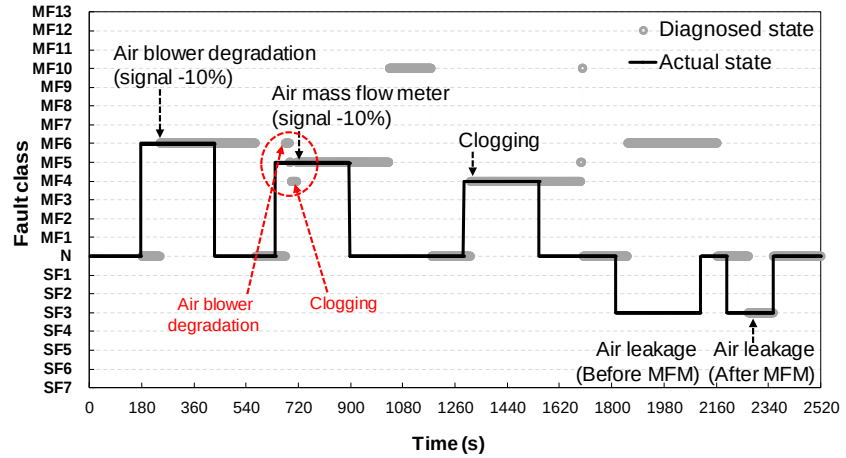

(a)

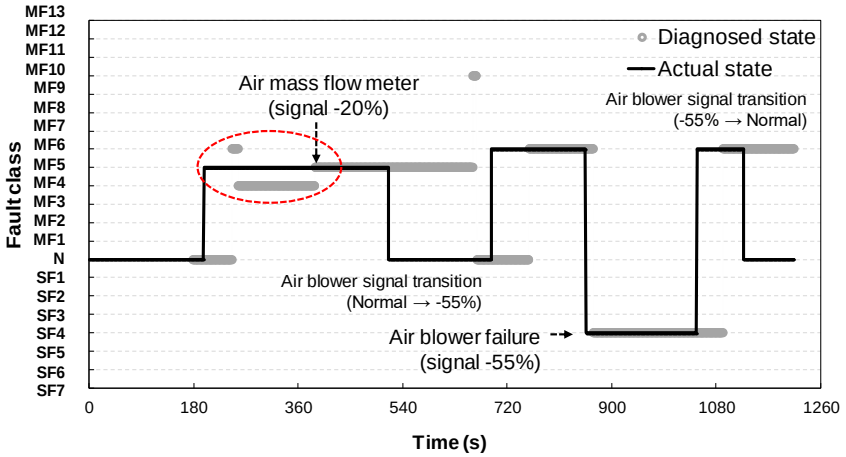

(b)

Figure 3.10 Fault diagnosis result in APS at 60 A

(a) First experiment (b) Second experiment

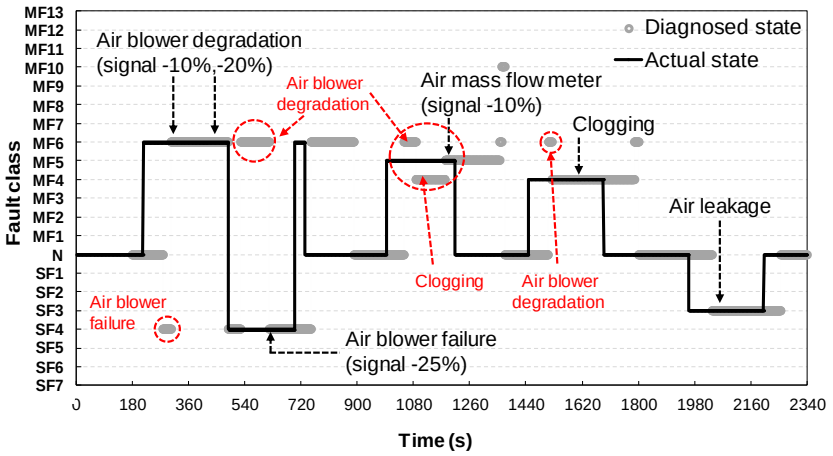

Figure 3.11 Fault diagnosis result in APS at 80 A

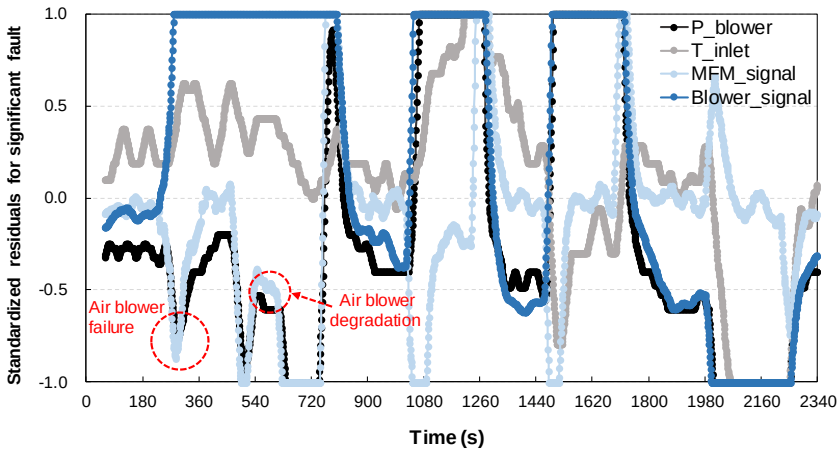

(a)

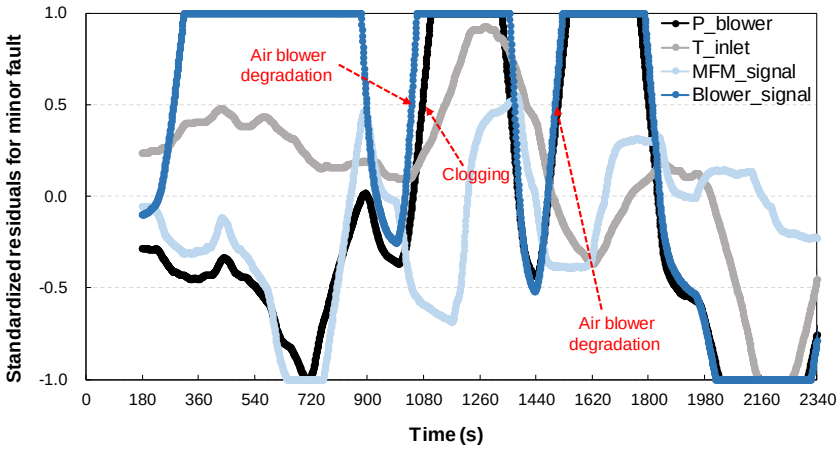

(b)

Figure 3.12 Standardized residuals for algorithm

(a) Residuals for NN2 (b) Residuals for NN3

The fault experiment and corresponding fault diagnosis are also performed in TMs. diagnosis results at current load 60 A is shown in Fig. 3.13. Degradation of water pump (*MF11*), degradation of radiator fan (*MF12*), clogging (*MF8*) and radiator fouling (*MF13*) are diagnosed in the Fig.3.13(a). Before the correct diagnosis of *MF13*, radiator fan degradation is miss-diagnosed. Since the radiator fouling is simulated by fan degradation and clogging in turn, this is natural result. In Fig. 3.13(b), stack outlet temperature sensor fault (*MF10*) and stack inlet temperature sensor fault (*MF9*) are simulated. Before the diagnosis of *MF9*, water pump degradation (*MF11*) and clogging (*MF8*) is diagnosed. As with the FPS and APS similarly, this is due to the different response time between the control signal, pressure and temperature. However, overall response time with TMS is much slower than the responses in FPS and APS. It seems that the thermal response takes more time likely to the case in FPS and APS. Therefore, diagnosis of a fault took more time in TMS than FPS and APS at current load 60 A.

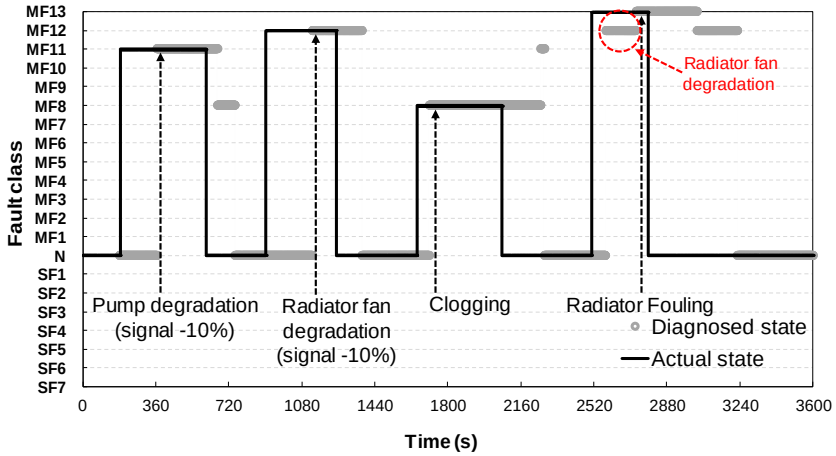

(a)

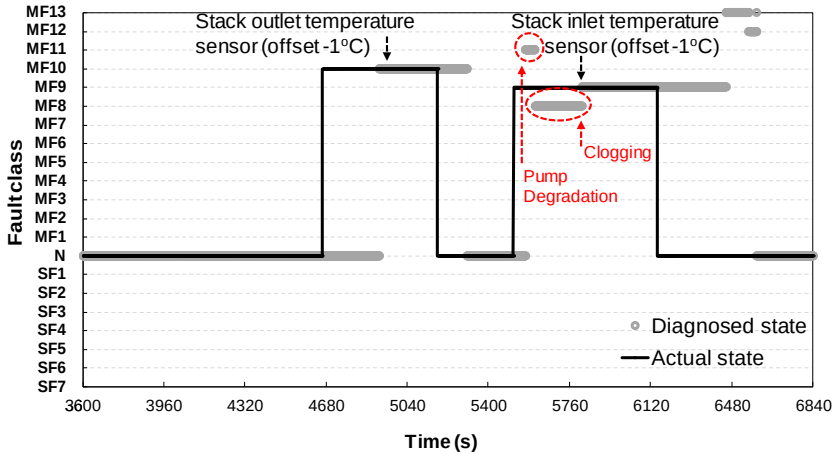

(b)

Figure 3.13 Fault diagnosis result in TMS at 60 A

(a) First hour experiment (b) Second hour experiment

The fault experiment and corresponding fault diagnosis of TMS are also performed at current load 80 A. The results are shown in Fig. 3.14. In Fig. 3.14(a), degradation of radiator fan (*MF12*) and the fan failure (*SF7*) are diagnosed during the first half hour. Then, degradation of the water pump (*MF11*), and the pump failure (*SF6*) are diagnosed for the next half hour. After the first hour, clogging (*MF8*), fouling (*MF13*), stack inlet temperature sensor fault (*MF9*) are diagnosed in turn (Fig. 3.13(b)). The similar miss-diagnosis patterns are shown in the early stage of *MF8* and *MF13* to the patterns shown with the 60 A miss-diagnosis cases. For *MF9*, the offset magnitude is adjusted. First, the offset is -0.5^{o}C. Under the situation, *MF9* is miss diagnosed as *MF8*. This is due to the increased coolant flow and pressure drop over the TMS, but not enough increment of FPS stack outlet temperature. The temperature at FPS did not increase above the threshold. The fault diagnosis result of coolant leakage (*SF12*) in TMS and humidifier fouling (*MF7*) are also clearly diagnosed. About 30 seconds after the signal change of reservoir level sensor, *SF12* is diagnosed. For *MF7*, the system is stopped to simulate the fault. The steady state of the *MF7* is clearly diagnosed with the increase of air blower control signal, increase of APS pressure and decrease of stack air inlet temperature.

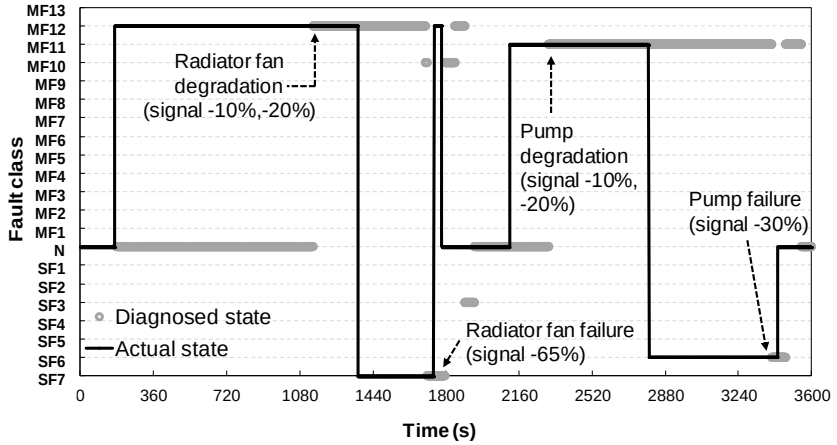

(a)

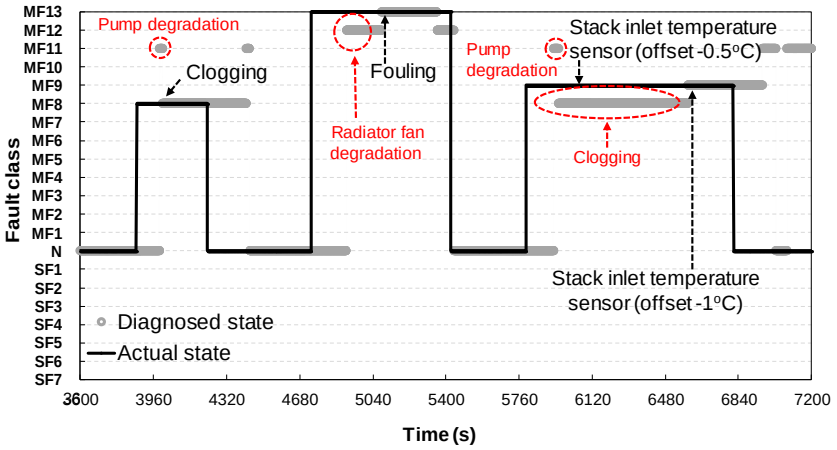

(b)

Figure 3.14 Fault diagnosis result in TMS at 80 A

(a) First hour experiment (b) Second hour experiment

The critical faults are simulated at current load of 60 A. Their diagnosis results are shown in Fig.3.15. The NN1, which detects the critical faults, diagnosed the all critical faults. Disabled state of air blower (*CF3*), hydrogen blower (*CF1*) and water pump (*CF4*) are diagnosed within the 10 seconds. Fuel depletion state (*CF2*) is diagnosed in 20 seconds. With the fault occurrences form *CF1* to *CF4*, the control/sensing signals reacted fast and big. Since the thermal response is very slow, *CF5* took time to be diagnosed.

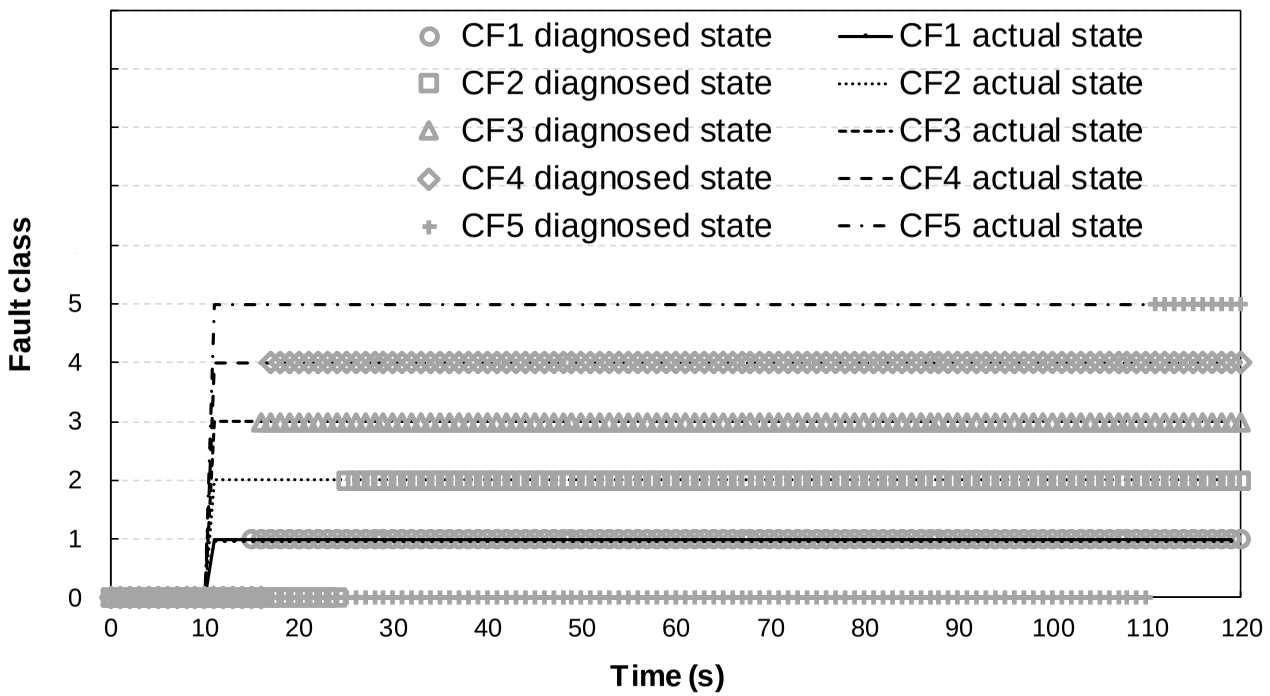

Figure 3.15 Critical fault diagnosis results in 60 A

3.5 Summary

In this chapter, a severity-based fault diagnostic method for PEMFC system is suggested. The core idea of the algorithm is to separately diagnose the faults depending on its severity. Fault scenarios are divided into three groups; critical faults, significant faults and minor faults. Three neural network classifiers diagnosed the state of the fuel cell in series, working as a severity-based fault diagnosis algorithm. With the algorithm, critical faults, significant fault, minor faults are successfully diagnosed in fuel providing system (FPS), air providing system (APS) and thermal management system (TMS) under the load condition of 60 A and 80 A. While responses and diagnosis of FPS and APS were fast, that of TMS was relatively slow.

Chapter 4. Current distribution prediction with neural network[1]

4.1 Introduction

This chapter presents the practical prediction method for PEMFC local current distribution. Unbalanced current distribution may induce local performance degradation and local hot spots, which may affect the fuel cell's durability. Therefore, it is important to operate the fuel cell under conditions that do not break the distribution balance. However, the current distribution is hard to predict with an analytic model because the fuel cell includes sophisticated multi-phase electrochemical reactions. Therefore, in commercial product development, a segmented fuel cell is used to observe current distribution inside the fuel cell. This chapter suggests a utilization method for the data collected in this process. Firstly, a neural network-based PEMFC local current prediction model is developed and validated. The effects of operating parameters on current distribution and its standard deviation are investigated with the model. Secondly, an idea of finding optimal operating conditions for

[1] The contents of chapter 4 are published in the International Journal of Hydrogen Energy on 17 June 2021. [74]

the uniform current distribution is suggested and evaluated. Additional neural network model is developed by positioning local current distribution as inputs and operating parameters as outputs. Feeding the uniform current distribution profile as input, an optimal operating condition is acquired. This operating condition is then evaluated with the current prediction neural network model developed in the first step. The contents of this chapter are published in the International Journal of Hydrogen Energy [74].

4.2 Experimental setup

4.2.1 Experimental apparatus

The experimental setup is presented in Fig. 4.1(a). Its schematic diagram is illustrated in Fig. 4.1(b). The test station for the fuel cell is typical. Air and hydrogen are provided from the gas tanks and are humidified through the bubbler type humidifier. The flowrates of the reactants are mass flow controlled (EL-FLOW, Bronkhorst, Netherlands). Electric pressure controllers (EL-PRESS, Bronkhorst, Netherlands) are located at the gas outlet. A segmented bipolar plate flow channel is on the anode which consists of 25 isolated segments. Each segment has 1 cm^2 active area. The areas are numbered from 1 to 25 following the anode flow direction, as shown in Fig. 4.2(a). Over all flow channel shape is serpentine with 5-pass and 4-turn channels, horizontally counter-flow and vertically parallel-flow.

The gold coated printed circuit board (PCB) collects the separate current flows and transfers to the hall effect sensors. The PCB is located between the end plate and the segmented channel. Twenty-five hall effect sensors (CY2-02B, Nana Engineering Co., Japan) are located between the PCB and electronic load (PLZ series, Kikusui, Japan). The hall effect sensors transmit local segment

current flow data to the data acquisition system (NI cDAQ-9178 with NI 9205 and NI9206, National Instruments, USA). The membrane electrode assembly (M815, Gore, USA) and gas diffusion layer (35BC, Sigracet, Germany) applied to in this research.

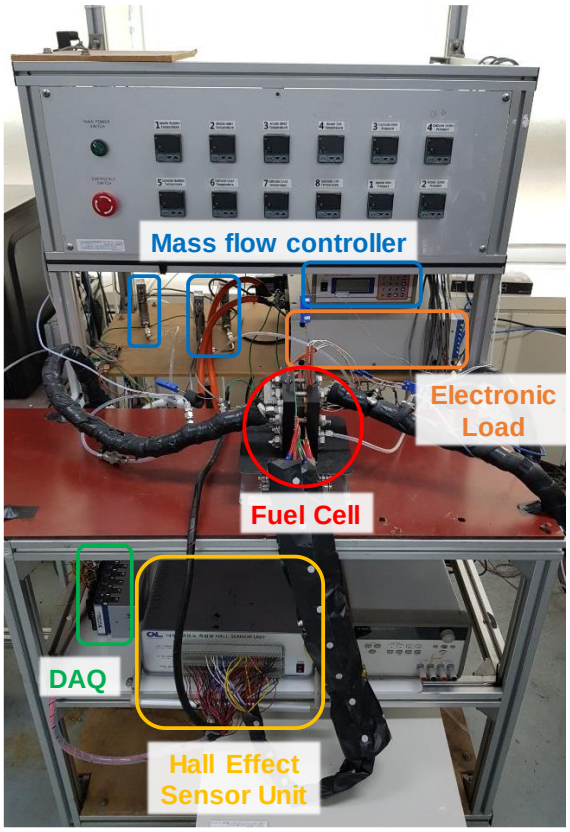

(a)

Figure 4.1 Experimental setup

(a) Fuel cell test station (b) Schematic diagram [74]

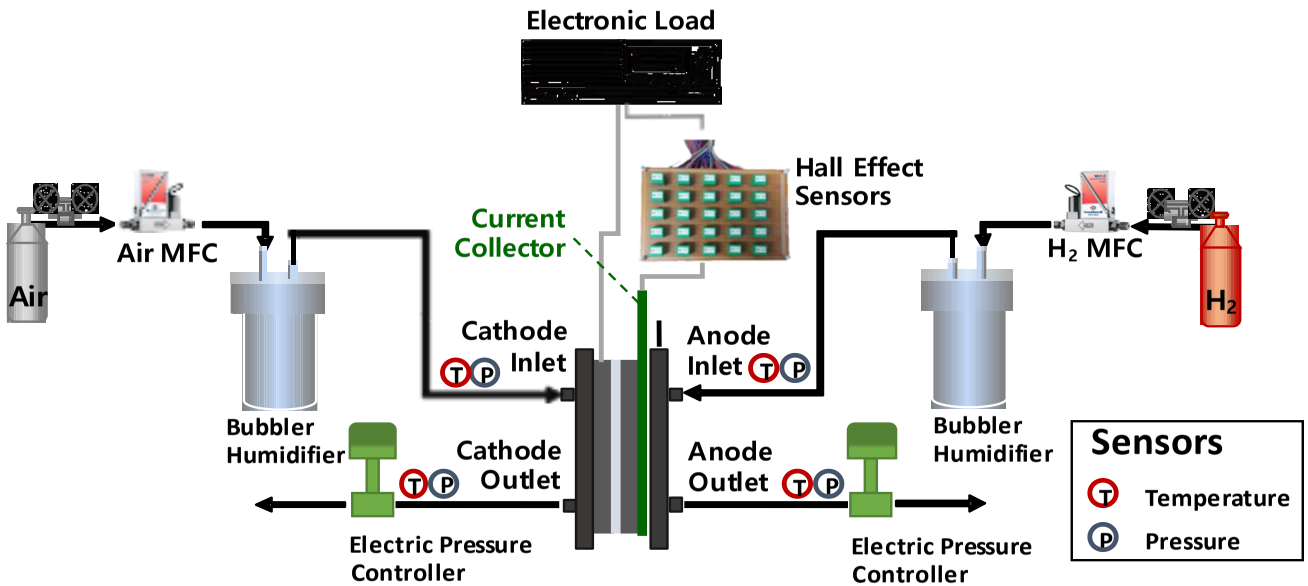

(b)

Figure 4.1 Experimental setup(a) Fuel cell test station (b) Schematic diagram (Continued) [74]

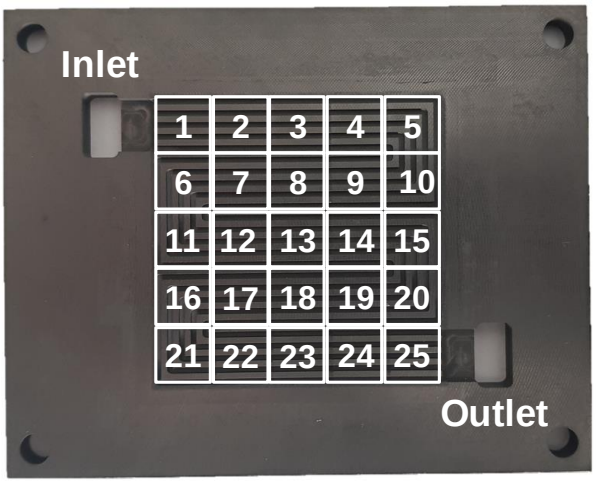

(a)

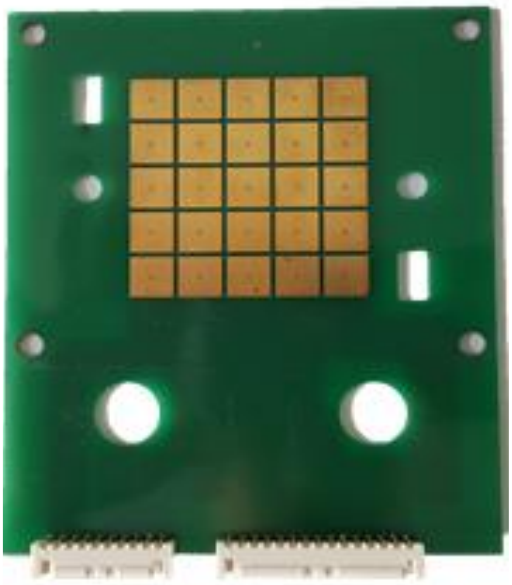

(b)

Figure 4.2 Segmented fuel cell

(a) Anode bipolar plate (b) printed circuit board [74]

4.2.2 Experimental conditions

Local current flow, representing local electro-chemical reaction, varies depending on multiple parameters such as temperature, pressure, gas concentration and relative humidity on both anode and cathode. The local current distribution profile data is collected under various operating conditions (Table 4.1.). Within the acceptable operating conditions (temperature (30~60^{o}C), dew point (30~60^{o}C), reactant stoichiometric ratio (1.2~3.5), and pressure (1~3 bar)), 161 different experimental condition are tested. Of these cases, current distribution profile of 125 cases are used for the model training and the rest cases (25 cases) are used for the model validation. The conditions for the train and validation are shown in the Table 4.1. The fuel cell is operated under galvanostatic mode with a current load 25A (1 A/cm^2 for each segment).

Table 4.1 Experimental conditions of train set and test set

Temperature (°C)	Dew Point(°C)		Stoichiometric Ratio(SR)		Pressure (bar)	
	H_2	Air	H_2	Air	TRAIN SET	TEST SET
30	30	30	1.2	1.2	1.0, 2.0, 3.0	
			1.5	2.0	1.0, 2.0, 3.0	1.5(6.1%), 2.5(5.2%)
			2.0	3.5	1.0, 2.0, 3.0	
40	40	40	1.2	1.2	1.0, 2.0, 3.0	
			1.5	2.0	1.0, 2.0, 3.0	1.5(6.2%), 2.5(6.3%)
			2.0	3.5	1.0, 2.0, 3.0	
50	50	50	1.2	1.2	1.0, 2.0, 3.0	
			1.5	2.0	1.0, 2.0, 3.0	1.5(4.1%), 2.5(4.0%)
			2.0	3.5	1.0, 2.0, 3.0	
60	30	30	1.2	1.2	1.0, 2.0, 3.0	
			1.2	1.5	1.0, 1.5, 2.0, 2.5, 3.0	
			1.2	2.0	1.0, 1.5, 2.0, 2.5, 3.0	
			1.5	1.5	1.0, 1.5, 2.0, 2.5, 3.0	
			1.5	2.0	1.0, 1.5, 2.0, 2.5, 3.0	
			1.5	2.5	1.0, 1.5, 2.0, 2.5, 3.0	
			1.8	2.0	1.0, 1.5, 2.0, 2.5, 3.0	
			1.8	2.5	1.0, 1.5, 2.0, 2.5, 3.0	
			2.0	3.5	1.0, 2.0, 3.0	
60	40	40	1.2	1.2	1.0, 2.0, 3.0	
			1.5	2.0	1.0, 2.0, 3.0	
			1.5	3.0		1.0(0.7%), 1.5(2.1%), 2.0(2.3%), 2.5(1.9%), 3.0(2.4%)
			2.0	3.5	1.0, 2.0, 3.0	

Table 4.1 Experimental conditions of train set and test set (Continued)

Temp. (°C)	Dew Point(°C)		Stoichiometric Ratio(SR)		Pressure (bar)	
	H_2	Air	H_2	Air	TRAIN SET	TEST SET
60	45	45	1.2	1.2		1.0(3.5%), 2.0(3.3%), 3.0(3.4%)
			1.5	2.0		1.0(3.7%), 2.0(3.0%), 3.0(3.4%)
			2.0	3.5		1.0(3.6%), 2.0(3.1%), 3.0(3.4%)
60	50	50	1.2	1.2	1.0, 2.0, 3.0	
			1.5	2.0	1.0, 2.0, 3.0	
			1.5	3.0		1.0(0.7%), 1.5(1.2%), 2.0(1.8%), 2.5(1.9%), 3.0(2.2%)
60	52	52	2.0	3.5		1.0(3.5%), 2.0(2.5%), 3.0(2.4%)
			1.2	1.2		1.0(3.7%), 2.0(2.8%), 3.0(2.5%)
			1.5	2.0		1.0(3.6%), 2.0(2.7%), 3.0(2.5%)
60	60	60	1.2	1.2	1.0, 2.0, 3.0	
			1.2	1.5	1.0, 1.5, 2.0, 2.5, 3.0	
			1.2	2.0	1.0, 1.5, 2.0, 2.5, 3.0	
			1.5	1.5	1.0, 1.5, 2.0, 2.5, 3.0	
			1.5	2.0	1.0, 2.0, 3.0	1.5(1.8%), 2.5(2.2%)
			1.5	2.5	1.0, 1.5, 2.0, 2.5, 3.0	
			1.8	2.0	1.0, 1.5, 2.0, 2.5, 3.0	
			1.8	2.5	1.0, 1.5, 2.0, 2.5, 3.0	

4.3 Model development

4.3.1. Neural network model

Proving its excellent pattern recognition performance, an artificial neural network has been applied to many engineering fields recently. In fuel cell engineering, the neural network has been mainly applied for fault detection and performance prediction. One good advantage in applying the neural network is the complexity of the fuel cell reaction. Fuel cell reaction is basically an electrochemical reaction, but is affected by heat transfer, mass transfer and two-phase flow in multi-scale. This complex reaction and multi-scale problem bring errors in the analytic model despite the significant computational time and power. The application of neural network technology can solve these problems. If there is enough data to be trained, complex physics and correlations can be replaced with the weight connections between the neurons. Replacement of equations to matrix makes the calculation remarkably fast and precise. In this sense, many researchers have developed PEMFC performance prediction models using neural networks. In this chapter, I have extended neural network application to the prediction of fuel cell current distribution.

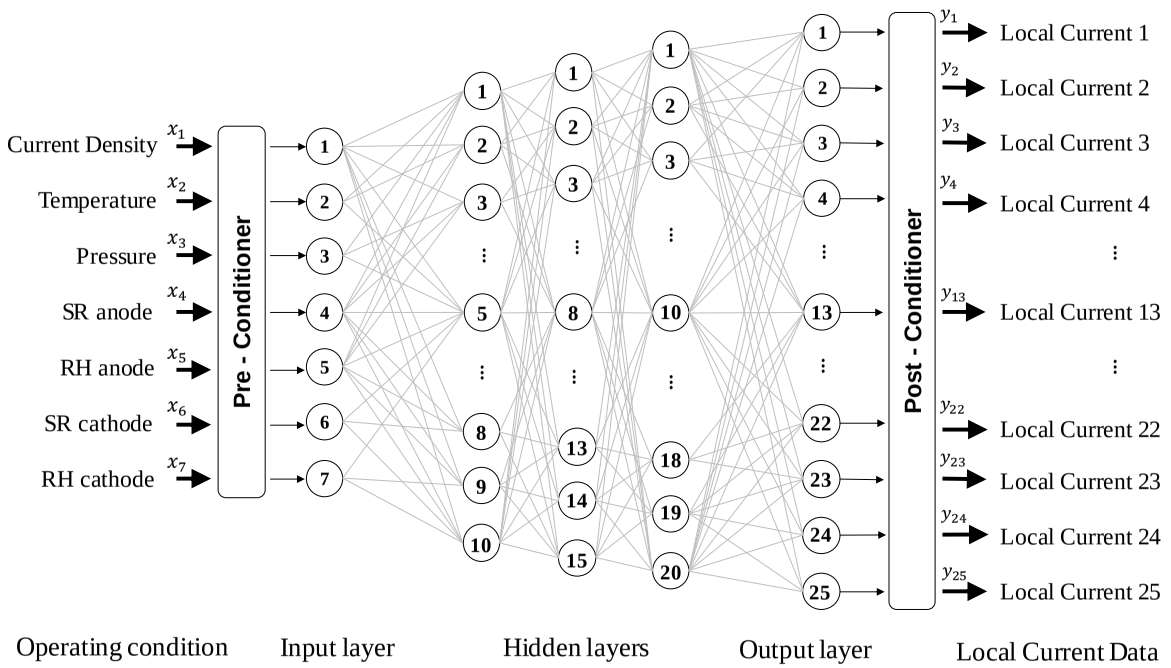

Figure 4.3 Current distribution prediction model [74]

The neural network model structure developed to predict the PEMFC current distribution is shown in Fig. 4.3. Each circle represents a single perceptron, which is a basic unit that constructs a neural network. The perceptron is a binary classier alone. When the perceptrons are connected, however, a 'layer' is formed. When the layer is connected in series, a neural network is developed and works as a powerful regressor or classifier. In this paper, the current distribution prediction model (Fig. 4.3) uses feedforward fully connected multi-layer perceptron (MLP) is applied.

The model consists of an input layer, hidden layers, and an output layer. Seven nodes in the input layer correspond to the operating parameters (current density, temperature, pressure, stoichiometric ratio (SR) of anode and cathode, and their relative humidity (RH)). Twenty-five output nodes in the outlet layer correspond to the locally measured current data. Each node matches the segmented area shown in Fig. 4.2(a). The hidden layers are composed of three layers with 10, 15, and 20 nodes each. There is no exact rule for the number of layers or the nodes in each layer. Nevertheless, many articles recommend a gradual increase or decrease in the number of nodes in each hidden layer. The number of layers was varied between two to six. I have not tried all the combinations with the variation in the number of nodes. However, three hidden layers showed good performance overall in the case of experimental data in this

chapter.

Aside from the structure of the neural network, pretreatment of the input and output data is very important. Pretreatment processes of inputs and outputs, each will be referred pre-conditioner and post-conditioner, are described in subsection 4.3.2. The details of the current prediction model development process will be explained in subsection 4.3.3. After then, the development process for an operating condition prediction model, which suggests operating conditions for the uniform current profile, will be introduced.

4.3.2. Data conditioning

Pre-conditioning

Neural network itself is originally a series of matrices, but the non-linearity is added between the matrixes. The values in the matrices (correlations between the inputs and outputs) are found automatically by renewing the values. Therefore, in developing the neural network, setting the proper input and output data in the right form is important. In normal, the given data to the neural network should be adjusted between the range of minus one to plus one for better performance. When the data is out of the range, the structure size of the neural network model should be increased to achieve similar performance

compared to the model trained with data in range. Considering this, operating parameters (inputs) are rescaled. Eliminating the physical dimension effect, each parameter is rescaled in the range of zero to plus one following the equations below (Eq. (4.1) to Eq. (4.7)). The code that pre-conditions the input data will be referred to as a scaling filter in the thesis

$$i_{load} = \frac{I_{load}}{Area} \quad (4.1)$$

$$t = \frac{\mathrm{T}}{100} \quad (4.2)$$

$$p = \frac{\mathrm{P}}{100} \quad (4.3)$$

$$sr_{anode} = \frac{SR_{anode}}{10} \quad (4.4)$$

$$rh_{anode} = \frac{RH_{anode}}{100} \quad (4.5)$$

$$sr_{cathode} = \frac{SR_{cathode}}{10} \quad (4.6)$$

$$rh_{cathode} = \frac{RH_{cathode}}{100} \quad (4.7)$$

Post-conditioning

Similarly, with the input data, local current data (output data) needs to be

preprocessed. Since the process will help the outcomes of the neural network transformed back to their original form, the procedure will be referred as a post-conditioner. The post-conditioner consists of two functions. The first one adjusts the measured current data from the hall sensors. It eliminates the small difference (less than 1%) between the sum of the current flows at each segment and the loaded current flow to the fuel cell. The current flow value at each segment is then multiplied with the relative ratio between the actual sum (loaded current) and the sum of the current flows from the hall sensors. Plus, the current flow is divided with the active area, transforming into current density (since the segment's active area is 1 cm^2, there is no difference in the value). The explained process above is shown in Eq. (4.8), and referred as the current sum filter.

$$i_k = \frac{I_k}{\sum I_k} \times \frac{I_{Load}}{Area} \tag{4.8}$$

The second function rescales the adjusted current density data from the first function in the form of residuals. If this process is skipped, outputs will be within the specific current range that matches the input current load value. To isolate the dependence on the input current load, output current data is nondimensionalized. The current data is transformed into residuals and divided with the loaded current density as shown in Eq. (4.9). The code that proceeds

the Eq. (4.9) will be referred to as the residual filter.

$$r_k = (i_k - i_{Load}) \ / \ i_{Load} \tag{4.9}$$

4.3.3. Model training

Current distribution prediction model

Figure 4.4 explains the development process for the current distribution prediction model shown in Fig. 4.3. The very first step for neural network modeling is selecting a dataset. The list of used training data and test data is shown in Table 4.1.

The second step is proper conditioning of the input and output training data. The PEMFC operating condition, as an input, is preprocessed with the scaling filter. The local current data, as an output, is preprocessed with the current sum filter and the residual filter. Preprocessed input and output data are then used to train the neural network (Fig. 4.3). For the training, a multi-layer perceptron regression algorithm provided by the Scikit-learn software is used. This 'Scikit-learn' is a Python programming language-based machine learning library. This research suggests the methodology for the PEMFC current distribution modeling, not the artificial intelligence modeling technique. Therefore, this study utilized the open source library. Any commercial or self-

developed neural network can be used following the method suggested in this chapter. In the process of neural network model training, hyper-parameters should be properly adjusted to achieve higher model performance. These hyper-parameters are initial values that should be given for the training. Therefore, hyper-parameter values are grid-searched and optimized with the combination test.

As a third step, the developed model is evaluated. Operating conditions listed as test set in the Table 4.1. are preprocessed with the pre-conditioner and put into the trained neural network model. the outputs will be normalized local current residual data. The outputs are then post-processed with the post-conditioner. As final outcome, 25 local current data is acquired. Since the outcomes are predicted values, the outcomes are finally compared with the measured local current data as shown in the Fig. 4.4.

Uniform current prediction model

In this chapter, a novel method for finding optimal operating conditions which can achieve uniform current distribution is proposed. The model that will be developed using this method will be referred to as uniform current prediction model. The overall process of the development and evaluation is depicted in Fig. 4.5. The core idea of the development is to switch the inputs and outputs

of the current distribution model. Then, the current distribution profile will be input and operating condition will be the output. Since the inputs and outputs are flipped, the structure of the neural network should also be flipped. To put it simply, everything else stays the same, but the direction of the information is reversed. While then, pre-conditioning and post-conditioning process are also reversed, renamed as ‘reverse pre-conditioner’ and ‘reverse post-conditioner’. The details are well described in Fig. 4.5. In the process of uniform current prediction model, hyper-parameter values remain the same with the values from the current distribution prediction model.

After the development, the uniform current distribution profile is put into the model. Current load of 1 A is equally given to the 25 inputs, as shown in Fig. 4.5. As a result, a specific operating condition is acquired. If the reverse strategy is valid, the current distribution should turn out uniform when this operating condition is put into the current distribution prediction model. Here, the current distribution prediction model is used as a validation tool. After the validation, the output local current data is compared to the uniform current distribution profile.

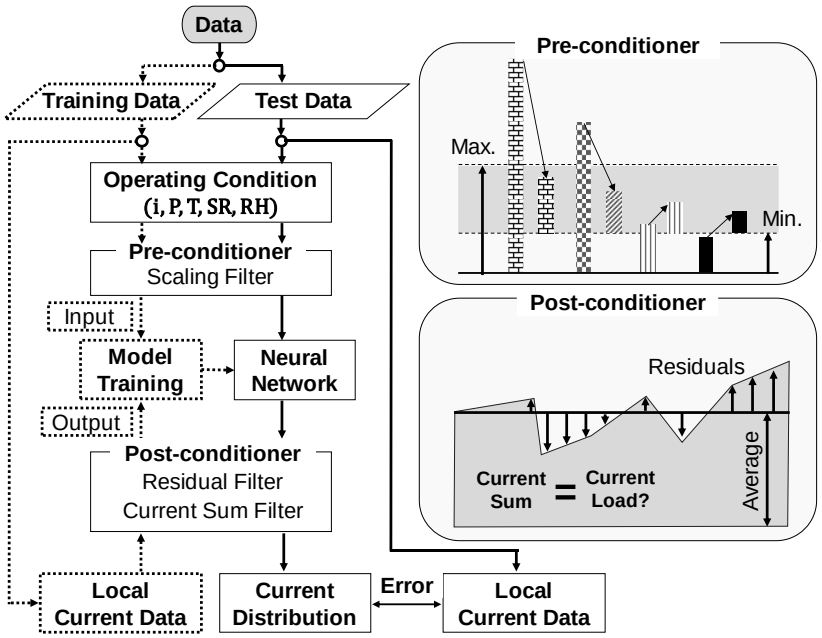

Figure 4.4 Training procedure for current distribution prediction model [74]

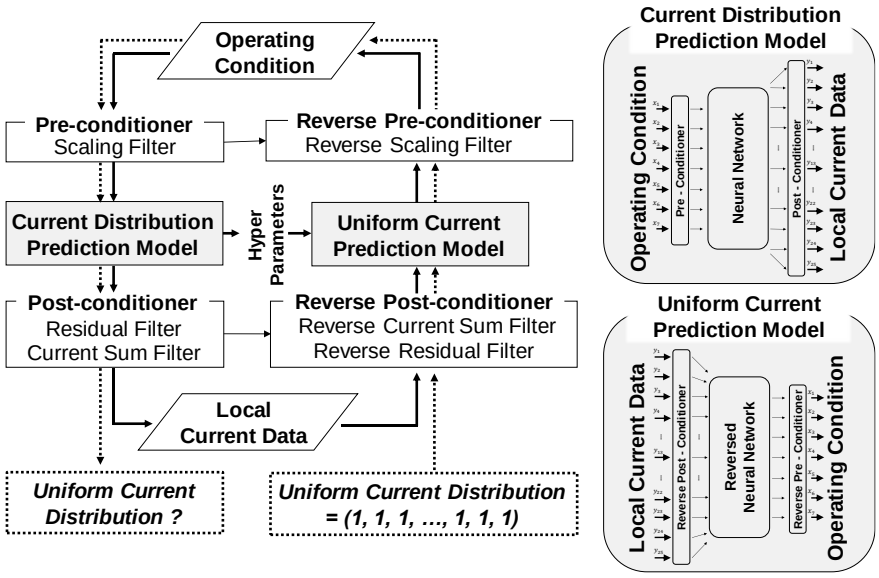

Figure 4.5 Training flow chart for uniform current prediction model [74]

4.4 Results and Discussion

4.4.1 Model accuracy

In the previous subsection, the current distribution model development and the evaluation process are explained. As an example, the comparison result of the model and experimental local current profile data is shown in Fig. 6. The exemplary case is the current distribution profile under pressure at 2 bar, the temperature at 60^{o}C, SR of anode and cathode at 1.5 and 2.0, respectively, and humidity of both anode and cathode at 40^{o}C dew point. The absolute errors between the prediction and experimental data are shown next to the test cases in Table 1. The error values are red, orange and green marked depending on their error range. If the error is bigger than 4.0%, it is marked in red. If the error is smaller than 2.0%, it is marked in green. In between, it is marked in orange. The overall absolute average is 3.0%. An interesting result is that the test cases can be grouped clearly. Due to the nature of machine learning techniques, the test results show small errors if similar data is trained. For example, the very first six test cases show larger errors compared to the rest test cases. Here, it can be concluded that more data is in need if we are to develop a more accurate model.

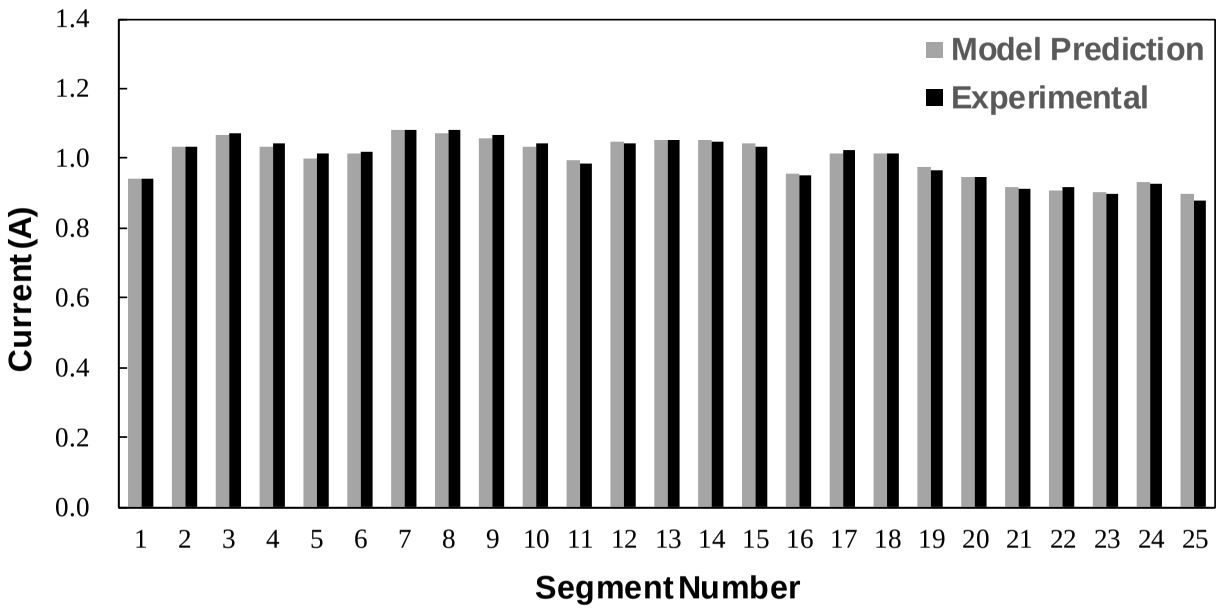

Figure 4.6 Comparison of local current distribution predicted by current distribution prediction model and experimental data (Operating condition; pressure (2 bar), temperature (60°C), anode SR (1.5), cathode SR (2.0), both anode and cathode humidity (dew point temperature at 40°C)) [74]

The application goal of this suggested neural network method is to bridge the gap between the simulation model and experimental data. However, note that the experimented local current data might not exactly match the electrochemical reaction. Near the segmented line between the section, electron transportation may not match the membrane proton transportation [75].

4.4.2 Effects of parameters on current distribution

Using the developed prediction model, the effects of operating conditions on the current distribution profile are tested. As a reference, pressure at 1 bar, 60^{o}C temperature, cathode SR at 2.0, anode SR at 1.5, cathode RH at 80% and anode RH at 80% is set under current load at 1 A/cm^2. Based on this reference, each operating parameters are varied. Preceding studies [39,40,60,61] pointed out that the cathode condition effect is much more dominant than that of the anode. Therefore, the current distribution trends with temperature, pressure, cathode SR, cathode RH variations are tested and suggested in Fig. 4.7.

The x-axis segmentation section number in Fig. 4.7 is the location shown in Fig. 4.2(a). Operating parameter value and current flow rate are each shown in the y-axis and z-axis. Overall, local peaks are observed in sections 3, 8, 13, 23 and 28, which are the middle sections of the membrane. These peaks are

combined results of the contact resistance [60,61,77], the flow field configuration [76,77], and the heat dissipation at the outer cell boundaries [47,61]. Another overall point is that the lower current flows are observed in the outlet stream. This characteristic is found commonly found in the PEMFCs [39,57,72,78-81]. It results from the low reactant concentration and liquid water flooding [39,40,61].

Effect of temperature on the current distribution is presented in Fig. 4.7(a). With the temperature elevation, current distribution turns more uniform. Low current flow at the outlet region of the channel at low temperature results from flooding [65]. On the other hand, the inlet region current flow should be increased to compensate for the current loss in the outlet region. When the operating temperature is elevated, water vapor capacity in the channel increases, which alleviates the flooding leading to the reduced non-uniformity [77]. Effect of operating pressure on the current distribution is shown in Fig. 4.7(b). The portion of inlet region current flow increases with temperature elevation, but its effect is not as critical as the operating temperature. Next, the cathode SR (Stoichiometric Ratio) effect on the current distribution is shown in Fig. 4.7(c). The cathode SR is one of the most important factor that affects the performance of the fuel cell. One of the main performance degradation results from the low concentration of oxygen in the outlet region. Relatively low current flow at the

outlet region in Fig. 4.7 is due to this low concentration in the outlet region. With cathode SR increment, peak current shift from inlet to the middle region. A similar current distribution result are reported in the preceding studies [41,60,61].

The current distribution variation with cathode relative humidity (RH) change is shown in Fig. 4.7(d). In the high RH condition, local current flow decreases along the flow channel.

The current distribution variation with cathode relative humidity (RH) change is shown in Fig. 4.7(d). In the high RH condition, local current flow decreases along the flow channel. As the RH decreases, however, the current peak is made in the middle region due to the decreased local current flow in the inlet region. This trend results from the membrane dry-out in the inlet region with decreased RH [35,65].

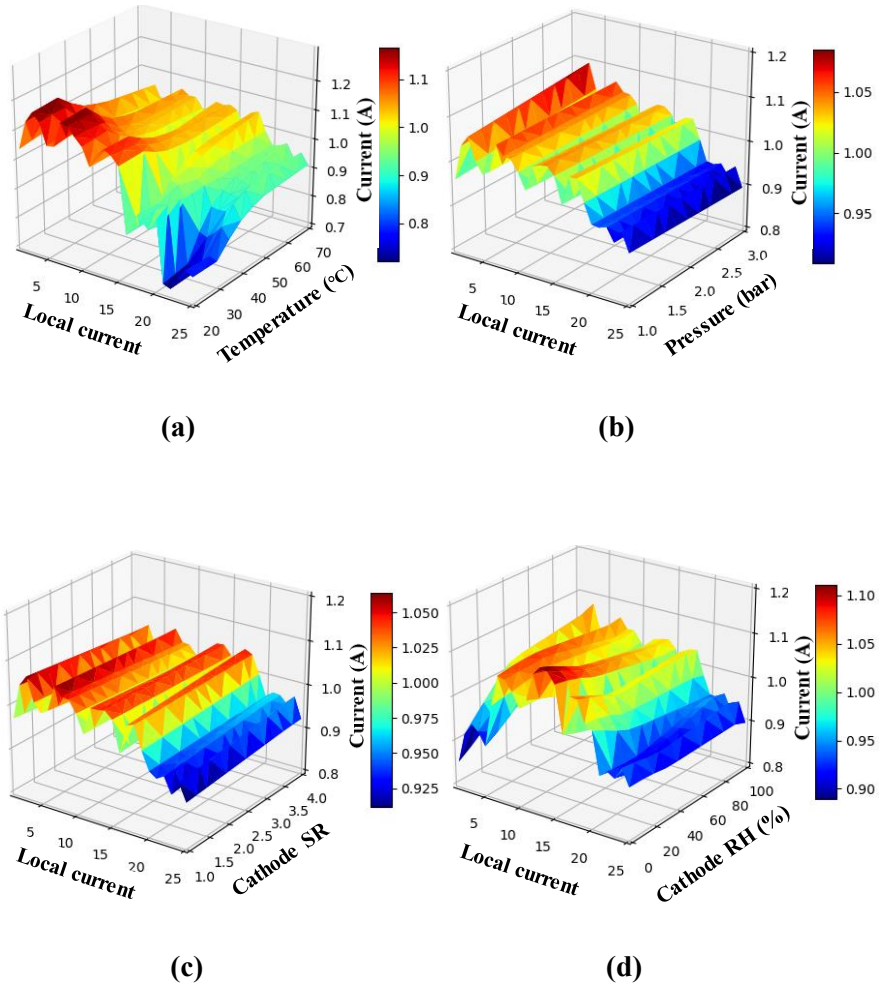

(a) **(b)**

(c) **(d)**

Figure 4.7 Effects of operating parameters on local currents

(a) Temperature (b) Pressure (c) Cathode SR (d) Cathode RH [74]

4.4.3. Effects of parameters on standard deviations

The operating parameter effects are presented in Fig. 4.8(a) and Fig. 4.8(b). To evaluate the effect, current distribution uniformity is expressed in the form of standard deviation. Fig. 4.8(a) shows the effects of temperature and pressure on the local current flow uniformity. With the temperature elevation, the non-uniformity of the current distribution decreases. As explained, this is due to the alleviation of the flooding in the outlet region with high vapor water capacity. With the pressure elevation, the current distribution is uniformed in the high-temperature condition while non-uniformed in the low-temperature condition. In low-temperature conditions, the vapor water saturation starts closer to the inlet region [61]. In other words, the flooding starts earlier with the temperature decrement, leading to the non-uniformity with the underperformed current flow in the outlet region. Overall, high-temperature with high-pressurized operating conditions seem to make the fuel cell current distribution uniform.

In Fig. 4.8(b), the effects of SR and RH on the uniformity of the current distribution are suggested. With the elevation of RH, the standard deviation tends to decrease until a certain level (70%). After then, the standard deviation increases. As shown in Fig. 4.7(d), excessively low or high RH induces non-uniformity. Therefore, there is an optimal humidification condition for the fuel cell [32]. It seems that the optimal RH for the uniform current distribution is

formed around 70% in this research. Under the RH lower than ca. 70%, standard deviation tends to decrease with the increasing cathode SR. Overall, it seems that RH around 70% with increased SR improves the current uniformity.

4.4.4. Uniform current distribution

From the uniform current prediction model shown in Fig. 4.5, the operating condition for uniform current distribution is acquired. This operating condition implies pressure at 2.3 bar, the temperature at 65.1^{o}C, SR of anode and cathode at 1.62 and 2.93, respectively, and RH of anode and cathode at 68.9% and 71.8%, respectively. Considering the standard deviation results shown in Fig. 4.8, high enough temperature (65.1^{o}C), elevated pressure (2.3 bar), moderate cathode RH (71.8%), and high enough cathode SR (2.93) conditions seem reasonable enough. This allegedly optimal operating condition for the uniform current distribution is then put into the current distribution model for evaluation. The corresponding current distribution profile is acquired, as shown in Fig. 4.9. The profile is not exactly uniform as expected. The absence of the local current experimental data may have made this result since most distributions showed decreasing current flow along with the segmented number. Nevertheless, the current standard deviation with the acquired operating condition showed 0.039 A, which is a smaller value than the current

deviation results shown in Fig. 4.8. Considering the reasonability of the acquired operating condition investigated with Fig. 4.8 and the small current deviation, it seems that this reversed neural network approach is valid.

The optimal operating conditions for the uniform current distribution can also be found using optimization techniques. Perhaps, it may be a more appropriate approach than the one suggested above. However, when the right amount of local current distribution data is prepared, the suggested approach is faster and efficient. It only costs switching inputs and outputs.

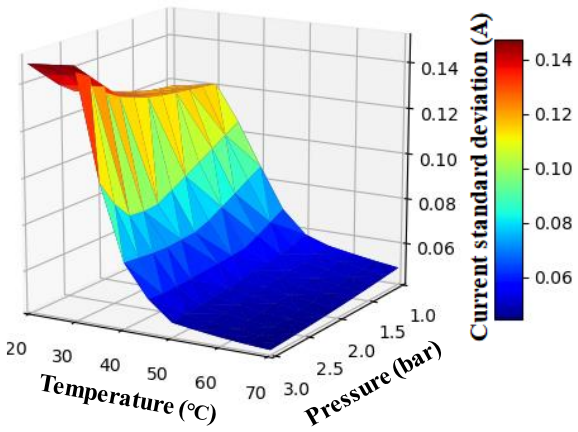

(a)

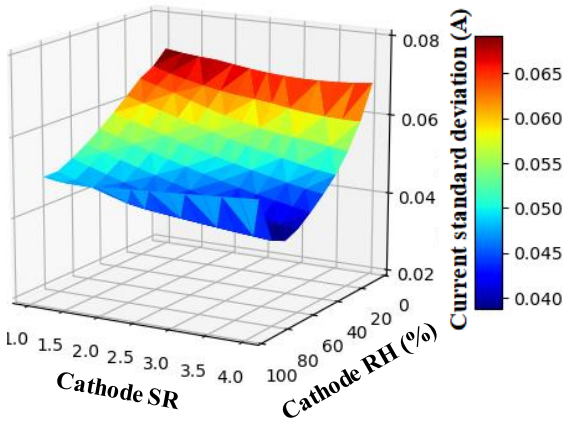

(b)

Figure 4.8 Effects of operating parameters on the standard deviation of local current (a) Temperature & Pressure (b) Cathode SR & cathode RH [74]

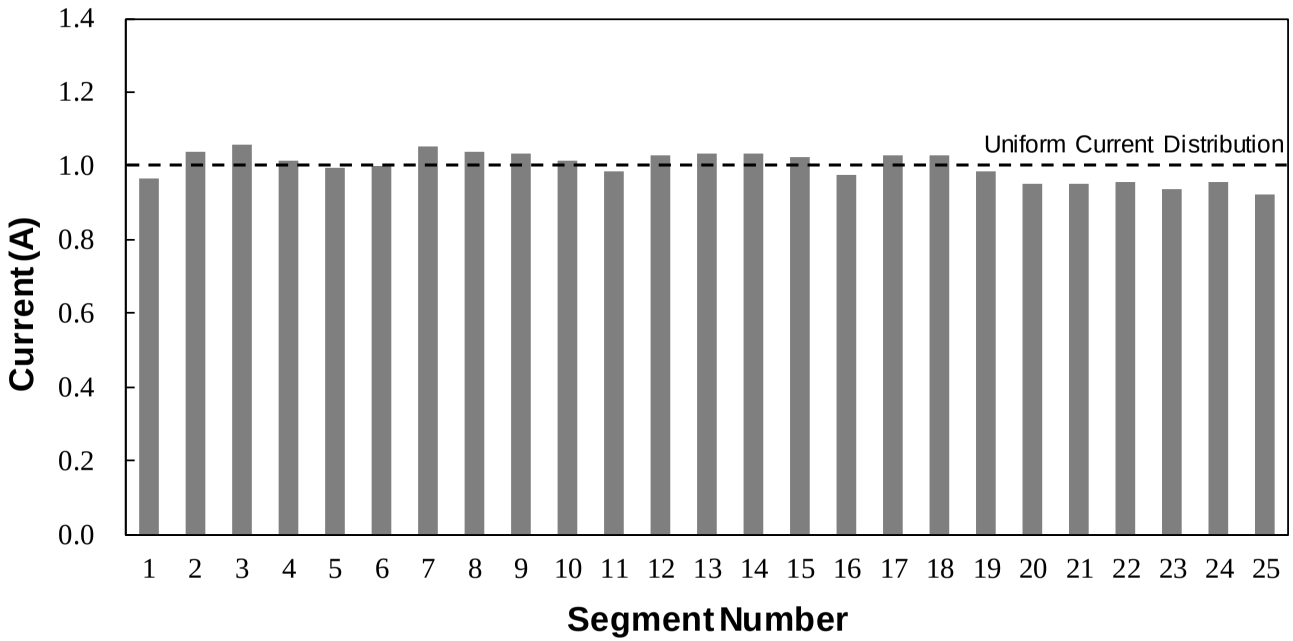

Figure 4.9 Local current distribution acquired from uniform current prediction model [74]

4.5. Summary

In this chapter, a new PEMFC local current distribution prediction method is suggested. The suggested method has advantages in the fast development process and high enough accuracy using a neural network algorithm. The developed neural network-based model predicted the current distribution profile within a 3.0% error. The effects of operating condition parameters (pressure, temperature, cathode stoichiometric ratio, cathode relative humidity) on local current distribution and uniformity are analyzed with the current distribution prediction model.

Switching the input and output data used for the current distribution prediction model, another neural network model is developed. This new model, the uniform current prediction model, suggests the operating condition that can achieve uniform current distribution. The suggested operating condition suits the investigated current distribution results with the current distribution prediction model. As a result, the current distribution uniformity is achieved with the standard deviation of 0.039 A under the current density of 1 A/cm^2.

Chapter 5. Current distribution prediction under degradation and fault

5.1 Introduction

Most of the PEMFCs are operated under specific conditions considering their performance and durability. Despite many efforts, however, the performance of PEMFC decreases after a long-time operation [82,83]. With the degradation, the current distribution inside the PEMFC changes. Therefore, local hot spots or the reactant concentration distribution also change with the degradation. In this context, the evolution of PEMFC local current distribution is investigated under degradation. The degradation is simulated by applying an accelerated stress test (AST) to a segmented fuel cell. Considering that the overall concept of the thesis is related to the fault, the current distribution change under faulty conditions is also investigated.

Most importantly, in this chapter, a prediction method for local current distribution under degradation and fault is suggested. The method is an extension of the method suggested in chapter 4, but capable of considering the time effect and various current densities. The prediction model is developed and validated using the collected data from the experiments.

5.2 Accelerated stress test

One of the PEMFC's weaknesses is its durability. United States department of energy (DOE) suggests 8,000 hours of operating time with less than 10% loss of performance as an ultimate durability target. Based on the on-road data collected from 230 fuel cell electric vehicles (FCEVs), however, most of the stack showed a performance decrease between 1,500 and 2,000 hours [84]. Likewise, the performance degradation of PEMFC is inevitable in the current state.

There are many reasons for the degradation of the fuel cell. Representative phenomena of fuel cell electric vehicle (FCEV) stack degradation are as follows [85]; degradation of the catalyst layer due to the carbon corrosion, loss of catalyst active area due to the platinum dissolution and sintering, loss of catalyst active are due to the adsorption of contaminants, and mechanical degradation due to the thermal and humidity stresses. Among these phenomena, carbon support corrosion of the catalyst layer is actively researched both industrially and academically.

PEMFC carbon corrosion is often explained with below equation [86];

$$C + 2H_2O = CO_2 + 4H^+ + e^-, \qquad E_0 = 0.207\ V_{RHE} \tag{5.1}$$

Since the PEMFC is operated above the given voltage (0.207 V), carbon corrosion can proceed in the catalyst layer. The detailed process about the carbon corrosion in PEMFC can be found in the following papers; [85,87-89]. This process, however, proceeds very slow in a natural state. Therefore, an accelerated stress test (AST) is applied in many studies.

There are mainly two AST methods for simulating carbon corrosion in PEMFC [85]; The first is applying a start-up or shut-down cycle to the PEMFC. This process is based on the explanations that local fuel starvation on the anode induces the oxygen crossover, which brings the overpotential to the fuel cell. The second is applying overpotential higher than the open-circuit voltage (OCV). This is also related to fuel starvation, but different mechanisms; non-uniform fuel distribution at sudden high current loads, liquid water accumulation, localized blockage due to the ice formation [85].

Jung et al. [90] followed the second method by applying 1.3 V, 1.4 V and 1.5 V to the fuel cell. Lee et al. [91] applied 1.5 V on the fuel cell to simulate the carbon corrosion. Spernjak et al. [92] applied 1.3 V on the fuel cell to investigate the influence of the microporous layer on carbon corrosion. Lin et al. [50] applied a maximum overvoltage of 2.0 V to investigate the anode carbon corrosion effect. This study also follows the second AST method by applying 1.4 V to the fuel cell. However, the AST method is not the point in

this chapter.

This chapter aims to validate the effectiveness of the suggested current distribution prediction method under degradation and faults. Thus, the AST method is not the point in this chapter, but the distribution changes itself with the AST is the focus of this chapter.

5.3 Experimental setup

5.3.1 Experimental apparatus

The experimental setup is shown in Fig. 5. 1(a), and its schematic diagram is illustrated in Fig. 5.1(b) [93]. Basic compositions are similar to the experimental setup in chapter 4. In Fig. 5.1(a), A segmented fuel cell with a printed circuit board is used. Twenty-five hall effect sensors (CY2-02B, Nana Engineering Co., Japan) are used to measure local current flows. The current flow data is collected with the acquisition system (NI cDAQ-9178 with NI 9205 and NI9206, National Instruments, USA). Power supply (E3649A, Agilent) is used for applying overvoltage to the MEA. Potentiostat module (WPG100HP, Wonik) is placed to observe electrochemical characteristics of PEMFC. For the temperature control, a temperature bath circulator is used to supply deionized coolant to the fuel cell.

In Fig. 5.1(b), dry air and hydrogen from gas tanks are supplied to the segmented cell with mass flow controllers (EL-FLOW, Bronkhorst, Netherlands). Between the mass flow controller and the segmented cell, a bubbler humidifier is located for reactant humidification. Electronic load (PLZ series, Kikusui, Japan) is used to control the current or voltage of the fuel cell.

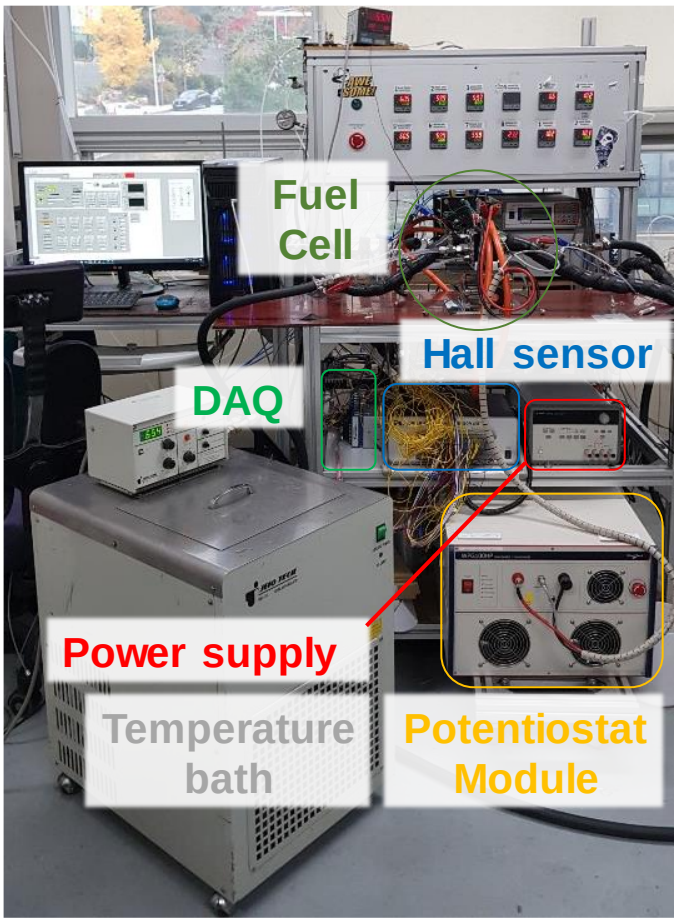

(a)

Figure 5.1 Experimental setup

(a) Fuel cell teset station (b) Schematic diagram [93]

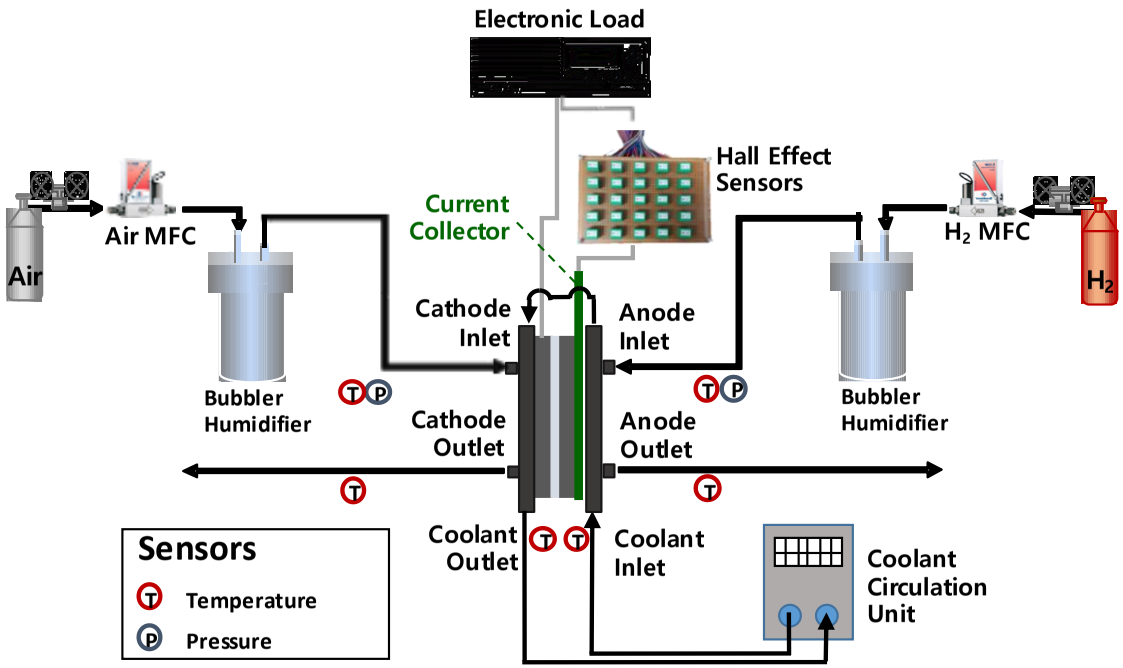

(b)

Figure 5.1 Experimental setup (a) Fuel cell test station (b) Schematic diagram (Continued) [93]

An anode bipolar plate of the segmented fuel cell is shown in Fig. 5.2. Looking at the front side (Fig. 5.2(a)), the channel is divided into 25 isolated segments. As a typical serpentine flow field with 5-pass and 4-turn channels, reactants are counter-flow at each horizontal line but parallel with the vertical direction. Each segment has a 1 cm^2 active area. The 25 segments are grouped into five areas, from the inlet to the outlet (A to E). The gold coated printed circuit board current collector is placed at the back of the anode bipolar plate to separately transfer currents from local spots to the hall effect sensors. The contact area of the bipolar plate and the printed circuit board is shown in Fig. 5.2(b). The membrane electrolyte assembly (VFM, CNL, South Korea) used in this chapter has an active area of 25 cm^2, as well as the gas diffusion layer (39BB, Sigracet, Germany) applied to both anode and cathode.

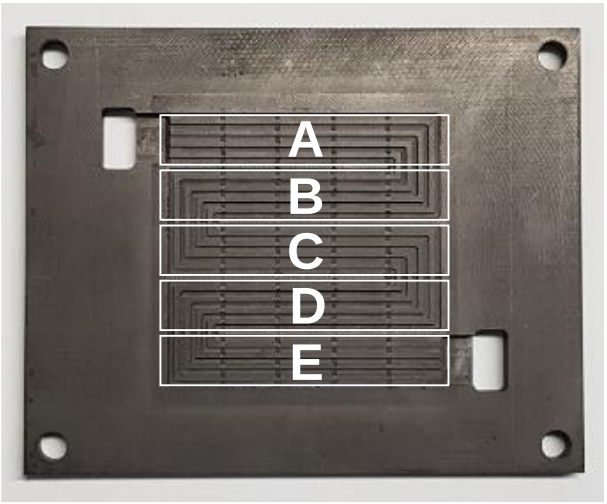

(a)

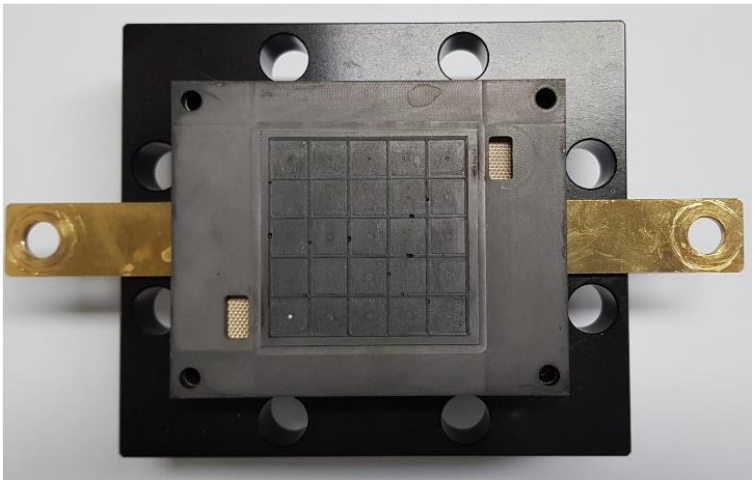

(b)

Figure 5.2 Anode bipolar plate (a) Front side (b) Back side

5.3.2 Experimental conditions

To observe the evolution of local current distribution under degradation and fault, reference operating conditions should be fixed. The reference operating conditions are as follows; temperature at 65°C, non-pressurized, anode SR at 1.5, cathode SR at 2.0 and relative humidity of 80% at both cathode and anode.

Experimental degradation and fault conditions are given in Table 5.1. For PEMFC degradation simulation, an accelerated stress test (AST) technique with 1.4 V overvoltage is application is performed. From the initial state (beginning of life), the AST proceeded for 8 hours. Every hour, AST is stopped to measure the PEMFC performance. Also, current distribution data under the air supply fault, humidification fault and temperature fault are collected every couple hours during the AST. The air supply fault is simulated by varying the cathode SR from 1.6 to 2.4. The humidification fault is simulated by reducing the cathode dew point to 46°C and 54°C, which corresponds to the relative humidity of 40% and 60%. The temperature fault is simulated by elevating the operating temperature from 65°C to 70°C. The fault data is collected under the current loads at 10A, 20A and 30A.

The overall experimental procedure is briefly presented in Fig. 5.3. First, the performance of the fuel cell is measured with its current distribution. Before

Table 5.1 Experimental degradation and fault conditions

AST (hour)	Operating Temperature (ºC)	Dew point (ºC)		Stoichiometric Ratio (SR)	
		H_2	Air	H_2	Air
0 (Beginning of Life)	65	60	60	1.5	2.0
	65	60	60	1.5	1.6, 1.8, 2.2, 2.4
	65	60	46, 54	1.5	2.0
	70	60	60	1.5	2.0
1	65	60	60	1.5	2.0
2	65	60	60	1.5	2.0
	65	60	60	1.5	1.6, 1.8, 2.2, 2.4
	65	60	46, 54	1.5	2.0
	70	60	60	1.5	2.0
3	65	60	60	1.5	2.0
4	65	60	60	1.5	2.0
	65	60	60	1.5	1.6, 1.8, 2.2, 2.4
	65	60	46, 54	1.5	2.0
	70	60	60	1.5	2.0
5	65	60	60	1.5	2.0
6	65	60	60	1.5	2.0
	65	60	60	1.5	1.6, 1.8, 2.2, 2.4
	65	60	46, 54	1.5	2.0
	70	60	60	1.5	2.0
7	65	60	60	1.5	2.0
8 (End of Life)	65	60	60	1.5	2.0
	65	60	60	1.5	1.6, 1.8, 2.2, 2.4
	65	60	46, 54	1.5	2.0
	70	60	60	1.5	2.0

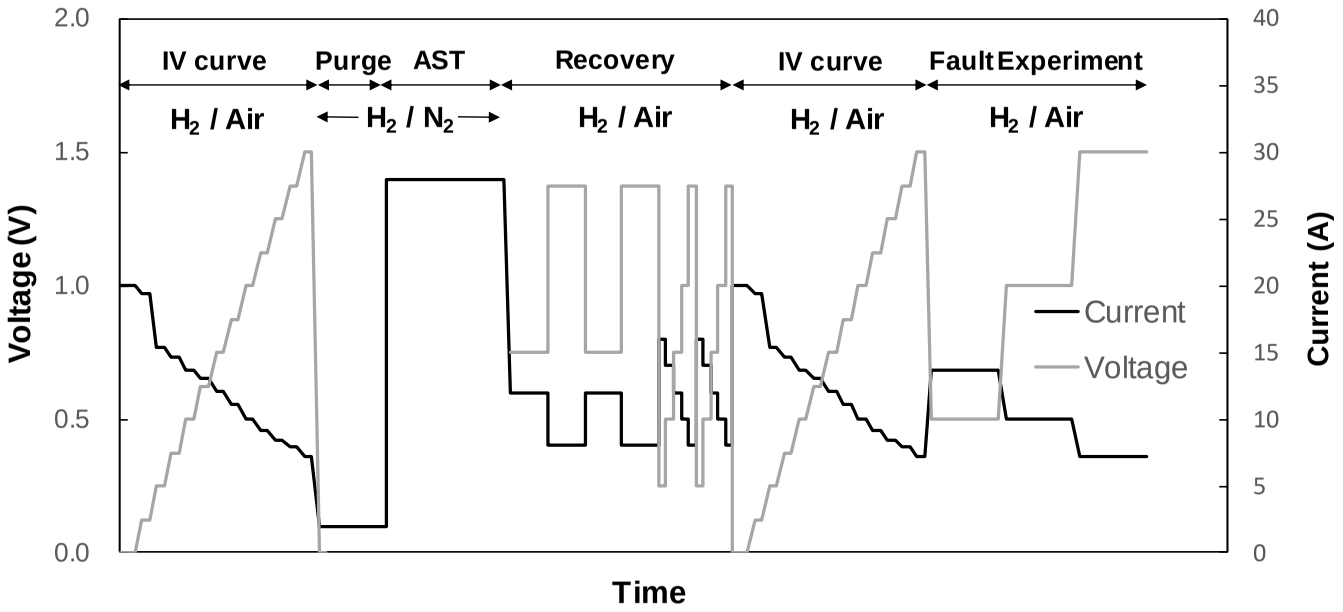

Figure 5.3 Experimental procedure

the AST, cathode reactant is changed to nitrogen gas and the purge has proceeded. Then, 1.4 V overvoltage is applied to the fuel cell. While the AST, carbon corrosion has proceeded and performance of the fuel cell decreases. After an hour of AST, PEMFC performance recovery is made. With the recovery process, the performance of the over degraded fuel cell rises and stabilized. At this stage, the polarization curve is measured once again. Then finally, the fault experiment proceeds under current loads at 10A, 20A, 30A. The current loads correspond to the current densities at 0.4 A/cm^2, 0.8 A/cm^2, 1.2 A/cm^2.

5.4 Current distribution characteristics

5.4.1 Local current distribution change with accelerated stress test

The evolution of PEMFC performance with the accelerated stress test (AST) is shown in Fig. 5.4. With the AST, the performance of the fuel cell decreases. Before the AST, in other words, beginning of life (BoL), fuel cell showed 0.584 V at the current density of 1.2 A/cm^2. After 8 hours of AST, the fuel cell showed 0.436 V at 1.2 A/cm^2. The voltage of the fuel cell decreased about 25%. This state (after 8 hours of AST) will be referred to as the end of life (EoL) in this paper. Overall, the polarization curve decreases with the AST. But its decrement is bigger with the higher current load condition.

The evolution of local current distribution change under AST is shown in Fig. 5.5. Current distributions under current load at 10 A (0.4 A/cm^2) are presented in Fig. 5.5(a). Local area A, which is near the reactant inlet region, shows the highest current flow. Along the reactant flow direction from A to E, current flow at each local area decreases. This is mainly due to the decreasing reactant concentration at the local spots along the flow channel. With the AST, current flow at the inlet region takes more current distribution portion, and that of the outlet region decreases. Since the fuel cell is under galvanostatic mode

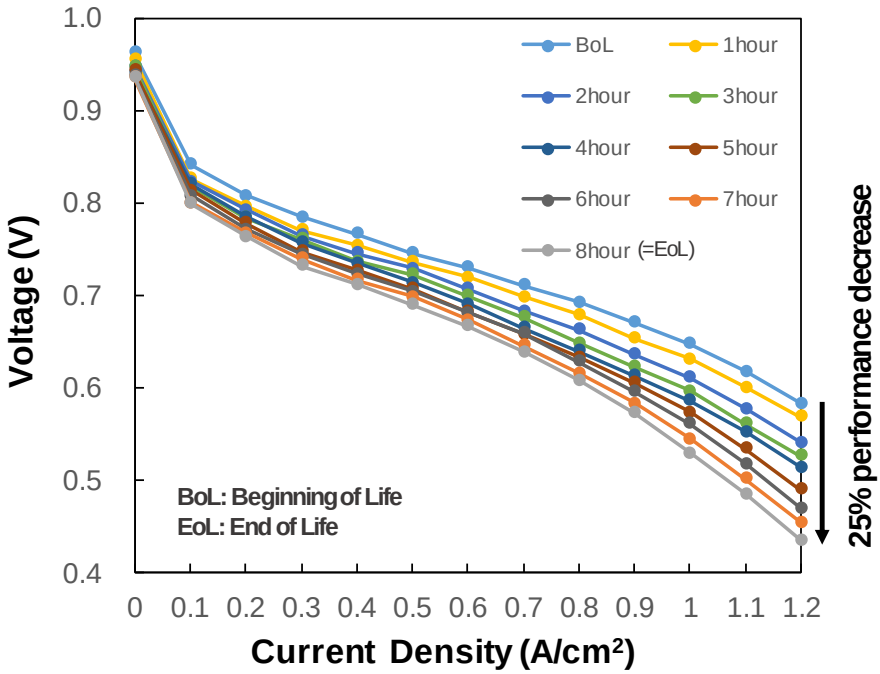

Figure 5.4 Evolution of current distribution with accelerated stress test

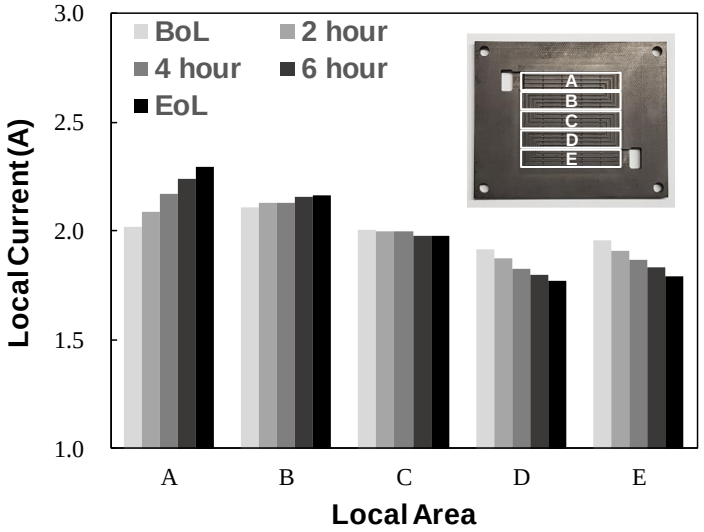

(a)

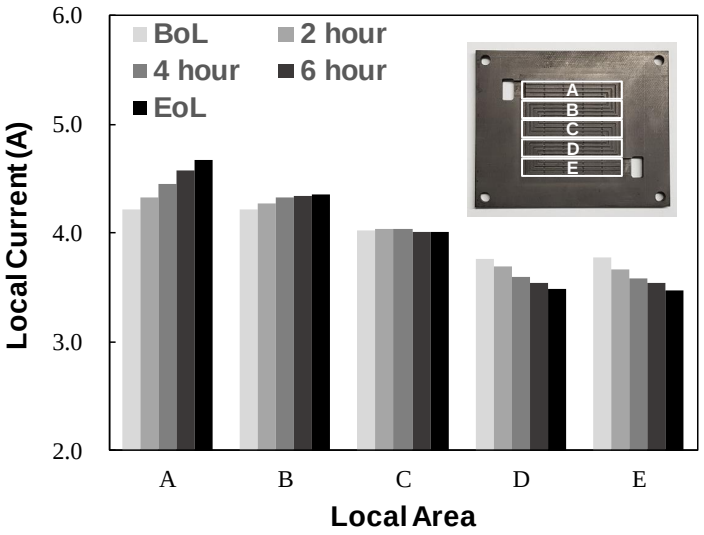

(b)

Figure 5.5 Evolution of current distribution under (a) 10 A (b) 20 A (c) 30 A

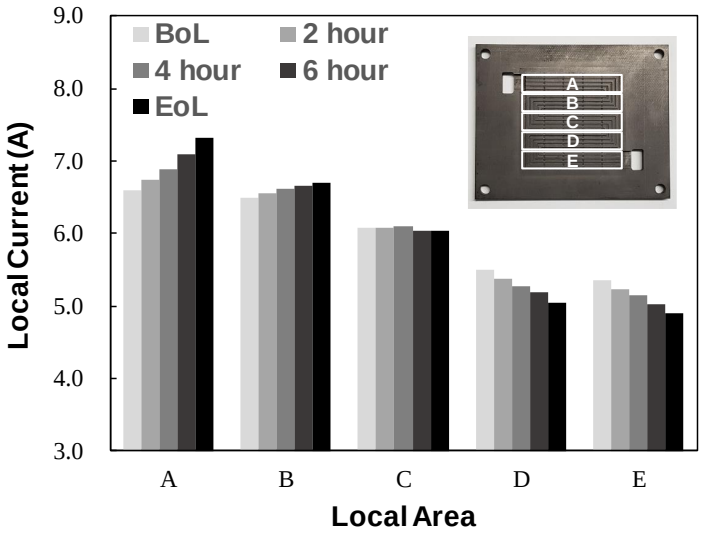

(c)

Figure 5.5 Evolution of current distribution under (a) 10 A (b) 20 A (c) 30 A (Continued)

under 10 A load condition, the sum of the current flows should be preserved. Therefore, an increase of a specific local current flow induces a decrease in another local area's current flow.

As with the current load elevation (Fig. 5.5(b), Fig 5.5(c)), non-uniformity due to the higher current flows at the inlet region gets more severe. In other words, the current distribution slope from A to E gets steeper with the higher current load. This slope also gets steeper with the degradation under the higher current load. This phenomenon is reported in other papers [60,91]. The papers also observed more severe carbon corrosion in the outlet region. It seems that the higher liquid water accumulation at the outlet region is a more suitable condition for carbon corrosion.

5.4.2 Local current distribution change under faults

Local current distributions are observed under faulty conditions. Fault related to the APS is simulated by varying the cathode SR. Under severe degradation of the air blower or air leakage can reduce the reactant supply to the stack. On the other hand, degradation of the airflow meter can lead to increased airflow to the stack. In Fig. 5.6(a), local current distribution change with varying cathode SR is suggested. The distribution is measured under non

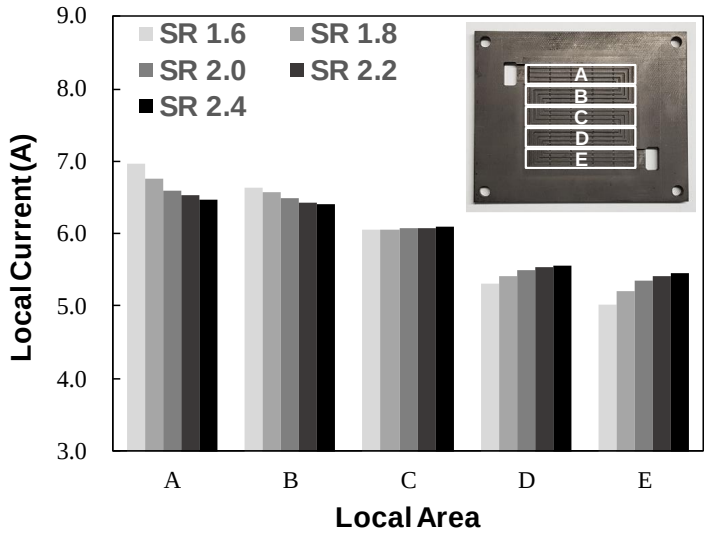

(a)

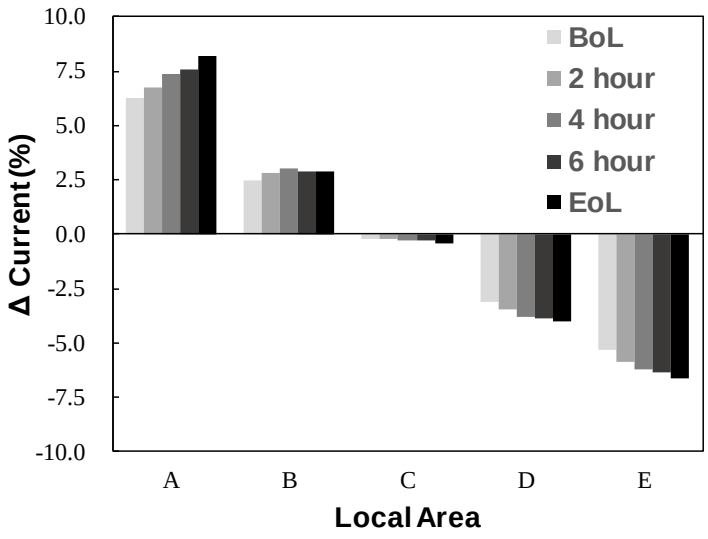

(b)

Figure 5.6 Current distribution change under air supply fault at 30 A

(a) Effect of SR (b) Effect of AST under 20% decreased air SR

degraded state (BoL) at current load of 30 A. With the lesser air flow, current distribution shifts to the inlet. With more airflow, on the contrary, the distribution shifts to the outlet, resulting in more uniform current distribution. In general, the outlet region suffers from insufficient reactant concentration due to the consumed reactant in the inlet region and increased water concentration. With more air SR, therefore, it is reasonable to have a more uniform current distribution.

Fault experiments are also performed under degraded states with AST. Local current distribution with AST under 20% cathode air decreased state (SR=1.6) is shown in Fig. 5.6(b). Y-axis represents the residuals of the current flow compared to its normal state. For example, if the current flow value at local area A is 6.1 A at normal state and 6.4 A in a fault state, residual due to the fault is 0.3 A. At the current load of 30 A, each local area is expected to have the current flow of 6.0A ideally (uniform current distribution condition). Then, the current residual is divided into 6.0 A. As a result, the residual percentage value is represented as 5.0%. At the beginning of life (BoL) state under 20% decreased air SR, current flows are more concentrated in the inlet region. With the AST cycle, this unbalanced current distribution gets more severe. Performance decrement in the outlet region due to the carbon corrosion leads to the decreased current flow. The decreased current flow is compensated at the

inlet region, resulting in increased current flow.

Fault responses under humidification fault and temperature fault are suggested in Fig. 5.7(a) and Fig. 5.7(b), respectively. When the inlet air humidity decreases from 80% to 40%, current flows in the inlet region decrease while those of the outlet region increase. This is due to the insufficient membrane humidification in the inlet region under the humidification fault [74]. The decrement is compensated at the outlet region. The humidification fault response does not seem to show a clear trend as the air SR fault with the AST. Nevertheless, decreased current flow at the inlet and increased current flow in the outlet are clearly shown.

PEMFCs are widely known to have an optimal operating temperature between 60~80^{o}C [94-96]. The optimal point can vary depending on the membrane type and gas diffusion layer type. Flow channels and shapes can also affect the optimal temperature condition. Therefore, an increase in operating temperature cannot always be seen as a fault. Nevertheless, this chapter focuses on the current distribution change with the temperature elevation. Therefore, an increase of 5^{o}C operating temperature will be referred to as temperature fault. Under the fault, inlet current flow decreases compared to the normal state. This seems to be a similar effect of decreased humidification in the inlet region. An increase in operating temperature led to the decrease of relative humidity.

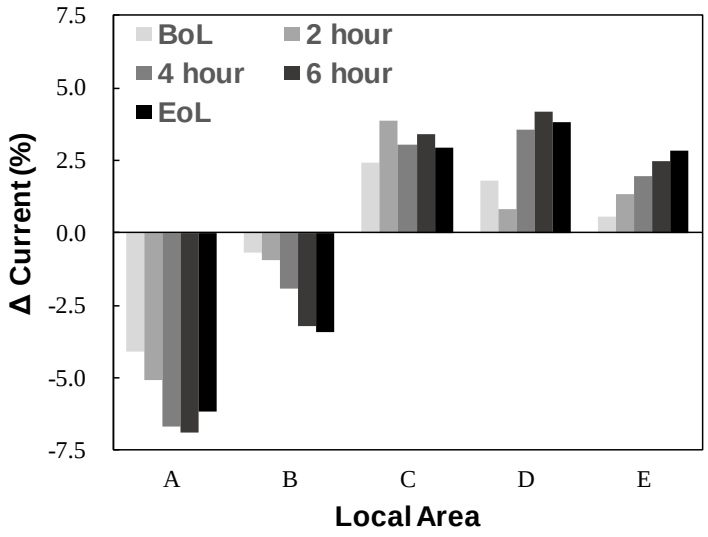

(a)

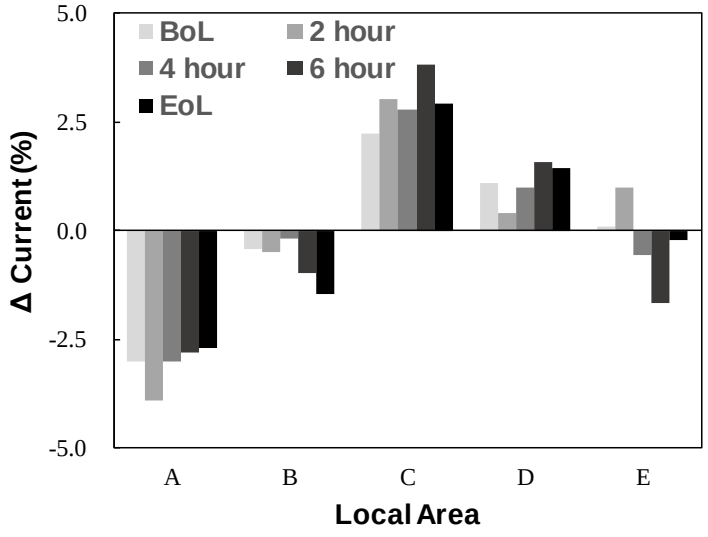

(b)

Figure 5.7 Current distribution change with AST at 30 A

(a) 40% decreased air humidity (b) 5°C temperature increase

5.5 Model development

5.5.1 Neural network models

Overview of the experimental data and corresponding results with neural network-based models are suggested in Fig. 5.8. First, local current distribution data is collected under various operating conditions; pressure, temperature, stoichiometric ratio and relative humidity. Using the data, the prediction model for local current distribution under various operating conditions is developed in chapter 4. The effectiveness of the model is validated. Also, the fact that cathode SR, cathode RH and temperature are dominant parameters on local current distribution is checked.

In this chapter, an accelerated stress test (AST) is performed by applying 1.4 V overvoltage to the fuel cell for 8 hours. While the process, performance curve data is collected. Also, three fault scenarios are set and performed during the AST. The scenarios match the key operating parameters found in chapter 4. In subchapter 5.5, a method for modeling current distribution with the AST data will be suggested. The developed model with the method is expected to predict the current distribution change under degradation. Also, a method for modeling fault response under fault conditions will be suggested.

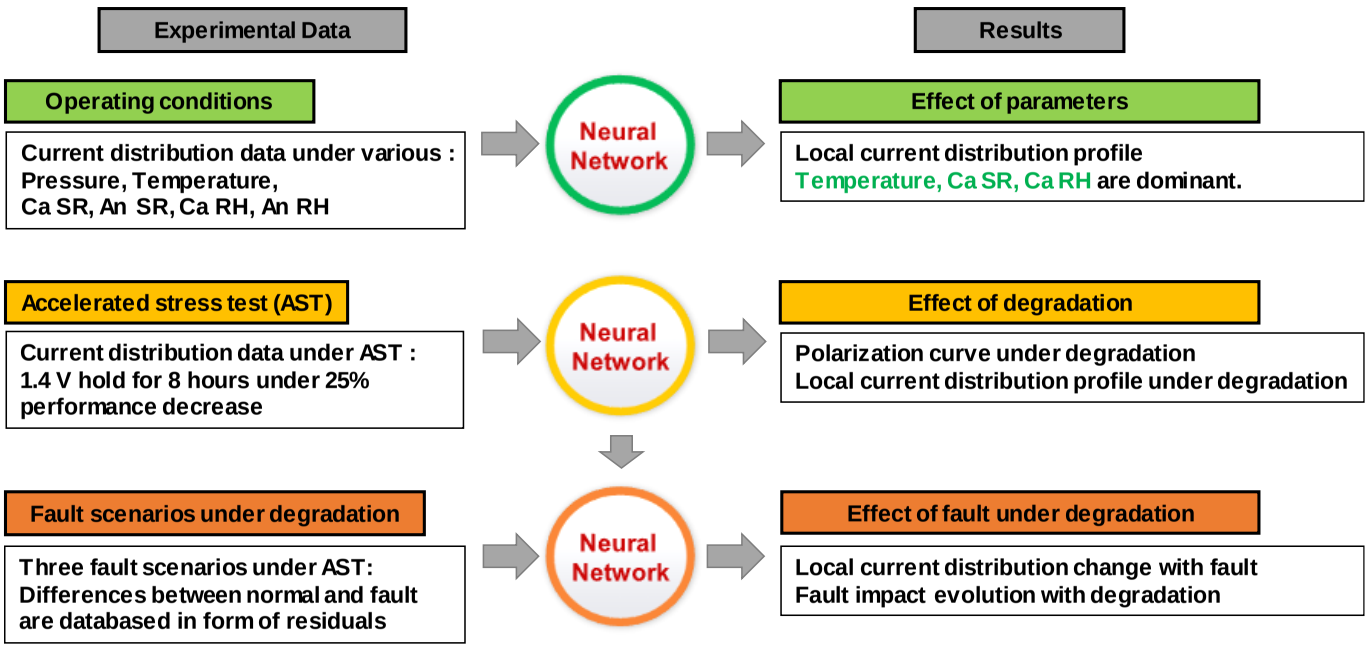

Figure 5.8 Overview on the local current distribution models

The structure of the neural network-based current distribution prediction model is suggested in Fig. 5.9. Figure 5.9(a) shows the inputs and outputs of the model. Since the operating condition is fixed, time and current density are the only inputs. Pre-conditioner rearranges the time and current density values. For the time, AST time is divided into 8 hours. For the current density, current load is divided into its maximum load condition, 1.2 A/cm^2. The post-conditioner will be explained on the next page. The current distribution neural network model has three hidden layers with five nodes each (5-5-5), as shown in Fig. 5.9(b). The fault response prediction model also has three hidden layers, but with more nodes (10-10-10).

The working principle of the fault response prediction model is shown in Fig. 5.10. The model returns local current difference values. In other words, the model returns changes due to the fault. In order to predict local current distribution under fault, therefore, current distribution should be acquired with the current distribution prediction model firstly. Then, the changes due to the fault are predicted with the fault response model. Finally, the predicted local current distribution value under fault is acquired with the addition.

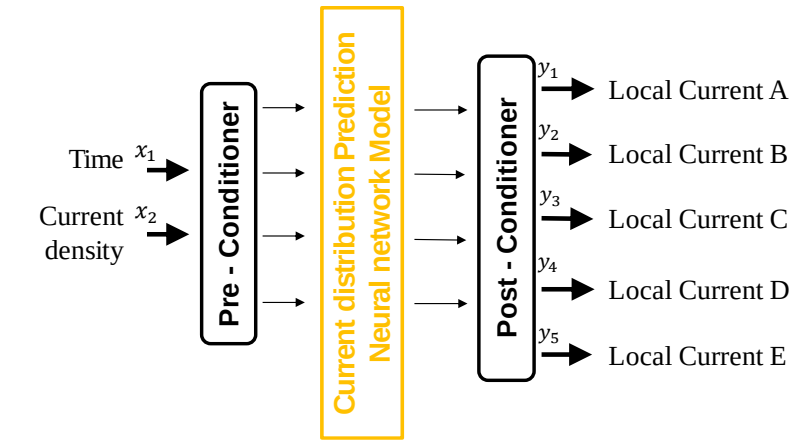

(a)

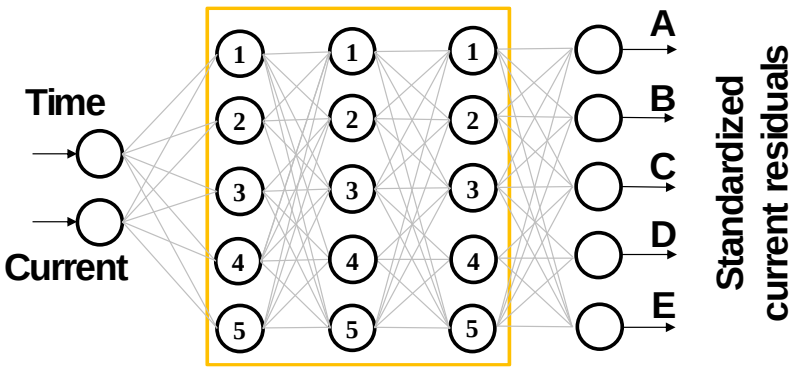

(b)

Figure 5.9 Current distribution prediction model

(a) Inputs and outputs (b) neural network structure

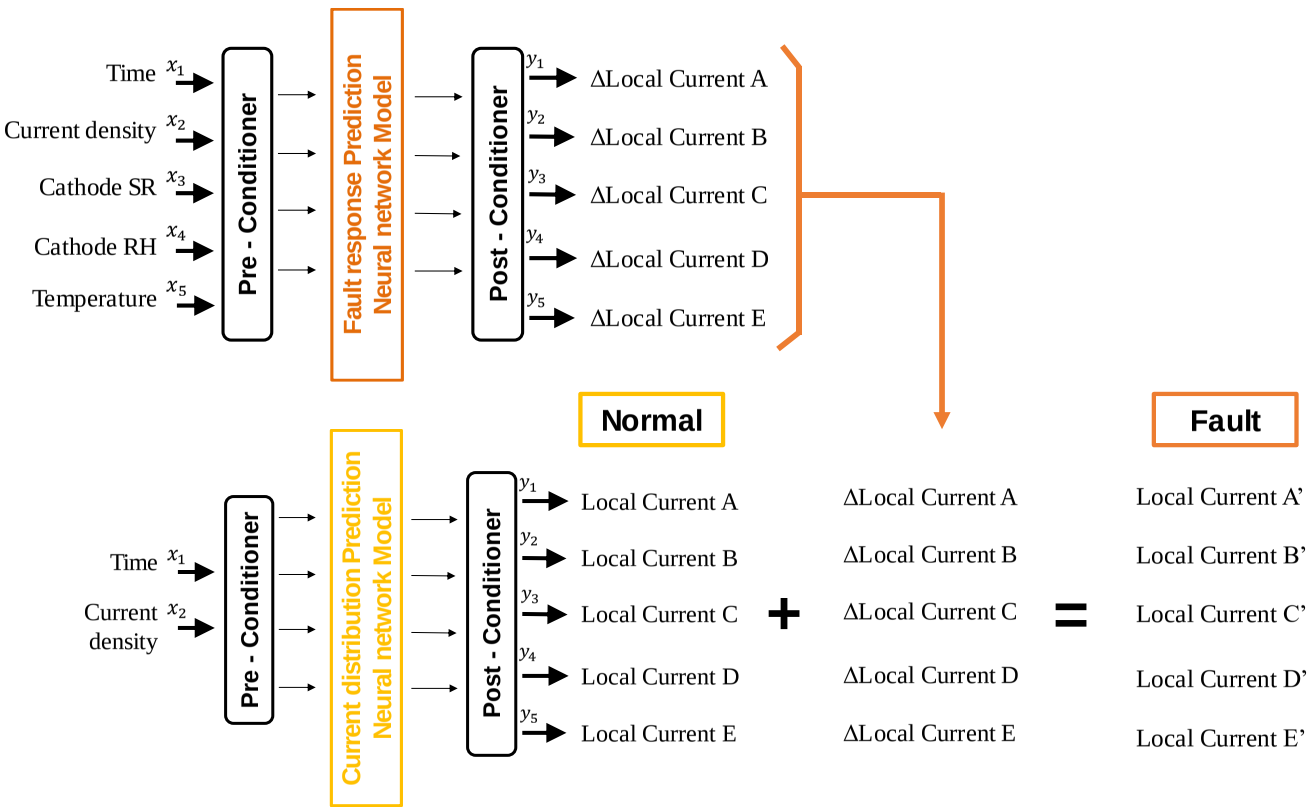

Figure 5.10 Working principle of fault response prediction model

5.5.2 Data conditioning

Before the training, data should be properly conditioned. In other words, data should be transformed into a standardized form. Figure 5.11 shows the data conditioning process. The collected current distribution data under AST should be transformed for the model training. This process is the reversal process of the post-conditioner (Fig. 5.11(a)). Figure 5.11(b) shows the current distribution data under current loads at 10A, 20A and 30A. The averaged value at each local area is 2 A, 4 A and 6 A, respectively. The gap between the averaged value and the measured value is residual. As shown in Fig. 5.11(c), these residuals are bigger at the higher current load conditions. When the neural network is trained with the residuals, the model will return bigger residuals in response to higher current density input. Therefore, the characteristics of the current distribution will not be reflected in the model. So in Fig. 5.11(c), the residuals are divided into its averaged value for the standardization.

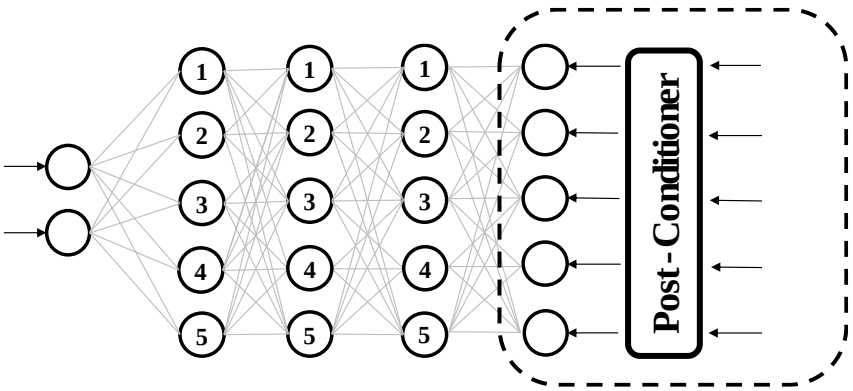

(a)

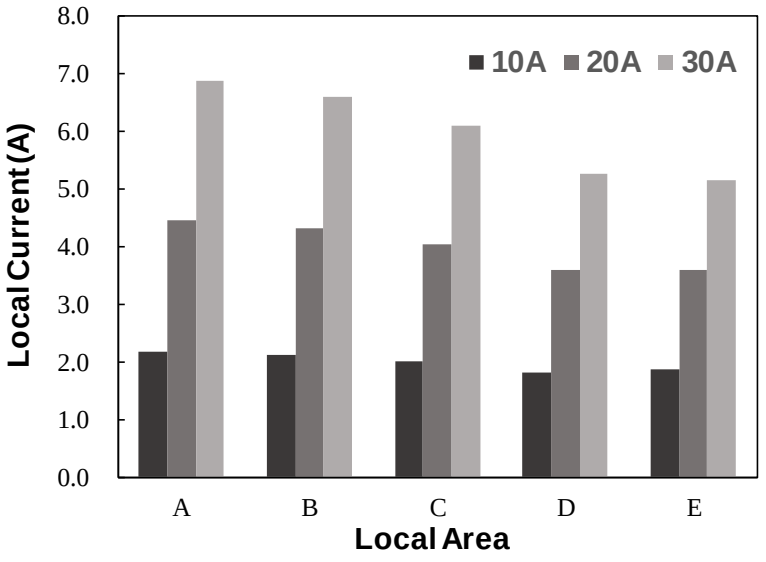

(b)

Figure 5.11 Data conditioning process

(a) Reverse post conditioner (b) Residuals (c) Standardized residuals

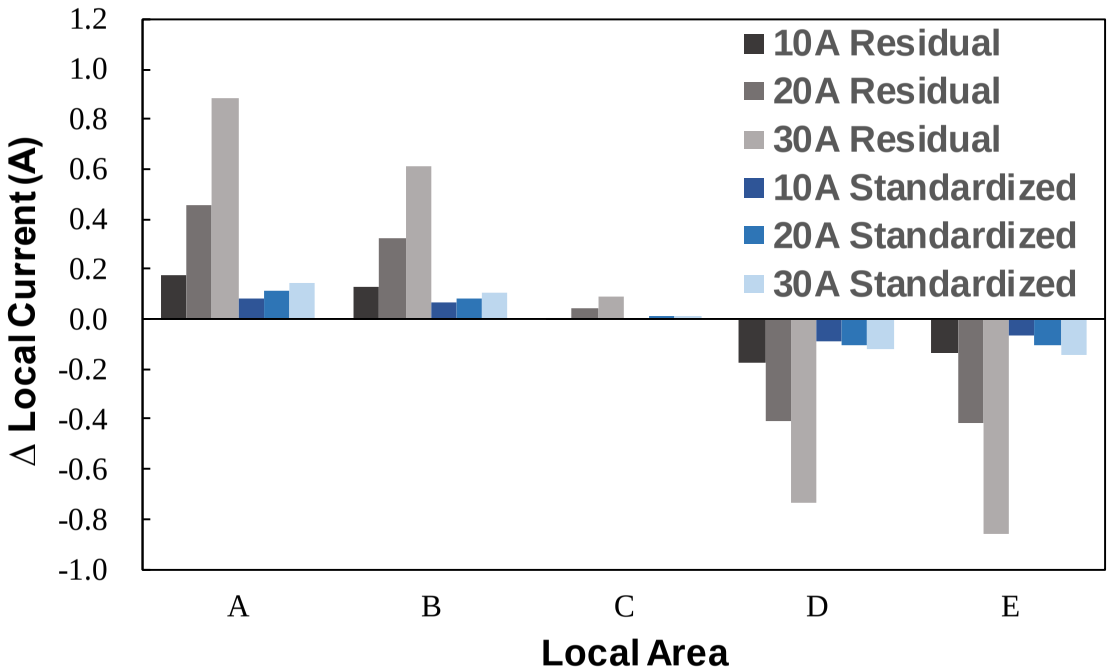

(c)

Figure 5.11 Data conditioning process (a) Reverse post conditioner (b) Residuals (c) Standardized residuals

5.5.3 Model training

The basic tool and process for model training are the same as in chapter 4. During the 8 hours of AST, the performance curve is measured nine times, including the BoL and EoL. The fault data is collected under five different AST conditions; BoL, 2 hours of AST, 4 hours of AST, 6 hours of AST and 8 hours of AST (EoL). The data under the AST for 4 hours is used for the test data. The rest data is used for the model training.

In Table 5.2, an example of cross-fold validation is suggested. When the training dataset is not enough, the training data set is divided into few groups. Each group, in other words, fold, takes a turn to be a validation set. In Table 5.2, there are four-folds. The hyper-parameters are optimized to find the appropriate training point between the under fitting and overfitting. When the hyper-parameters are optimized, the test data is put into the model to validate the model.

In the case of chapter 4, current distribution data after 4 hours of AST and fault data under AST for 4 hours are used as test set data. The rest are divided into four groups, as shown in Table 5.3. Then the 4-fold cross-validation has proceeded. After the optimization, the model is validated with the test data.

Table 5.2 Cross-fold validation

Training Set				Test set
Fold 1 (Validation)	Fold 2	Fold 3	Fold 4	Test data
Fold 1	Fold 2 (Validation)	Fold 3	Fold 4	
Fold 1	Fold 2	Fold 3 (Validation)	Fold 4	
Fold 1	Fold 2	Fold 3	Fold 4 (Validation)	

Table 5.3 Cross-fold validation with experimental data

Experimental Data (AST for 8 hours: 25% Performance degradation)				
Training Set				Test set
0 hour AST (BoL)	1 hour AST	2 hour AST	3 hour AST	4 hour AST
5 hour AST	6 hour AST	7 hour AST	8 hour AST (EoL)	

5.6 Prediction results

The model validation results are shown and discussed in this sub-chapter. Firstly, the prediction result of the local current prediction after 4 hours of AST is suggested in Fig. 5.12. The predicted result with the model is compared to the experimental results under current loads at 10 A, 20 A and 30 A. Regardless of the current load condition, the model predicted the current distribution very precisely. The mean absolute error (MAE) between the predicted value and experimented value is 0.88%.

Next, the fault response prediction model is validated in Fig. 5.13. The graph shows local current distribution changes under three different fault conditions; 20% decreased air SR, 40% decreased relative humidity and 5^{o}C increased operating temperature. Overall, the prediction residuals of the model followed the experimental residuals very well. The model followed the increase and decrease of the current flows at the local spots correctly. Excluding the normal state prediction results, which are determined with the current prediction model, the fault response prediction model showed a 1.25% mean absolute error (MAE) difference compared to the experimental data.

When considering the normal state prediction value as shown in Fig. 5.10, both prediction results should be combined. In other words, the result shown in

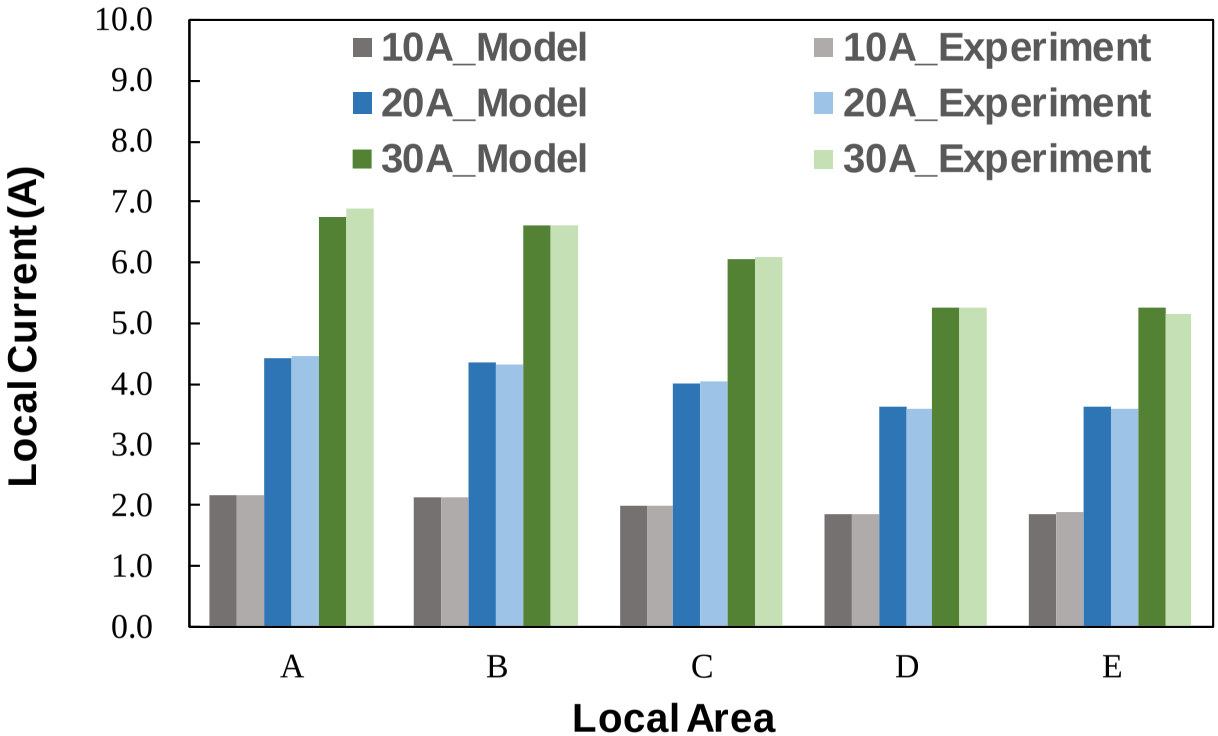

Figure 5.12 Current distribution prediction model prediction results (AST for 4 hours)

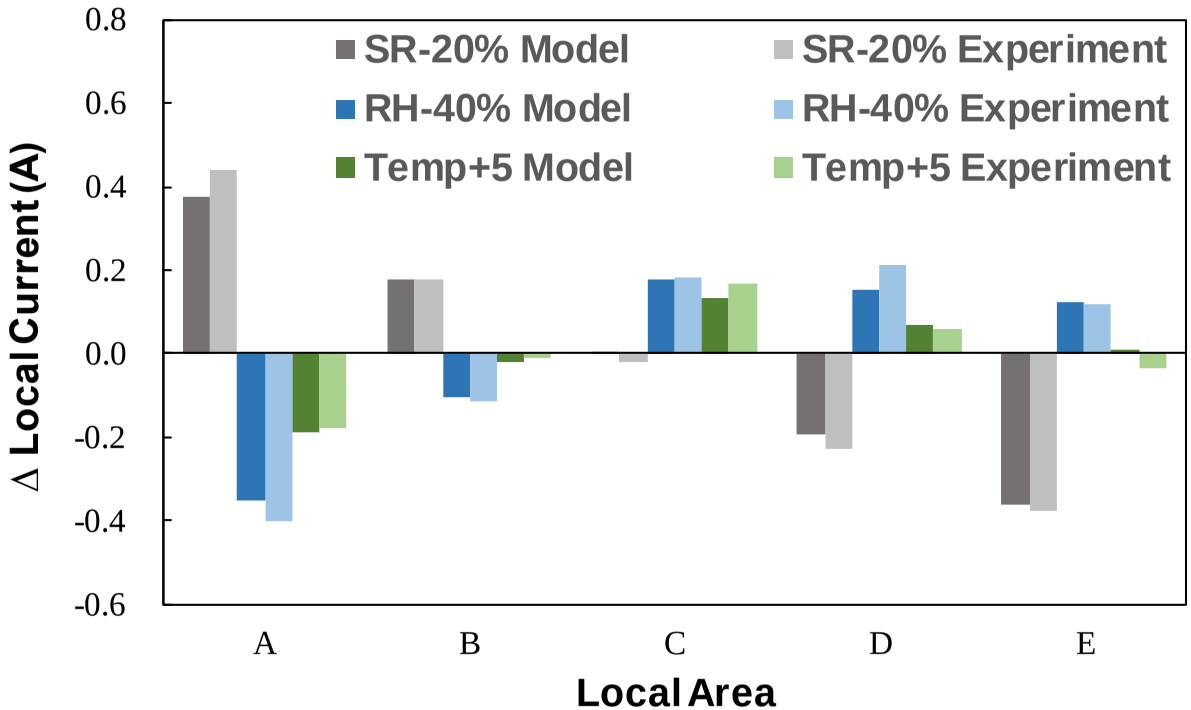

Figure 5.13 Fault response prediction model residual prediction results (AST for 4 hours / Load 30 A)

Fig. 5.13 should be added to the result suggested in Fig. 5.12. As a final result, local current distributions under 4 hours of AST and fault conditions are acquired (Fig. 5.14). The mean absolute error (MAE) between the predicted distribution and experimental distribution is 0.8%. As shown in the graph (Fig. 5.14) predicted current flows at the local spots match the experimental current flows.

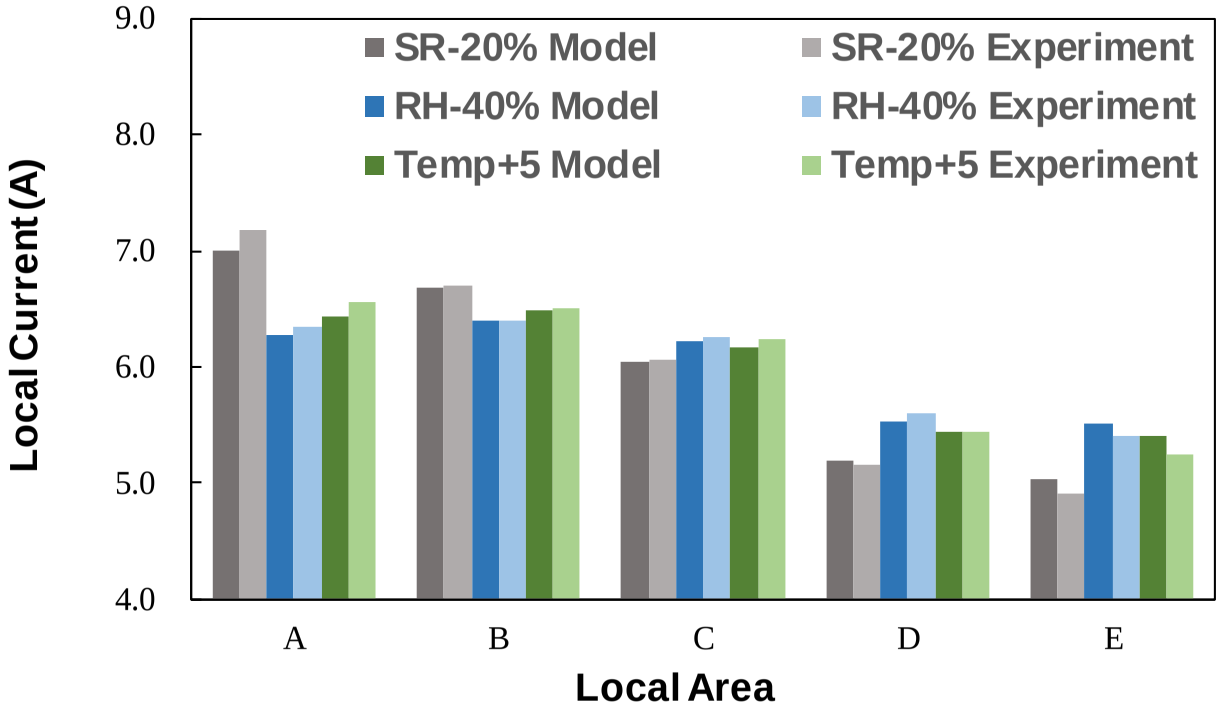

Figure 5.14 Fault response prediction model Prediction results (AST for 4 hours / Load 30 A)

5.7 Summary

In this chapter, local current distribution prediction under fuel cell degradation and fault mode has proceeded. First, local current distribution evolution data under the degradation is collected with an accelerated stress test (AST). Second, a fault experiment is performed between the accelerated stress test to collect current distribution changes under faulty conditions. On the basis of the modeling method suggested in chapter 4, modifications are made using the standardized residual approach. As a result, the current distribution prediction model and fault response prediction model are successfully trained and showed good performance. The prediction results show less than 1% mean absolute error with both the current distribution prediction model and fault response prediction model.

Chapter 6. Concluding remarks

A fault is one of the main reasons that reduce the reliability and durability of the system. Therefore, fault diagnosis technology is essentially required to protect the system. This paper suggests a new fault diagnostic method for PEMFC. When developing a fault diagnostic algorithm, the algorithm's robustness and sensitivity are in the trade-off position. The suggested method achieves both robustness and sensitivity by applying multiple diagnostic neural networks based on fault severity. Also, the suggested method does not require experimental fault data. When used in the commercial PEMFC system development process, it can save cost and time for the fault experiment.

Seventeen different fault scenarios are considered in this study. Some faults are classified in detail depending on their fault severity. The scenarios are grouped into a critical fault group, a significant fault group and a minor fault group. The fault experiment data is performed with the 1 kW class PEMFC system. As the severity of the fault gets intense, the fault response magnitude was larger and faster. Focusing on these characteristics, moving average time and normalization magnitude is adjusted before feeding into the diagnosis algorithm. As a result, the developed severity-based fault diagnosis algorithm diagnosed all the fault scenarios successfully.

Fault response is also investigated from the viewpoint of current distribution inside the PEMFC. With the application of segmented fuel cell, local current distribution is collected under various operating conditions before the fault experiment. With the collected data, a current distribution prediction model is developed with the modeling method suggested in this study. Effects of pressure, temperature, air stoichiometric ratio and air relative humidity on the current distribution is firstly investigated. The results showed that the current distribution prediction model is very effective and precise.

With the modeling method, an attempt to predict local current distribution under degradation and fault is made. An accelerated stress test is applied to the fuel cell to simulate the degradation of the fuel cell. Also, faulty conditions are applied to the fuel cell during the accelerated stress test. With the collected data, a model that predicts current distribution under degradation is developed and validated. A model that predicts current distribution change under fault is developed and validated. Comparing the results, both models showed good prediction performance less than 1% mean average error.

Overall, neural network technology is applied to develop the fault diagnosis algorithm and the current distribution prediction model. Introducing neural network technology to the field of PEMFC, simple but practical and powerful modeling is capable. In conclusion, severity-based fault diagnostic

algorithm and current distribution modeling method using limited experimental data are suggested in this study. The author believes that these suggestions will be effectively working when applied to the development process of commercial PEMFC.

References

[1] B. Pivovar, "H2@Scale Workshop Report," 2017. [Online]. Available: https://www.osti.gov/servlets/purl/1350015.

[2] R. E. Yonoff, G. V. Ochoa, Y. Cardenas-Escorcia, J. I. Silva-Ortega, and L. Meriño-Stand, “Research trends in proton exchange membrane fuel cells during 2008–2018: A bibliometric analysis,” *Heliyon*, vol. 5, no. 5, p. e01724, 2019.

[3] T. Sutharssan, D. Montalvao, Y. K. Chen, W. C. Wang, C. Pisac, and H. Elemara, “A review on prognostics and health monitoring of proton exchange membrane fuel cell,” *Renew. Sustain. Energy Reviews*, vol. 75, pp. 440–450, 2017.

[4] B. Tanç, H. T. Arat, E. Baltacıoğlu, and K. Aydın, “Overview of the next quarter century vision of hydrogen fuel cell electric vehicles,” *Int. J. Hydrogen Energy*, vol. 44, no. 20, pp. 10120–10128, 2019.

[5] L. Eudy, “Technology Acceleration: Fuel Cell Bus Evaluations,” 2019. [Online]. Available: https://www.osti.gov/servlets/purl/1518591.

[6] L. Eudy and M. Post, “SunLine Transit Agency American Fuel Cell Bus Progress Report, Data Period Focus: January 2017–July 2019,” 2020. [Online]. Available: https://www.osti.gov/servlets/purl/1659871.

[7] W. Y. Lee, H. Oh, M. Kim, Y. Y. Choi, Y. J. Sohn, and S. G. Kim,

"Hierarchical fault diagnostic method for a polymer electrolyte fuel cell system," *Int. J. Hydrogen Energy*, vol. 45, no. 47, pp.25733-25746, 2020.

[8] H. Oh, W. Y. Lee, J. Won, M. Kim, Y. Y. Choi, and S. Bin Han, "Residual-based fault diagnosis for thermal management systems of proton exchange membrane fuel cells," *Appl. Energy*, vol. 277, p. 115568, 2020.

[9] Z. Zheng *et al.*, "A review on non-model based diagnosis methodologies for PEM fuel cell stacks and systems," *Int. J. Hydrogen Energy*, vol. 38, no. 21, pp. 8914–8926, 2013.

[10] R. Petrone *et al.*, "A review on model-based diagnosis methodologies for PEMFCs," *Int. J. Hydrogen Energy*, vol. 38, no. 17, pp. 7077–7091, 2013.

[11] Z. Gao, C. Cecati, and S. X. Ding, "A survey of fault diagnosis and fault-tolerant techniques-part I: Fault diagnosis with model-based and signal-based approaches," *IEEE Trans. Ind. Electron.*, vol. 62, no. 6, pp. 3757–3767, 2015.

[12] Z. Zheng, M. C. Péra, D. Hissel, M. Becherif, K. S. Agbli, and Y. Li, "A double-fuzzy diagnostic methodology dedicated to online fault diagnosis of proton exchange membrane fuel cell stacks," *J. Power*

Sources, vol. 271, pp. 570–581, 2014.

[13] A. Escobet, À . Nebot, and F. Mugica, “PEM fuel cell fault diagnosis via a hybrid methodology based on fuzzy and pattern recognition techniques,” *Eng. Appl. Artif. Intelligence*, vol. 36, pp. 40–53, 2014.

[14] I. S. Lim, J. Y. Park, E. J. Choi, and M. S. Kim, “Efficient fault diagnosis method of PEMFC thermal management system for various current densities,” *Int. J. Hydrogen Energy*, vol. 46, no. 2, pp. 2543–2554, 2021.

[15] Z. Li, R. Outbib, D. Hissel, and S. Giurgea, “Data-driven diagnosis of PEM fuel cell: A comparative study,” *Control Eng. Pract.*, vol. 28, pp. 1–12, 2014.

[16] Z. Li *et al.*, “Online implementation of SVM based fault diagnosis strategy for PEMFC systems,” *Appl. Energy*, vol. 164, pp. 284-293, 2016.

[17] J. Y. Park, I. S. Lim, E. J. Choi, and M. S. Kim, “Fault diagnosis of thermal management system in a polymer electrolyte membrane fuel cell,” *Energy*, vol. 214, p. 119062, 2021.

[18] S. Giurgea, R. Tirnovan, D. Hissel, and R. Outbib, “An analysis of fluidic voltage statistical correlation for a diagnosis of PEM fuel cell flooding,” *Int. J. Hydrogen Energy*, vol. 38, no. 11, pp. 4689–4696,

2013.

[19] N. Fouquet, C. Doulet, C. Nouillant, G. Dauphin-Tanguy, and B. Ould-Bouamama, “Model based PEM fuel cell state-of-health monitoring via ac impedance measurements,” *J. Power Sources*, vol. 159, no. 2, pp. 905–913, 2006.

[20] N. Yousfi Steiner, D. Hissel, P. Moçtéguy, and D. Candusso, “Diagnosis of polymer electrolyte fuel cells failure modes (flooding & drying out) by neural networks modeling,” *Int. J. Hydrogen Energy*, vol. 36, no. 4, pp. 3067–3075, 2011.

[21] S. Laribi, K. Mammar, Y. Sahli, and K. Koussa, “Analysis and diagnosis of PEM fuel cell failure modes (flooding & drying) across the physical parameters of electrochemical impedance model: Using neural networks method,” *Sustain. Energy Technol. Assessments*, vol. 34, pp. 35–42, 2019.

[22] M. Shao, X. J. Zhu, H. F. Cao, and H. F. Shen, “An artificial neural network ensemble method for fault diagnosis ofproton exchange membrane fuel cell system,” *Energy*, vol. 67, pp. 268–275, 2014.

[23] E. Pahon, N. Yousfi Steiner, S. Jemei, D. Hissel, and P. Moçoteguy, “A signal-based method for fast PEMFC diagnosis,” *Appl. Energy*, vol. 165, pp. 748–758, 2016.

[24] M. M. Kamal, D. W. Yu, and D. L. Yu, “Fault detection and isolation for PEM fuel cell stack with independent RBF model,” *Eng. Appl. Artif. Intell.*, vol. 28, pp. 52–63, 2014.

[25] S. De Lira, V. Puig, J. Quevedo, and A. Husar, “LPV observer design for PEM fuel cell system: Application to fault detection,” *J. Power Sources*, vol. 196, no. 9, pp. 4298–4305, 2011.

[26] Y. Wang, D. F. Ruiz Diaz, K. S. Chen, Z. Wang, and X. C. Adroher, “Materials, technological status, and fundamentals of PEM fuel cells – A review,” *Mater. Today*, vol. 32, pp. 178–203, 2020.

[27] Z. Hu *et al.*, “A novel diagnostic methodology for fuel cell stack health: performance, consistency and uniformity,” *Energy Convers. Manag.*, vol. 185, pp. 611–621, 2019.

[28] S. J. C. Cleghorn, C. R. Derouin, M. S. Wilson, and S. Gottesfeld, “A Printed Circuit Board approach to measuring current distribution in a fuel cell,” *J. Appl. Electrochem.*, vol. 28, no. 7, pp. 663–672, 1998.

[29] J. J. Hwang, D. Y. Wang, and N. C. Shih, “Development of a lightweight fuel cell vehicle,” *J. Power Sources*, vol. 141, no. 1, pp. 108–115, 2005.

[30] T. Reshetenko and A. Kulikovsky, “On the distribution of local current density along a PEM fuel cell cathode channel,” *Electrochem.*

commun., vol. 101, pp. 35–38, 2019.

[31] K. Takanohashi *et al.*, “Simultaneous visualization of oxygen partial pressure, current density, and water droplets in serpentine fuel cell during power generation for understanding reaction distributions,” *J. Power Sources*, vol. 343, pp. 135–141, 2017.

[32] Z. Liu, Z. Mao, B. Wu, L. Wang, and V. M. Schmidt, “Current density distribution in PEFC,” *J. Power Sources*, vol. 141, no. 2, pp. 205–210, 2005.

[33] Y.-G. Yoon, W.-Y. Lee, T.-H. Yang, G.-G. Park, and C.-S. Kim, “Current distribution in a single cell of PEMFC,” *J. Power Sources*, vol. 118, no. 1–2, pp. 193–199, 2003.

[34] P. C. Ghosh, T. Wüster, H. Dohle, N. Kimiaie, J. Mergel, and D. Stolten, “In situ approach for current distribution measurement in fuel cells,” *J. Power Sources*, vol. 154, no. 1, pp. 184–191, 2006.

[35] H. Sun, G. Zhang, L.-J. Guo, and H. Liu, “A novel technique for measuring current distributions in PEM fuel cells,” *J. Power Sources*, vol. 158, no. 1, pp. 326–332, 2006.

[36] F.-B. Weng, B.-S. Jou, C.-W. Li, A. Su, and S.-H. Chan, “The effect of low humidity on the uniformity and stability of segmented PEM fuel cells,” *J. Power Sources*, vol. 181, no. 2, pp. 251–258, 2008.

[37] D. H. Jeon, K. N. Kim, S. M. Baek, and J. H. Nam, “The effect of relative humidity of the cathode on the performance and the uniformity of PEM fuel cells,” *Int. J. Hydrogen Energy*, vol. 36, no. 19, pp. 12499–12511, 2011.

[38] R. Lin, C. Cao, J. Ma, E. Gülzow, and K. A. Friedrich, “Optimizing the relative humidity to improve the stability of a proton exchange membrane by segmented fuel cell technology,” *Int. J. Hydrogen Energy*, vol. 37, no. 4, pp. 3373–3381, 2012.

[39] V. Lilavivat, S. Shimpalee, J. W. Van Zee, H. Xu, and C. K. Mittelsteadt, “Current distribution mapping for PEMFCs,” *Electrochim. Acta*, vol. 174, pp. 1253–1260, 2015.

[40] B. Feng, R. Lin, D. Liu, and D. Zhong, “Study on the Uncoupling Characteristics of PEM Fuel Cell by Segmented Cell Technology,” *Int. J. Electrochem. Sci*, vol. 14, pp. 2175–2186, 2019.

[41] L. Peng, H. Shao, D. Qiu, P. Yi, and X. Lai, “Investigation of the non-uniform distribution of current density in commercial-size proton exchange membrane fuel cells,” *J. Power Sources*, vol. 453, p. 227836, 2020.

[42] D. Gerteisen, N. Zamel, C. Sadeler, F. Geiger, V. Ludwig, and C. Hebling, “Effect of operating conditions on current density distribution

and high frequency resistance in a segmented PEM fuel cell," *Int. J. Hydrogen Energy*, vol. 37, no. 9, pp. 7736–7744, 2012.

[43] D. Liang, M. Dou, M. Hou, Q. Shen, Z. Shao, and B. Yi, "Behavior of a unit proton exchange membrane fuel cell in a stack under fuel starvation," *J. Power Sources*, vol. 196, no. 13, pp. 5595–5598, 2011.

[44] M. Dou *et al.*, "Behaviors of proton exchange membrane fuel cells under oxidant starvation," *J. Power Sources*, vol. 196, no. 5, pp. 2759–2762, 2011.

[45] H. Shao, D. Qiu, L. Peng, P. Yi, and X. Lai, "In-situ measurement of temperature and humidity distribution in gas channels for commercial-size proton exchange membrane fuel cells," *J. Power Sources*, vol. 412, pp. 717–724, 2019.

[46] T. V Reshetenko, G. Bender, K. Bethune, and R. Rocheleau, "A segmented cell approach for studying the effects of serpentine flow field parameters on PEMFC current distribution," *Electrochim. Acta*, vol. 88, pp. 571–579, 2013.

[47] S.-G. Kim, M.-J. Kim, and Y.-J. Sohn, "Segmented cell approach for studying uniformity of current distribution in polymer electrolyte fuel cell operation," *Int. J. Hydrogen Energy*, vol. 40, no. 35, pp. 11676–11685, 2015.

[48] F. B. Weng, C. Y. Hsu, and C. W. Li, “Experimental investigation of PEM fuel cell aging under current cycling using segmented fuel cell,” *Int. J. Hydrogen Energy*, vol. 35, no. 8, pp. 3664–3675, 2010.

[49] D. Spernjak, J. D. Fairweather, T. Rockward, R. Mukundan, and R. Borup, “Characterization of Carbon Corrosion in a Segmented PEM Fuel Cell,” *ECS Trans.*, vol. 41, no. 1, pp. 741–750, 2019.

[50] R. Lin *et al.*, “Investigation of real-time changes and recovery of proton exchange membrane fuel cell in voltage reversal,” *Energy Convers. Manag.*, vol. 236, p. 114037, 2021.

[51] S. Komini Babu *et al.*, “Spatially resolved degradation during startup and shutdown in polymer electrolyte membrane fuel cell operation,” *Appl. Energy*, vol. 254, no. October 2018, p. 113659, 2019.

[52] J. Dillet *et al.*, “Impact of flow rates and electrode specifications on degradations during repeated startups and shutdowns in polymer-electrolyte membrane fuel cells,” *J. Power Sources*, vol. 250, pp. 68–79, 2014.

[53] R. Lin, F. Xiong, W. C. Tang, L. Técher, J. M. Zhang, and J. X. Ma, “Investigation of dynamic driving cycle effect on the degradation of proton exchange membrane fuel cell by segmented cell technology,” *J. Power Sources*, vol. 260, pp. 150–158, 2014.

[54] Y. H. Lai and G. W. Fly, “In-situ diagnostics and degradation mapping of a mixed-mode accelerated stress test for proton exchange membranes,” *J. Power Sources*, vol. 274, pp. 1162–1172, 2015.

[55] R. Lin, X. Cui, J. Shan, L. Técher, F. Xiong, and Q. Zhang, “Investigating the effect of start-up and shut-down cycles on the performance of the proton exchange membrane fuel cell by segmented cell technology,” *Int. J. Hydrogen Energy*, vol. 40, no. 43, pp. 14952–14962, 2015.

[56] J. Shan, R. Lin, S. Xia, D. Liu, and Q. Zhang, “Local resolved investigation of PEMFC performance degradation mechanism during dynamic driving cycle,” *Int. J. Hydrogen Energy*, vol. 41, no. 7, pp. 4239–4250, 2016.

[57] S. Chevalier, C. Josset, and B. Auvity, “Analytical solutions and dimensional analysis of pseudo 2D current density distribution model in PEM fuel cells,” *Renew. energy*, vol. 125, pp. 738–746, 2018.

[58] H. Y. Wang, W. J. Yang, and Y. B. Kim, “Analyzing in-plane temperature distribution via a micro-temperature sensor in a unit polymer electrolyte membrane fuel cell,” *Appl. Energy*, vol. 124, pp. 148–155, 2014.

[59] H. Askaripour, “Effect of operating conditions on the performance of a

PEM fuel cell," *Int. J. Heat Mass Transf.*, vol. 144, p. 118705, 2019.

[60] C. Yin *et al.*, "In situ investigation of proton exchange membrane fuel cell performance with novel segmented cell design and a two-phase flow model," *Energy*, vol. 113, pp. 1071–1089, 2016.

[61] C. Yin, Y. Gao, T. Li, G. Xie, K. Li, and H. Tang, "Study of internal multi-parameter distributions of proton exchange membrane fuel cell with segmented cell device and coupled three-dimensional model," *Renew. Energy*, vol. 147, pp. 650–662, 2020.

[62] W. Y. Lee, G. G. Park, T. H. Yang, Y. G. Yoon, and C. S. Kim, "Empirical modeling of polymer electrolyte membrane fuel cell performance using artificial neural networks," *Int. J. Hydrogen Energy*, vol. 29, no. 9, pp. 961–966, 2004.

[63] G. Napoli, M. Ferraro, F. Sergi, G. Brunaccini, and V. Antonucci, "Data driven models for a PEM fuel cell stack performance prediction," *Int. J. Hydrogen Energy*, vol. 38, no. 26, pp. 11628–11638, 2013.

[64] A. U. Chávez-Ramírez *et al.*, "High power fuel cell simulator based on artificial neural network," *Int. J. Hydrogen Energy*, vol. 35, no. 21, pp. 12125–12133, 2010.

[65] S. JemeÏJemei, D. Hissel, M.-Cé. PÉraPera, and J. M. Kauffmann, "A

new modeling approach of embedded fuel-cell power generators based on artificial neural network," *IEEE Trans. Ind. Electron.*, vol. 55, no. 1, pp. 437–447, 2008.

[66] M. Seyhan, Y. E. Akansu, M. Murat, Y. Korkmaz, and S. O. Akansu, "Performance prediction of PEM fuel cell with wavy serpentine flow channel by using artificial neural network," *Int. J. Hydrogen Energy*, vol. 42, no. 40, pp. 25619–25629, 2017.

[67] S. Ou and L. E. K. Achenie, "Artificial Neural Network Modeling of PEM Fuel Cells," *J. Fuel Cell Sci. Technol.*, vol. 2, no. 4, pp. 226–233, 2005.

[68] A. Saengrung, A. Abtahi, and A. Zilouchian, "Neural network model for a commercial PEM fuel cell system," *J. Power Sources*, vol. 172, no. 2, pp. 749–759, 2007.

[69] I.-S. Han and C.-B. Chung, "Performance prediction and analysis of a PEM fuel cell operating on pure oxygen using data-driven models: A comparison of artificial neural network and support vector machine," *Int. J. Hydrogen Energy*, vol. 41, no. 24, pp. 10202–10211, 2016.

[70] Y. Vural, D. B. Ingham, and M. Pourkashanian, "Performance prediction of a proton exchange membrane fuel cell using the ANFIS model," *Int. J. Hydrogen Energy*, vol. 34, no. 22, pp. 9181–9187,

2009.

[71] S. V Puranik, A. Keyhani, and F. Khorrami, “Neural network modeling of proton exchange membrane fuel cell,” *IEEE Trans. Energy Convers.*, vol. 25, no. 2, pp. 474–483, 2010.

[72] S. Laribi, K. Mammar, M. Hamouda, and Y. Sahli, “Impedance model for diagnosis of water management in fuel cells using artificial neural networks methodology,” *Int. J. Hydrogen Energy*, vol. 41, no. 38, pp. 17093–17101, 2016.

[73] F. Z. Arama, K. Mammar, S. Laribi, A. Necaibia, and T. Ghaitaoui, “Implementation of sensor based on neural networks technique to predict the PEM fuel cell hydration state,” *J. Energy Storage*, vol. 27, p. 101051, 2020.

[74] J. Y. Park, Y. H. Lee, I. S. Lim, Y. S. Kim, and M. S. Kim, “Prediction of local current distribution in polymer electrolyte membrane fuel cell with artificial neural network,” *Int. J. Hydrogen Energy*, vol. 46, no. 39, 2021, pp.20678-20692, 2021.

[75] Y.-J. Choi, G.-Y. Lee, K.-M. Kang, W.-G. Kim, and H.-C. Ju, “Computational Justification of Current Distribution Measurement Technique Via Segmenting Bipolar Plate in Fuel Cells,” *Transactions of the Korean hydrogen and new energy society*, vol. 21, no. 1. pp. 1–

11, 2010.

[76] Y. S. Kim, S. Il Kim, N. W. Lee, and M. S. Kim, “Study on a purge method using pressure reduction for effective water removal in polymer electrolyte membrane fuel cells,” *Int. J. Hydrogen Energy*, vol. 40, no. 30, pp. 9473–9484, 2015.

[77] Y. S. Kim, D. K. Kim, I. M. Kong, M. Kim, and M. S. Kim, “Local electrochemical characteristics at various operating pressure and temperature values using a segmented polymer electrolyte membrane fuel cell,” *J. Mech. Sci. Technol.*, vol. 30, no. 9, pp. 4391–4396, 2016.

[78] T. Reshetenko and A. Kulikovsky, “On the distribution of local current density along a PEM fuel cell cathode channel,” *Electrochem. commun.*, vol. 101, pp. 35–38, 2019.

[79] Y. S. Kim and D. K. Kim, “Operating strategy for successful start-up in self-humidified polymer electrolyte membrane fuel-cell system,” *Appl. Therm. Eng.*, vol. 152, pp. 370–376, 2019.

[80] Y. S. Kim, D. K. Kim, K. Y. Ahn, and M. S. Kim, “Real-time analysis of dry start-up characteristics of polymer electrolyte membrane fuel cell with water storage process under pressurized condition,” *Energy*, p. 117292, 2020.

[81] Y. S. Kim, D. K. Kim, K. Y. Ahn, and M. S. Kim, “Parametric study

on the local current distribution of polymer electrolyte membrane fuel cell with counter flow channel under pressurized condition," *J. Mech. Sci. Technol.*, vol. 34, no. 5, pp. 2189–2198, 2020.

[82] W. Y. Lee, Y. J. Sohn, S. G. Kim and M. Kim, "Fault Detection and Diagnosis Methods for Polymer Electrolyte Fuel Cell System," *Trans. of Korean Hydrogen and New Energy Society*, vol. 28, no. 3, pp. 252–272, 2017, doi: 10.7316/KHNES.2017.28.3.252.

[83] L. Placca and R. Kouta, "Fault tree analysis for PEM fuel cell degradation process modelling," *Int. J. Hydrogen Energy*, vol. 36, no. 19, pp. 12393–12405, 2011.

[84] J. Kurtz, S. Sprik, G. Saur, and S. Onorato, "Fuel Cell Electric Vehicle Durability and Fuel Cell Performance," 2018. [Online]. Available: www.nrel.gov/publications.

[85] Ž. Penga, G. Radica, and F. B. Fesb, "Degradation Mechanisms in Automotive Fuel Cell Systems." FCH-JU, GIANTLEAP, 2017.

[86] M. Pourbaix, *Atlas of Electrochemical Equilibria in Aqueous Solutions*. New York: Pergamon Press, 1966.

[87] N. Yousfi-Steiner, P. Moçotéguy, D. Candusso, and D. Hissel, "A review on polymer electrolyte membrane fuel cell catalyst degradation and starvation issues: Causes, consequences and diagnostic for

mitigation," *J. Power Sources*, vol. 194, no. 1, pp. 130–145, 2009.

[88] N. Macauley *et al.*, "Carbon Corrosion in PEM Fuel Cells and the Development of Accelerated Stress Tests," *J. Electrochem. Soc.*, vol. 165, no. 6, pp. F3148–F3160, 2018.

[89] Q. Meyer, Y. Zeng, and C. Zhao, "Electrochemical impedance spectroscopy of catalyst and carbon degradations in proton exchange membrane fuel cells," *J. Power Sources*, vol. 437, no. May, p. 226922, 2019.

[90] J. Jung *et al.*, "Electrochemical impedance analysis with transmission line model for accelerated carbon corrosion in polymer electrolyte membrane fuel cells," *Int. J. Hydrogen Energy*, vol. 43, no. 32, pp. 15457–15465, 2018.

[91] Y.H. Lee, "Study on the Current Density Distribution in Polymer Electrolyte Membrane Fuel Cell (PEMFC) System", Seoul National University, 2020.

[92] D. Spernjak, J. Fairweather, R. Mukundan, T. Rockward, and R. L. Borup, "Influence of the microporous layer on carbon corrosion in the catalyst layer of a polymer electrolyte membrane fuel cell," *J. Power Sources*, vol. 214, pp. 386–398, 2012.

[93] J. Y. Park, I. S. Lim, E. J. Choi, Y. H. Lee, and M. S. Kim,

"Comparative study of reverse flow activation and conventional activation with polymer electrolyte membrane fuel cell," *Renew. Energy*, vol. 167, pp. 162–171, 2021.

[94] E. J. Choi, S. H. Hwang, J. Park, and M. S. Kim, "Parametric analysis of simultaneous humidification and cooling for PEMFCs using direct water injection method," *Int. J. Hydrogen Energy*, vol. 42, no. 17, pp. 12531–12542, 2017.

[95] E. J. Choi, J. Y. Park, and M. S. Kim, "A comparison of temperature distribution in PEMFC with single-phase water cooling and two-phase HFE-7100 cooling methods by numerical study," *Int. J. Hydrogen Energy*, 2018.

[96] E. J. Choi, J. Y. Park, and M. S. Kim, "Two-phase cooling using HFE-7100 for polymer electrolyte membrane fuel cell application," *Appl. Therm. Eng.*, vol. 148, no. August 2018, pp. 868–877, 2019.

국 문 초 록

최근 들어 지속 가능하며 오염 없는 수소 사회에 대한 관심이 증가하고 있다. 수소는 우주에 가장 많은 물질이며 또한 쉽게 제조할 수 있다. 친환경 기술 개발과 더불어 수소 사회가 실현 된다는 가정하에, 수소에너지를 전기에너지로 변환시켜 주는 장치가 반드시 필요하다. 고분자 전해질막 연료전지 시스템은 산소와 수소의 전기화학반응을 이용하여 전기를 발전시키는 시스템이며, 다른 변환 장치에 비해 많은 장점을 가지고 있다. 또한, 가장 널리 사용되고 있는 장치이기도 하다. 다만, 연료전지의 상용화와 보급에 있어 내구성과 신뢰성은 아직 부족하여 극복해야 할 문제로 언급되고 있다. 이러한 내구성과 신뢰성 증진을 위해서는 고장 진단 기술이 반드시 필요하다. 연료전지는 운전 조건에 따라 그 성능과 내구성이 크게 영향을 받기 때문에 시스템에 발생한 문제를 빠르게 진단하여 장치를 보호하는 것이 중요하기 때문이다.

본 연구에서는 먼저 연료전지 시스템에 고장 발생시 그 영향을 관찰하였다. 일차적으로는 연료전지 스택에 반응의 공급 혹은 냉각이 원활히 이루어지지 않는 상황에서의 변화를 실험적으로 관찰하였다. 이어, 연료전지 시스템을 제작하여 연료 공급 시스템, 공기 공급 시스템, 열 관리 시스템에서 발생할 수 잇는 고장 시나리오를 설정하였다. 고장 시나리오는 연료전지 스택 혹은 시스템 전체에 미칠 수 있는 영향을 그 심각도에 따라 분류하였다. 마지막으로 고장을 인가하고 제어 및 계측 신호의 변화 양상을 관찰 및 분석하였다.

다음으로, 본 연구에서는 이러한 연료전지 시스템 고장을 진단할 수 있는 방법을 제안하였다. 고장의 심각도에 따라 변화 반응의 크기와 속도가 다르다는 점에 착안하여, 치명적 고장, 심각한 고장, 사소한 고장을 각각 진단하는 뉴럴 네트워크 기반 알고리즘을 개발하고, 이를 심각도 기반 고장 진단 알고리즘이라 명명하였다. 각각의 뉴럴 네트워크에 입력하는 계측 잔차 값의 이동 평균 시간과 이

를 나누는 분산의 배수 값을 조절함으로 서, 진단 알고리즘의 민감도와 강건성을 동시에 달성할 수 있다는 장점을 갖는다. 또한 고장 실험 없이 고장 시 예상되는 제어 및 계측 신호 값의 증감을 테이블화 하는 것만으로도 본 알고리즘을 개발할 수 있다는 장점을 갖는다. 이러한 방법으로 개발 된 심각도 기반 고장 진단 알고리즘에 고장실험 데이터를 입력한 결과 고장을 성공적으로 진단하는 것을 확인하였다.

이어서, 본 연구에서는 내부 전류 분포를 예측할 수 있는 모델 개발법을 제안하였다. 지금까지의 연료전지 내부 전류 분포 연구는 실험 기반으로, 혹은 모델기반으로 각각 이루어져 왔다. 다만 두가지 접근 방법 모두 필연적으로 한계점을 가진다. 이러한 한계를 뉴럴 네트워크를 도입하여 극복하고자 하였다. 분할 연료전지를 이용하여 압력, 온도, 유량 및 가습도가 변하는 다양한 운전 조건에서의 전류 분포 정보를 습득하였고, 이를 뉴럴 네트워크 모델에 학습시켰다. 그 결과 제한된 데이터만으로 모델을 개발하고, 다양한 운전조건에서 전류 밀도 분포를 예측 할 수 있음을 확인하였다. 이러한 접근법은 상용 연료전지의 개발 과정에서 효율적으로 활용될 것이라 생각한다.

마지막으로, 본 연구에서는 열화 및 고장 발생에 따른 내부 전류 분포를 예측할 수 있는 모델 개발법을 제안하고 검증하였다. 연료전지는 시간이 지나면 필연적으로 열화 한다는 특성을 가지고 있다. 따라서 열화에 따른 전류 분포 변화 특성을 이해하고 예측하는 작업은 중요하다. 하여, 가속 열화 기법을 도입하여 열화에 따른 내부 전류 분포 변화를 먼저 관찰하였다. 또한 가속 열화 시험 중간에 운전 온도 상승, 당량비 증감, 가습도 저하와 같은 고장을 인가하여 전류 분포 변화 정보를 추가적으로 습득하였다. 이러한 정보를 바탕으로 열화 및 열화 진행 상태에서의 고장 발생 시, 전류밀도 분포를 예측하는 뉴럴 네트워크 기반 모델을 개발하였다. 그 결과 모델을 이용하여 효율적이면서도 정확한 전류 밀도 분포 예측이 가능함을 확인하였다.

주요어: 고분자 전해질막 연료전지 시스템, 고장 진단, 고장 심각도, 국소 전류밀도 분포, 열화, 뉴럴네트워크

학 번: 2016-20653